A THREE DIMENSIONAL DISCRETIZED TIRE MODEL FOR SOFT SOIL APPLICATIONS

Eduardo J. Pinto

Thesis submitted to the faculty of the Virginia Polytechnic Institute and State University in partial fulfillment of the requirements for the degree of

Master of Science

In

Mechanical Engineering

Corina Sandu, Chair

Bob West

John Ferris

17th February 2012

Blacksburg, Virginia

Keywords: soft soil tire model, terramechanics, off-road, vehicle dynamics

A THREE DIMENSIONAL DISCRETIZED TIRE MODEL FOR SOFT SOIL APPLICATIONS

Eduardo J. Pinto

ABSTRACT

A significant number of studies address various aspects related to tire modeling; most are dedicated to the development of tire models for on-road conditions. Such models cover a wide range of resolutions and approaches, as required for specific applications. At one end of the spectrum are the very simple tire models, such as those employed in real-time vehicle dynamic simulations. At the other end of the spectrum are the very complex finite element models, such as those used in tire design. In between these extremes, various other models have been developed, at different levels of compromise between accuracy and computational efficiency. Existing tire models for off-road applications lag behind the on-road models. The main reason is the complexity added to the modeling due to the interaction with the soft soil. In such situations, one must account for the soil dynamics and its impact on the tire forces, in addition to those aspects considered for an on-road tire.

The goal of this project is to develop an accurate and comprehensive, while also efficient, off-road tire model for soft soil applications. The types of applications we target are traction, handling, and vehicle durability, as needed to support current army mobility goals. Thus, the proposed approach is to develop a detailed semi-analytical tire model for soft soil that utilizes the tire construction details and parallels existing commercially available on-road tire models. The novelty of this project relies in developing a three-dimensional three-layer tire model employing discrete lumped masses and in improving the tire-soil interface model. This will be achieved by enhancing the resolution of the tire model at the contact patch and by accounting for effects and phenomena not considered in existing models.

ACKNOWLEDGMENTS

I would like to thank Dr. Corina Sandu for all the advice she has given me. Throughout these years she has not only helped me in my formation as a successful engineer but has also helped me to fund my studies and has been a great mentor. I would also like to thank my committee members for all their valuable feedback and knowledge.

Furthermore, I would like to thank the Automotive Research Center and the quad members of my project for funding this project and providing me with great advice and guidance.

I would also like to thank all the colleagues and professors at AVDL that in one way or another have helped in this past few years. I would like to thank Anake Umsrithong and Jeremy Kolanski for all the great advice and guidance. Moreover, I would like to thank Scott Naranjo and Dr. Said Taheri for providing me valuable tire and soil data.

To all the friends that I have met in these years' thanks for all the good and bad times, you won't be forgotten.

Finally, I would like to thank my family for providing me the opportunity to reach all my goals. Their example and inspiration has guided me in this incredible journey. Thanks for all the love, patience and devotion. I will be forever indebted to you.

"In this great future, you can't forget your past"

-Bob Marley

From "No Woman No Cry" lyrics.

Contents

LIST OF FIGURES

LIST OF TABLES

Nomenclature

Variable	Description	Units
A_i	Bulldozing force area	m^2
A_u	Repetitive loading dependent parameter	
b	Tire width	m
c	Soil cohesion	Pa
c_i	Multipass experimental parameter	
c_{sd}	Multipass experimental parameter	
k_u	Pressure-sinkage parameter for repetitive loading	N/m
k_x	Longitudinal shear deformation modulus	m
k_y	Lateral shear deformation modulus	m
k_{xi}	Multipass experimental parameter	
k_{sd}	Multipass experimental parameter	
k_0	Static modulus of soil deformation	N/m
k_1	Sidewall radial spring stiffness (in-plane)	N/m
k_2	Wheel-sidewall circumferential spring stiffness (in-plane)	N/m
k_3	Inter-element radial spring stiffness (in-plane)	N/m
k_4	Circumferential inter-element spring stiffness (in-plane)	N/m
k_5	Lateral inter-element spring stiffness (out-of-plane)	N/m
k_6	Radial inter-element spring stiffness (out-of-plane)	N/m
k_7	Lateral wheel-sidewall spring stiffness (out-of-plane)	N/m
k_8	Circumferential inter-element spring stiffness (out-of-plane)	N/m
c_1	Sidewall radial damping (in-plane)	N.s/m
c_2	Wheel-sidewall circumferential damping (in-plane)	N.s/m
c_3	Lateral inter-element damping (out-of-plane)	N.s/m
c_4	Circumferential inter-element damping (in-plane)	N.s/m
c_5	Radial inter-element damping (out-of-plane)	N.s/m
c_6	Circumferential inter-element damping (out-of-plane)	N.s/m

c_7	Lateral wheel-sidewall damping (out-of-plane)	N.s/m
R	Loaded radius	m
R_s	Sidewall radius	m
R_u	Un-deformed radius; same as belt and tread radius	m
s_d	Longitudinal slip	%
V_x	Vehicle longitudinal velocity	m/s
z_0	Maximum sinkage	m
n	Pressure-sinkage index	
m	Penetration velocity exponent	
m_{total}	Total mass of tire	kg
m_{bead}	Bead mass	kg
$m_{i,bt}$	Belt plus tread element mass	kg
m_{tread}	Tread mass	kg
m_{belt}	Belt mass	kg
$m_{sidewall}$	Total sidewall mass (both sidewalls)	kg
$m_{i,s}$	Sidewall element mass	kg
m_{wheel}	Wheel mass	kg
I_x	Moment of inertia of the wheel about x-axis	kg/m^2
I_y	Moment of inertia of the wheel about y-axis	kg/m^2
I_z	Moment of inertia of the wheel about y-axis	kg/m^2
N_m	Number of masses	
σ_n	Normal ground force	N
τ_x	Longitudinal shear stress	Pa
τ_y	Lateral shear stress	Pa
τ_{max}	Maximum shear stress	Pa
j_x	Longitudinal shear displacement	m
j_y	Lateral shear displacement	m
p	Radial pressure	Pa
p_u	Pressure when unloading cycle begins	Pa

ϕ	Soil angle of internal friction	deg
γ	Soil density	kg/m^3
γ_{si}	Multipass experimental parameter	
γ_{sd}	Multipass experimental parameter	
N_γ	Soil specific weight coefficient	
N_c	Soil cohesion coefficient	
N_q	Soil surcharge load coefficient	
q	Surcharge load from accumulated bulldozed soil	m^3
z_i	Sinkage	m
z_u	Sinkage when unloading cycle begins	m
s_i	Length of contact patch section	m
$\dot{z}$	Vertical penetration velocity	m/s
z_0	Maximum sinkage	m
θ_a	Transition angle	deg
θ_i	Central angle describing mass position	deg
θ_a	Angle of transition	deg
θ_e	Entry angle	deg
θ_m	Angle of maximum normal stress	deg
θ_r	Exit angle	deg
α_c	Slip angle	deg
w_i	Width of contact patch section for mass *i*	m
λ_i	Length of bulldozing volume	m
ψ	Camber angle	deg
υ	Angle of rotation of the rigid wheel	deg
h	Tread height	m
W	Vertical load applied to rigid wheel	N
T	Applied torque to wheel	Nm
T_ϕ	Resultant driving torque at wheel	Nm
T_ψ	Resultant torque about the x-axis at wheel	Nm

T_{α_c}	Resultant torque about the z-axis at wheel	Nm
M_z	Applied moment to wheel about z-axis	Nm
M_x	Applied moment to wheel about x-axis	Nm
F_{ycp}	Lateral shear force	N
F_{ybd}	Bulldozing force	N
F_{xcp}	Longitudinal shear force	N
F_1	Force along the radial direction in local coordinates	N
F_2	Force along the circumferential direction in local coordinates	N
F_7	Force along the lateral direction in local coordinates	N
F_3	Force along the radial direction in local coordinates	N
F_4	Force along the circumferential direction in local coordinates	N
F_{camber}	Lateral force due to a camber angle	N
r_0	Wheel radius	m
yy_i	Relative distance of mass to the belt and tread layer	m
g	Acceleration of gravity	m/s^2

1 Introduction

This section covers the motivation for performing the project, the problem statement, and some of the research challenges encountered. Moreover, it also outlines the structure of this document.

1.1 Motivation

Tire modeling is of outmost importance to the prediction of vehicle performance. The reason is really simple; for a vehicle to move it needs to translate those forces to its tires. Thus, having a tire model that can accurately predict tire forces is indispensable. For this matter, researchers around the world have developed different models to predict tire performance for on-road applications. However, due to the complex interaction between pneumatic tires and soft soils the development of off-road tire models has been lagging that of on-road models. Hence, the importance to develop an off-road tire model that is able to accurately predict the forces at the contact patch.

1.2 Problem Statement and Research Challenges

There are many kinds of tire models, and they are each used with a specific application in mind [1]. Figure 1-1 shows different types of tire models along with their application, frequency and complexity. It can be observed that the most complex and detailed models are the finite element models. On the other hand, the least complex models are the Pacejka type models, which are empirical models that have no physical significance.

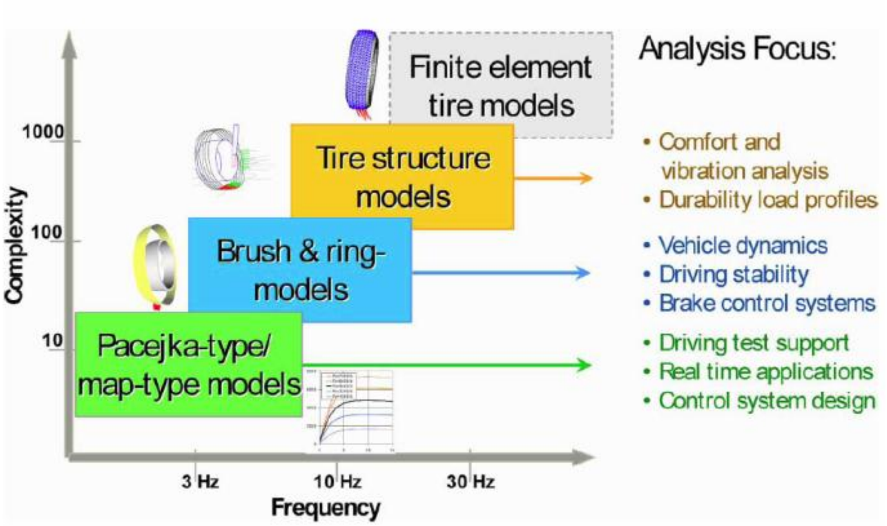

Figure 1-1. Different types of tire models along with their respective application (Reprinted from [1] with permission from Taylor & Francis)

The reason why different tire models are used for different applications lies in the fact that the desired end result for each application is different. For example, ride models are generally really simple because the only response of interest is the vertical motion, thus, developing a really complex finite element models is not desirable. Moreover, operating conditions and desired accuracy are also a factor that needs to be taken into consideration when choosing an appropriate tire model.

For this thesis the intent is to develop a model that is applicable for traction, mobility and handling. As such, the requirements of a vehicle dynamics tire model are: (i) to accurately predict the forces and moments transmitted from the tire to the wheel axle, (ii) widely applicable to different scenarios, and (iii) practical in use (low computational efforts, minimal parameters, etc.). Table 1-1 summarizes the requirement of tire models for different applications in vehicle dynamic analysis.

Table 1-1. Requirements of tire model for different applications. Provided by Anake Umsrithong.

Application	Accuracy	Importance of low computational effort	Parameter assessment effort	Frequency Range
Handling	very high	high	medium	0 - 5 Hz
Ride Comfort	medium	low	medium	0 - 80 Hz
Noise-Vibration	high	very low	medium	0 - 20 Hz
Durability	very high	low	high	N/A
Combined handling and ride analysis	medium	very low	medium	0 - 20 Hz
Control Systems	medium	very high	low	0 - 8 Hz
Multi-Purpose	low	medium	low	0 -80 Hz

Given the complex structure of the tire, the biggest challenge is accurately representing the tire in a mathematical model. Likewise, the challenge is not only being able to represent the tire, but also doing so with the smallest number of tire parameters. Hence, a tradeoff needs to be done.

Another challenge in tire modeling is finding a balance between model complexity and accuracy. As it was previously mentioned, it is important for a tire model to be able to perform adequately in different kinds of scenarios and operating conditions, however, in most cases this means adding complexity to the model. Thus, a compromise needs to be achieved between the scope of the tire model and its computational efficiency.

Finally, the validation of the model is also a big challenge since resources and time are always limiting factors.

1.3 Thesis Outline

Chapter 2 presents an extensive literature review. In this chapter the most important developments in the terramechanics field, as related to wheeled vehicles negotiating on soft soil, are discussed. Moreover, different tire models and tire modeling methods are reviewed and compared.

Chapter 3 first discusses different tire constructions. Next, a detailed explanation of the proposed tire and soil models implemented is given. Finally, a section on the implementation of the model is provided.

Chapter 4 focuses on the validation of the tire model. Different case studies and simulation results are presented in this chapter. The simulation results are compared with experimentally obtained data.

Chapter 5 presents the conclusions of this study and summarizes the work performed. It also presents the contributions made to the field.

Finally, Chapter 6 discusses the challenges left unaddressed and presents some suggestions for future work to fully validate and extend this model.

2 Review of Literature

This chapter reviews the most important theories developed by the terramechanics community in the last 60 years that are pertinent to this off-road tire modeling. It also includes brief references to on-road tire modeling approaches.

The review of literature is divided into three sections. The first section, titled "*Empirical Tire Modeling*", discusses the most important empirical tire models currently available. In the section titled "*Semi-Analytical Tire Modeling*", different semi-empirical on-road and off-road tire models are explored. The section "*Finite-Element Tire Modeling*" covers some of the most representative finite element tire models.

Each modeling approach is first discussed, and the pros and cons of each methodology are outlined.

Empirical tire modeling – Empirical tire models are based on experimental data; thus, they are generally very simple and computationally inexpensive. These models rely on data regression and interpolation methods to characterize tires, which means that they have no physical significance. Nonetheless, these models have proved to be really helpful when modeling transient or really complex tire behaviors. Their main drawback is the fact that full scale tire testing is required. This is generally expensive and time consuming. Moreover, these models can only be used for the application, operating conditions, and tire for which the tire parameters were obtained. Thus, their applicability is limited.

Analytical tire modeling – Analytical tire modeling is at the opposite end of the spectrum compared to empirical tire modeling. These models are based on the physics of the tire; therefore, the formulation is usually really complex and computationally expensive. Furthermore, since the models are based on the physical structure of the tire, their application is broader since it can be adapted to different scenarios or tires. The disadvantage of these types of models is the difficulty in accurately accounting for all physical tire parameters. As such, although analytical models are used for on-road applications, for soft soil applications they are not really popular due to the complex tire-soil interaction.

Finite and discrete element tire modeling – Finite element tire modeling has been on the rise in the recent years. Due to the advances in technology, it has now become feasible to create high-resolution finite element models. The advantage of this type of models is that they provide a more detailed representation what happens with the tire under given conditions; therefore, their use for structural analysis has become transcendental. However, their application to vehicle dynamics simulations has been limited due to the fact that they are still computationally expensive and very difficult to parameterize.

2.1 Empirical Tire Modeling

Empirical models have been around for quite some time now. Sixty years ago, when the problems of off-road locomotion were first being investigated, empirical models were really popular for the sole reason that analytical models were too complex to be solved. Among the first researchers that started doing empirical tire modeling for off-road applications were Wismer and Luth. In [2], Wismer and Luth developed empirical relationships to relate soil conditions and tire characteristics to tractive performance. This model was developed for agricultural applications, thus it was done using bias-ply tires. As such, when radial tires are used, the Wismur-Luth model tends to under-predict the traction of the vehicle. As a consequence, researchers that continued the work of Wismur-Luth had to include variations to account for changes in soil conditions, simulation parameters and radial tires.

Brixius developed a traction prediction model for bias-ply tires in [3] that is based on the same approach proposed by Wismer and Luth. Dimensional analysis was used to develop equations to predict torque ratio, motion resistance ratio and pull ratio as a function of cone index (CI), tire parameters and wheel slip. In the same way as the Waterways Experiment Station Model (WES) [4-6] he used a mobility number to predict the combined effect of soil-wheel parameters on tractive performance. As the mobility number increases, the tractive performance of a wheel improves. This value was determined using curve-fitting techniques in analyzing the traction data. This work was then expanded by Upadhyaya and Wulfsohn in [7, 8].

Uffelmann in [9] investigated rigid wheels operating at small sinkage and gave a simplified pressure relationship as:

$$p = 5.7c \tag{2.1}$$

Next, this equation was used to calculate sinkage and rolling resistance (R) as shown in the following equations (Please note: these equations are valid only for clay soil):

$$z = \frac{W^2}{(5.7c)^2 b^2 d} \tag{2.2}$$

$$R = \frac{W^2}{5.7cbd} \tag{2.3}$$

Where

W = wheel load.

b = tire width.

c = soil cohesion

d = tire diameter.

The STIREMOD [10] is another empirical model, developed by Systems Technology Inc. The model was developed for on-road conditions and then adapted to off-road conditions by applying empirical shaping functions developed by Metz [11]. Essentially, this model creates "*effective coefficients of friction*" to simulate the increased resistance forces encountered when running on off-road conditions.

The model accounts for the combined lateral and longitudinal slip by using equation (2.4), which is a derivation carried out by Szostak and is based on the developments of Sakai, Schallenmach, Grosh and Pacejka. Nonetheless, the applicability of this model is limited since the documentation provided suggests that the model is appropriate for highway vehicles that go into shoulder and slope incursions; thus, it cannot be used for high sinkage scenarios.

$$\sigma = \frac{\pi a_p^2}{8F_z} \sqrt{\frac{K_s^2 \tan^2 \alpha}{\mu_{py}^2} + \frac{K_c^2}{\mu_{px}^2} \left(\frac{S}{1 - S} \right)^2} \tag{2.4}$$

Where

F_z = the normal force

a_p = the tire contact patch length

$K_s \ and \ K_c$ = lateral and longitudinal stiffness, respectively

$\mu_{py} \ and \ \mu_{px}$ = lateral and longitudinal tire/surface coefficients of friction

$$K_s = \frac{2}{a_{po}^2}\left[A_0 + A_1 F_z - \frac{A_1}{A_2} F_z^2 + F_x\left(\frac{|F_{Xest}|}{F_z}\right)\right] \tag{2.5}$$

$$K_c = \frac{2}{a_{po}^2} F_z \left(\frac{CS}{FZ}\right) \tag{2.6}$$

a_{po} = initial contact patch length

α = slip angle

S = longitudinal slip

$$a_p = a_{po}\left(1 - K_a \frac{F_x}{F_z}\right) \tag{2.7}$$

K_a = sensitivity coefficient

$$a_{po} = \frac{\sqrt{F_z \cdot F_{ZT}}}{T_w \cdot T_p} \tag{2.8}$$

F_{ZT} = rated design load

T_w = tire width

T_p = tire pressure

F_{Xest} = term permits increased cornering stiffness under hard braking conditions

$$F_{Xest} = \left(\frac{CS}{FZ}\right) \cdot F_z \cdot S \tag{2.9}$$

$$\frac{CS}{FZ} = \frac{\left(\frac{dF_x}{dS}\right)}{F_z} \tag{2.10}$$

Finally, the Waterways Experiment Station (WES) empirical model [4-6] that subsequently led to the NATO Reference Mobility Model (NRMM) [4-6] is probably one of the most important empirical models. According to Wong in [12], this model was created during WWII "*to provide military intelligence and reconnaissance personnel with a simple means to assess vehicle mobility on a "go/no go" bases in fine- and course-grained soils [12]*". The model uses a cone penetrometer to obtain a cone index (CI), which is the force per unit cone base area. This cone index is then compared to a mobility index (MI) to determine if motion is possible. This mobility index is specific to each vehicle since it is a function of different vehicle parameters such as vehicle weight, type of engine and transmission, etc. It is also important to mention that this model can be used for both wheeled and tracked vehicles. Moreover, it can also account for repetitive loading by calculating a remolding index (RI), which is a measure of the strength of the terrain after it has been remolded. This model is still in use and it keeps getting modified and updated, as expressed by Priddy in [13].

Empirical tire modeling is also present in the on-road community as well. The Pacejka tire model [14], also known as the "magic formula" is probably one of the most widely used tire models in the automotive industry. This model uses polynomial fits to predict the forces and moments at the wheel center, thus, it is very fast. However, its formulation provides no physical insight into the dynamics of the tire.

2.2 Semi-Empirical Tire Modeling

Analytical tire models are definitely a minority when it comes to soft soil tire modeling. The complex structure and variability of soft soils makes it really difficult to represent the interaction by only using analytical methods. On the other hand, empirical models can accurately predict the performance of a tire; nevertheless, they cannot be applied blindly to different simulation scenarios; thus, the importance of semi-empirical tire modeling becomes evident.

Semi-empirical tire modeling is probably the most widely used approach in the terramechanics field. According to Plackett in [15], Bernstein in 1913 was the first researcher to propose a semi-empirical model to predict the contact patch forces acting on a tire operating in soil. He proposed the model based on the pressure sinkage characteristics of a rectangular plate. Bernstein's principle states:

$$p = kz^n \tag{2.11}$$

Where

p = soil pressure

z = sinkage

n = exponent of soil deformation

k = soil sinkage constant

Micklethwaite then used Bernstein's principle in [16] to calculate the rolling resistance in typical military soils. He also used the soil stress failure equation developed by Coulomb to predict the maximum tractive force for a tracked vehicle.

The work by Bernstein also leads Bekker to create his own version of a semi-empirical equation that relates the sinkage with the normal pressure. However, in [17, 18] Bekker suggests that the modulus of soil deformation has to be dependent on the cohesion and the friction of the soil. The proposed relation is commonly referred as Bekker's pressure-sinkage equation,

$$p = \left(\frac{k_c}{b} + k_\phi\right) z^n \tag{2.12}$$

Where

p = soil pressure

z = sinkage

n = exponent of soil deformation

k_c = cohesion dependent parameter

k_ϕ = friction angle dependent parameter

It is important to note that this formulation is only valid for homogenous terrains. The cohesion and friction parameters used in this equation are found by uniformly loading circular or rectangular plates of certain dimensions into the ground with a device called the bevameter (from "**Be**kker **Va**lues **Meter**"). A diagram of how the bevameter test is carried out is presented in Figure 2-1. It is important to note that this Bekker equation is probably the most widely used pressure-sinkage formulation in the terramechanics community.

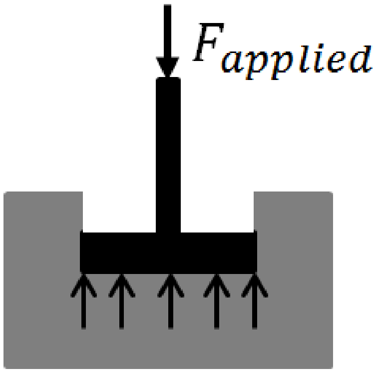

Figure 2-1. Bekker's pressure sinkage relationship carried out with a bevameter

Furthermore, using Uffelmann's work and a uniformly loaded rectangular plate to represent the pressure distribution beneath a rigid wheel, Bekker proposed the following equation for determining the compaction resistance,

$$R_c = \frac{1}{(3-n)^{(2n+2)/(2n+1)}(n+1)\left(k_c + bk_\phi\right)^{1/(2n+1)}}\left(\frac{3W}{\sqrt{d}}\right)^{(2n+2)/(2n+1)} \tag{2.13}$$

Reece proposed in [19] a development of Bekker's equation (2.12) . The difference is that the Reece equation uses dimensionless constants for the cohesion and friction of the soil and a normalized sinkage. The non-dimensional equation is the following,

$$p = \left(ck_c' + \frac{b\gamma_s k_\phi'}{2}\right)\left(\frac{z}{b}\right)^n \tag{2.14}$$

Where

b = the tire width

n = exponent of soil deformation

z = sinkage

c = soil cohesion

${k_c}'$ = dimensionless cohesion dependent parameter.

${k_\phi}'$ = dimensionless friction angle dependent parameter.

γ_s = unit weight of soil.

Several researchers, such as Onafeko and Reece, have pointed out some deficiencies in the Bekker/Reece equations [18]. In [20] these researchers investigated the radial stress beneath a rigid wheel and came to the conclusion that the radial pressure distribution in the contact patch is a function of wheel skid or slip. Through experimental testing they were able to observe that the peak pressure will shift depending on slip or skid, which is contrary to Bekker's assumption that peak pressure is located below the wheel center. Moreover, they were also able to observe that skid and slip also have an effect on the sinkage and rolling resistance of a tire, a term which is now referred to as slip sinkage.

In order to address these faults, Wong and Reece in [21, 22] developed a set of methods to predict the location of peak pressure. For a towed wheel (zero torque at the axle), Wong and Reece proposed that the transition point of tangential stress occurs at the conjunction of two soil failure zones beneath a towed wheel, as illustrated in Figure 2-2. At this location, the shear stress is equal to zero, and the radial stress is equal to the mayor principal stress. Thus, using Mohr's circle for the plastic equilibrium of soils, it is found that two slip lines are on either side of the axis of the principal stress with an angle of $u = 45 - \frac{\phi}{2}$. Thus, the transition point is located by the angle between the direction of the absolute velocity and the radius. Solving equation (2.15) yields the angle of maximum radial pressure (θ_m).

$$\tan\left(\frac{\pi}{4}-\frac{\phi}{2}\right)=\frac{\cos\theta_m-\frac{1}{1+i}}{\sin\theta_m} \tag{2.15}$$

Where

i = slip ratio

ϕ = soil's angle of friction

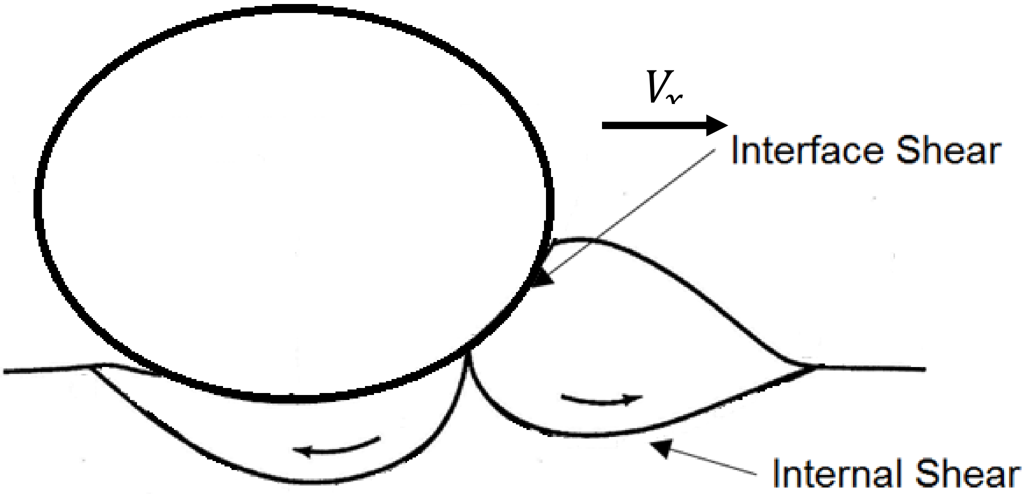

Figure 2-2. Diagram of the failure zones beneath a towed rigid wheel proposed by Wong and Reece. Adapted from [12].

From experimental results, Wong and Reece showed that these two points depart from each other slowly as torque is applied to the wheel. Thus, they came up with an empirical formulation for a driven wheel that is expressed in equation (2.16). It is important to note that this formulation by Wong and Reece was done for two-dimensional dynamics.

$$\frac{\theta_m}{\theta_e}=c_1+c_2 s_d \tag{2.16}$$

Where

θ_m = angular position of the maximum radial stress

θ_e = entry angle

s_d = longitudinal slip

$c_1, and\ c_2$ = empirical constants

Consequently, Wong and Reece used Bekker's equation to calculate the pressure-sinkage relationship. However, the sinkage is defined in two sections. The sinkage from the entry angle (θ_e) to the maximum stress angle (θ_m) is determined from the following formulation,

$$z(\theta) = R_l(\theta)(\sin\theta - \sin\theta_e) \tag{2.17}$$

The sinkage from the maximum stress angle (θ_m) to the exit angle (θ_r) is calculated using Eq. (2.18),

$$z(\theta) = R_l(\theta)\left(\sin\left(\theta_e - \left(\frac{\theta - \theta_r}{\theta_m - \theta_r}\right)(\theta_e - \theta_m)\right) - \sin\theta_e\right) \tag{2.18}$$

The maximum sinkage is evaluated by Eq. (2.19).

$$z_0 = R_l(\theta_m)(\sin\theta_m - \sin\theta_e) \tag{2.19}$$

Karafiath and Nowatzki [23-25] investigated the location of peak pressure in the ground under a rigid wheel, too. By modeling the soil as a plastic material and using the slip line method they were able to calculate the forward and backward slip lines of the wheels. There results show the importance of considering the non-linearity of the failure envelopes for several conditions.

Schwanghart also developed an approach to account for the shift in peak pressure due to sliding or skidding. Schwanghart's model in [26] proposed using two regions to predict the pressure distribution at the contact patch. The tire contact area was assumed to be rectangular, and subdivided into two regions, as shown in Figure 2-3. These two regions were made up of two different parabolas.

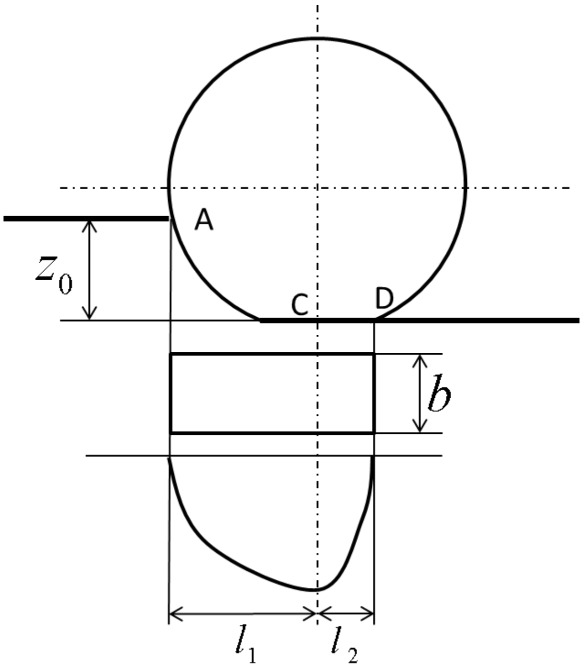

Figure 2-3. Tire Contact patch of Schwanghart's model (Reprinted from [26] with permission from Elsevier)

The pressure distribution in region *A*-*C* was expressed as:

$$p_1 = k_1 z^{n_1} = k_1 \left(z_0 - \frac{x^2}{D} \right)^{n_1} \tag{2.20}$$

In region *C*-*D*, the pressure distribution was calculated using the following equation,

$$p_2 = k_2 u^{n_2} = k_2 \left(u_0 - \frac{x^2}{D} \right)^{n_2} \tag{2.21}$$

In order for this formulation to be suitable, the pressure predicted by both sections needs to be the same at point *C*, therefore

$$P_{max} = k_1 z_0^{n_1} = k_2 u_0^{n_2} \tag{2.22}$$

Combining both regions and integrating yields the total load,

$$W = b\int_{0}^{l_1} p_1 dx + b\int_{0}^{l_2} p_2 dx \tag{2.23}$$

Regarding, the deficiencies pointed out by Onafeko and Reece in the Bekker/Reece equation that sinkage is dependent on slip or skid; several researchers have since tried to include the effects of slip or skid into the pressure-sinkage relationship. Grahn modified Bekker's equation in [27, 28] to account for the penetration velocity of the rectangular plate, the longitudinal velocity of the vehicle and the longitudinal slip. The dynamic pressure sinkage developed by Grahn is based on Bekker's equation:

$$p = kz^n \tag{2.24}$$

Where the sinkage exponent n is constant, but the modulus of soil deformation k is dependent on penetration velocity:

$$k = k_0\dot{z}^m \tag{2.25}$$

Where

k_0 = static modulus of soil deformation

m = exponent of penetration velocity

$\dot{z}$ = rate of vertical sinkage,

$$\dot{z} = \frac{V_x}{1 - sd}\sin\left[\cos^{-1}\left(1 - \frac{z_0 - z}{R}\right)\right] \tag{2.26}$$

V_x = longitudinal vehicle velocity

s_d = longitudinal slip

z_0 = maximum sinkage

R = radius of the tire

The results obtained by Grahn in Figure 2-4 confirm the considerable effect that the penetration velocity has on the pressure-sinkage relationship. According to the results obtained by Grahn, for a constant normal load, the sinkage is smaller at a higher velocity, while the pressure increases with higher velocity. Other researchers that have also investigated this phenomena are Gee-Clough in [29] and Lyasko in [30].

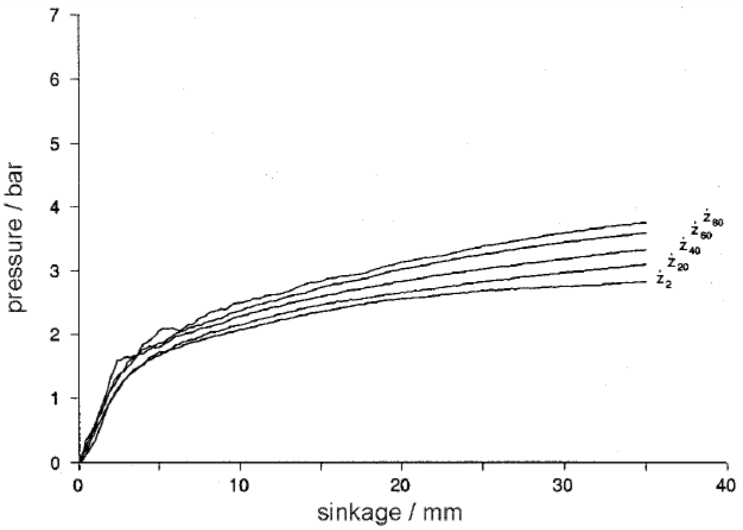

Figure 2-4. Pressure-sinkage curves on loam (14% moisture content) for different penetration speeds. (Reprinted from [31] with permission from Taylor & Francis)

Bekker also developed a formulation to predict the shear strength of the soil for a rolling tire. This shear stress is described by equation (2.27) and it is dependent on the angle of friction and cohesion of the soil. In order to obtain these parameters Bekker conceived a test that consisted of inserting a shear plate or shear cylinder into the soil at different pressures and then determining the cohesion and angle of friction; this test is shown in Figure 2-5.

$$\tau = \frac{K_3}{2K_1\sqrt{K_2^2 - 1}}\left(e^{\left(-K_2+\sqrt{K_2^2-1}\right)K_1 i} - e^{\left(-K_2-\sqrt{K_2^2-1}\right)K_1 i}\right) \tag{2.27}$$

Where

K_1, K_2, and K_3 = experiments constants

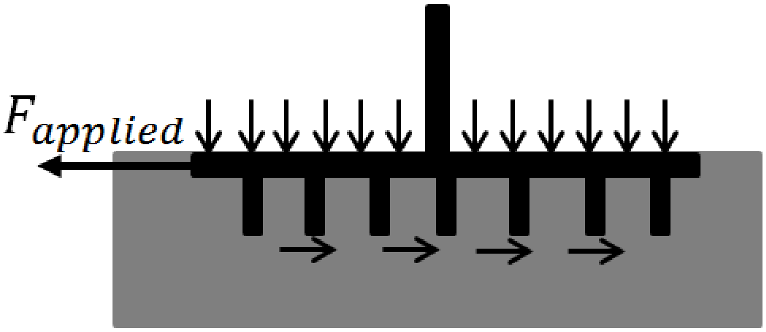

Figure 2-5. Bekker's shear tests

Bekker's shear stress formulation largest drawback is that there is connection between the normal pressure and the shear strength. Hence, Janosi and Hanamoto created an alternative formulation in [32] to calculate the shear stress. They assumed that the shear stress, which acts tangential to the surface of the tire, is defined by the Mohr-Coulomb criterion and the shear displacement of the soil. In this equation the first term is also referred as the maximum shear strength of the soil. However, it is important to note that this equation, as Bekker's, is also heavily dependent on empirical parameters. This formulation is presented in equation (2.28).

$$\tau = (c + \sigma \tan \phi)\left(1 - e^{-j/k}\right) \tag{2.28}$$

Where

c = soil cohesion

ϕ = soils internal angle of friction

j = soil-plate interface shear displacement

k = shear deformation modulus

In order to further investigate the shear stress formulation proposed by Janosi and Hanamoto, Grahn investigated in [28] the effects of different sized shear rings. In this investigation it was found that the shear stress does not depend on the shear ring size. Furthermore, in the same study Grahn concludes that further investigation needs to be done concerning the influence of the horizontal velocity of a point in the contact patch in the calculation of the shear strength in the soil.

The Janosi and Hanamoto equation is defined for conditions of either pure slip or pure drift. However, it was demonstrated by Grecenko in [33, 34] that a combined slip scenario has to be accounted for. The slip and drift model (SDM) developed by Gracenko was the first model that included both longitudinal and lateral dynamics. The constraint equation that relates the longitudinal and lateral forces is:

$$(1 - s_d)F_x \tan\alpha - F_y s_d = 0 \tag{2.29}$$

Where the friction coefficient can be calculated as a function of the deformation gradient, and the maximum shear stress is calculated as a function of the shear deformation. Finally, the longitudinal and the lateral forces are linked to the total shear force through the following expression:

$$F_u = \left(F_x^2 + F_y^2\right)^{1/2} = \tau_{max} b \int_0^1 f(ux)dx \tag{2.30}$$

Where

F_x = longitudinal shear force

F_y = lateral shear force

τ_{max}= maximum shear force

b = tire width

u = deformation gradient

x = coordinate along the contact patch

f = coefficient of friction

Another study that investigated the combined slip scenario for off-road locomotion is Lee et al. [35]. The researchers studied the effect of snow embedment on tires operating in combined slip

[35]. The University of Alaska-Fairbanks created this semi-analytical tire-snow model to satisfy the lack of "*comprehensive tire-snow interaction models for combined (longitudinal and lateral) slips [35].*" Thus, this model uses analytical formulae to describe the physical phenomena when possible, and relies on experimental or finite element simulation results when experimental data is not available.

This model is divided into 4 sub-models: motion resistance, pressure-sinkage, interfacial friction and shear force-slip model. The pressure-sinkage model is based on Wong's approach where pressure is related to sinkage for a terrain of finite-depth. For snow it is really important to model the terrain as a finite depth because snow height has an influence on sinkage, thus, this becomes a determining factor, especially for shallow or fresh snow. Therefore, the pressure-sinkage model uses a semi-analytical approach to model the snow as a Drucker-Prager material and Wong's formula described below,

$$\sigma_n = p_w \left[-\ln\left(1 - \frac{z}{z_w}\right)\right] \tag{2.31}$$

Where

p_w = empirical pressure parameter

z_w = empirical sinkage parameter

z = snow deformation of contact point (vertical deformation of snow)

The tire-snow interfacial friction model uses the classic cone index and mobility number formulation, however, in order to incorporate the snow material parameters and snow depth it has been modified; the cone index is substituted by an empirical pressure parameter (p_w) in the mobility index equations. Thus, the mobility numbers can be calculated using the following equations (only valid for snow),

$$N_{mobx} = p_w \left(\frac{bD}{F_z}\right) \left(\frac{1 + \frac{5\delta}{h_t}}{1 + \frac{3b}{D}}\right) \tag{2.32}$$

$$N_{moby} = p_w \left(\frac{bD}{F_z}\right)\left(\frac{1+\frac{5\delta}{h_t}}{1+\frac{3l_{cp}}{D}}\right) \tag{2.33}$$

Where,

l_{cp} contact patch length due to tire normal deflection

$$l_{cp} = 2\sqrt{\delta(D-\delta)} \tag{2.34}$$

Where,

D = tire diameter

δ = tire normal deflection on snow, $\delta = F_z/K_z$

Thus, the longitudinal and lateral friction coefficients are the following,

$$\mu_x = \mu_{x0}[1 - \exp(-0.5N_{mobx})] + f_{rr} \tag{2.35}$$

$$\mu_y = \mu_{y0}\left[1 - \exp\left(-0.5N_{moby}\right)\right] \tag{2.36}$$

Where,

μ_{x0} = initial longitudinal inherent friction coefficient

μ_{y0} = initial lateral inherent friction coefficient

N_{mobx}, N_{moby} = longitudinal and lateral mobility number, respectively

f_{rr} = longitudinal rolling resistance coefficient

The shear force-slip model takes into account both longitudinal and lateral slip in its formulation. Moreover, an empirical model is developed to characterize the initial driving slip shift, which states that, for off-road tire-terrain interaction, the shear force is not zero when slip is zero.

Finally, the motion resistance model is used to calculate the motion resistance in both the longitudinal and lateral directions. For the lateral direction, the Bekker approach is used since the snow is modeled as being semi-infinite. On the other hand, the longitudinal force is calculated using the following equation,

$$R_x = \frac{bD}{2}\int_0^{\theta_0} \sigma_n \sin\theta \, d\theta \tag{2.37}$$

Where

σ_n = normal pressure described by equation (2.31)

Moreover, Lee et al. has also investigated the effect of snow density on tire-snow interaction in the presence of uncertainty in [36].

Modeling a tire with lugs or tread pattern is really complex due to the fact that these lugs will embed in the soil and the ground forces are applied differently to every section of the tread. As such, for most studies researchers have simplified the problem and assume a smooth tire. However, El-Gawwad et al. developed a multi-spoke tire model [37-40] that investigates the effects of straight and angled lugs. This model was mainly aimed to the modeling of agricultural tires.

After different iterations and modifications El-Gawwad came to some really interesting conclusions about tires with straight lugs. The first one was that the slip angle and the soil deformation modulus have a significant effect on tractive performance. Moreover, they were able to conclude that as the lug height is increased, the tractive forces, lateral forces, overturning moments and aligning moments are all reduced. Another important conclusion was that an increase of the ratio of total area of lugs to total area of tread will lead to lower tire performance.

Even though the straight lug model provided El-Gawwad with great insight as to the effect of lugs in off-road tires, this model was not realistic since agricultural tires have angled lugs. Thus, he decided to expand the model to include angled lugs, and came up with several conclusions. The first one was that angled lugs provide higher lateral forces but lower tractive forces when compared to straight lugs. He also found that, as the soils hardness and deformation modulus increases, the effect of the lug is diminished. And finally he found that an increase in lug angle would decrease the pull forces and increase the lateral forces, thus, suggesting that an increase in lug angle will decrease tractive performance but would increase stability.

The Advanced Vehicle Dynamics Lab (AVDL) at Virginia Tech has developed different deterministic and stochastic tire models for both on-road and off-road applications [41]. Chan's and Senatore's tire model will be discussed due to its applicability to this thesis [42, 43].

This three dimensional steady-state tire model was developed for both rigid and pneumatic tires. Thus, if the carcass rigidity and the inflation pressure of the tire exceed the bearing capacity of the soil, the more complex flexible tire approach is used. Otherwise, since the deformation in the soil is much greater than the deformation in the tire, the tire can be assumed rigid. The rigid wheel model is based on the work done by Wong and Reece [21, 22]. The flexible tire model is an extension of the rigid wheel, which uses the flexible ring approach pictured in Figure 2-6.

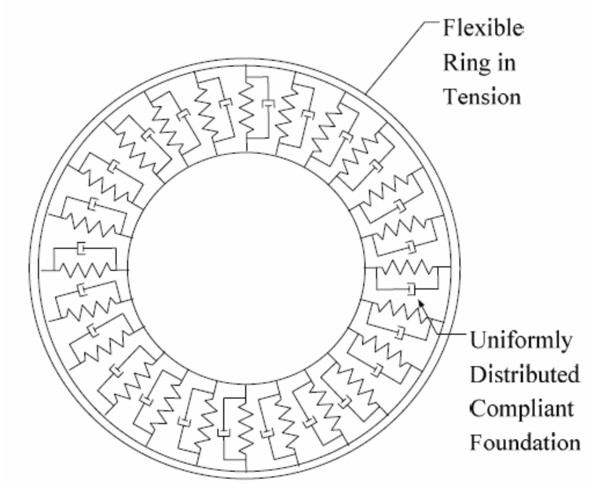

Figure 2-6. The flexible tire modelled as a flexible ring [42]

For this model, the soil is modeled using the plasticity theory; the Reece/Janosi-Hannamoto equations are used to predict normal pressure and shear stress at the contact patch. Likewise, this model accounts for the effects of bulldozing by using the principle of a wall moving into a mass of soil [44]. The model can also account for the combined longitudinal and lateral slip condition. As such, the model changes to pure longitudinal if the slip angle is zero, and consequently, to pure lateral if the slip ratio is zero. The model outputs all the forces and moments at the contact patch while inputting the normal load, the slip ratio, slip angle and the camber angle. Thus, the parameterization of this model is relatively simple.

As part of the literature review for this thesis, the state of the art in commercially available tire models was also investigate. Thus, some of the most representative and accepted commercially available on-road and off-road tire models are briefly discussed in this chapter. However, although the capabilities of these models are mentioned in the available publications, many model details or implementation aspects are not fully divulged.

Systems Technology Inc. has expanded their empirical tire model presented in [10] to accommodate for the additional forces involved in off-road excursions. The model presented in [45] "*adopts a semi-empirical approach that is based on curve fits of soil data combined with soil mechanics theories to capture soil compaction, soil shear deformation, and soil passive failure that associate with off-road driving* [45]."

The main limitation of this model is that it considers the tire as a rigid wheel; therefore, the accuracy of this model in hard surfaces such as clay or sandy loam will be hindered. However, for soft surfaces such as sand or snow it would be appropriate. Another drawback of this model is that it does not consider the multi-pass effect. This is a very important feature especially in surfaces where there is a lot of plastic deformation, since the change in conditions in the soil from the front to the rear axle will differ greatly. Moreover, it is not very clear how this model accounts for the combined longitudinal and lateral slip at the contact patch.

On the other hand, this model does a good job predicting such things as the soil compaction, soil shear deformation, bulldozing effect, compaction resistance, and sinkage. This model simulates the surface as a plastic material. Therefore, it uses Bekker's equations to predict sinkage and compaction resistance. Moreover, the lateral force at the contact patch is calculated taking into consideration both the bulldozing effect and the soil shear strength. For predicting the bulldozing effect it uses the soil cutting theory, which assumes the tire sidewall is the cutting blade and "*the soil in front of the blade will be brought into a state of passive failure [45]*", thus, the soil cutting force is in the same direction of movement. On the other hand, experimental curve fits are used to predict the soil shear strength.

Adams® is a three-dimensional rigid body simulation program. It is regarded as one of the most widely used vehicle dynamics software packages in the industry for on-road simulations. However, the Institute of Automotive Engineering in Hamburg released a soil-tire interface for the simulation of the dynamic vehicle-soil interaction called STINA [46, 47]. The developers of this model characterize it as being "*an alternative calculation method for investigating vibrations of a vehicle on uneven soft ground.*"[52]

The STINA module is comprised of three different models that interact with ADAMS: two semi-analytical models and one FEM based model. The analytical models are for a rigid wheel and an elastic tire, while the FEM based model "*employs data gained from FEM-simulations [47]*", such as different soil strength-properties and inflation pressures.

The rigid wheel semi-analytical model uses Grahn's formulation of dynamic soil behavior to calculate the pressure-sinkage relationship. Thus, the pressure is calculated from both static and dynamic components, while a constant diameter is used to determine the wheel load. On the other hand, the novelty for their elastic model lies in the fact that the formulation uses a larger rigid wheel to approximate the contact area of the deformed tire. This contact area is assumed to have a parabolic shape as seen in Figure 2-7; thus, a simpler mathematical approach can be used. This model uses Bekker's formulation to calculate the pressure-sinkage relationship. As a consequence, the wheel load is calculated using the equation below,

$$F_Z \approx b \cdot k \cdot z_0^{n+0.5} \cdot \frac{\sqrt{1+\frac{f_0}{z_0}} + \sqrt{\frac{f_0}{z_0}}}{1+\frac{n}{2}} \tag{2.38}$$

Where

z_0 = tire sinkage

b = tire width

k = static modulus of soil deformation

n = static sinkage exponent

f_0 = unknown initial tire deflection, which is calculated by iteration

$$f_0 \approx 2 \cdot \sqrt{\frac{f_0}{z_0}} \cdot \sqrt{\frac{D^*}{D} - 1} \cdot f_k \cdot \frac{D}{D^*} \tag{2.39}$$

D^* = contact curve between the tire and the soil

$$\sqrt{\frac{D^*}{D}} \approx \sqrt{1 + \frac{f_0}{z_0}} + \sqrt{\frac{f_0}{z_0}} \tag{2.40}$$

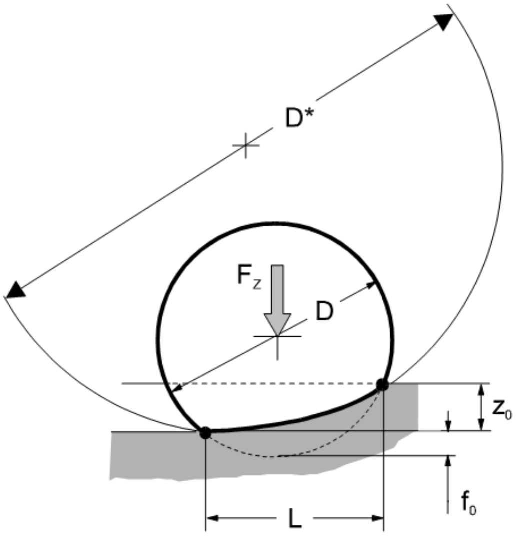

Figure 2-7. Diagram of the physical system used to calculate the elastic tyre diameter and wheel load (Reprinted from [31] with permission from Taylor & Francis)

A good feature of this model is that it takes into consideration the multi-pass effect, however, it "*is based on the hypothesis, that the same pressure sinkage curve applies for the front and rear wheels. Hence the rear wheel does not undergo any additional sinkage unless the soil pressure under the rear wheel is greater than that of the front wheel.*" [53]

The AS2TM tire model presented in [48] is a semi-empirical off-road tire model that was built for the MATLAB/Simulink environment. It is a model that runs faster than real time, thus, it is mostly used for vehicle dynamics simulations to predict traction and mobility. In the same way as the ADVL model, this model uses both a rigid wheel and a flexible wheel approximation depending on the terrain that will be used. The elastic tire model uses the same formulation developed by IKK where a larger radius rigid wheel is used as a substitute for the elastic tire. This principle can be observed in Figure 2-7. It is also important to note that the formula used to calculate the tire deflection is dependent on tire inflation pressure.

The advantage of this model is that it is a tire model that was developed specifically for an off-road environment. Thus, it predicts the pressure-sinkage relationship using Bekker's equations. Moreover, it uses Janosi and Hanamoto's approach to approximate both the longitudinal and lateral shear stress. It also accounts for the multi-pass effect or repetitive loading of the soil using a description that is similar to that developed by Wong and the developers of STINA. Thus, the track module of the model stores the vertical soil deformation and soil compaction of every loading so that it can be used for additional loadings.

The mathematical approach for calculating the lateral and longitudinal forces takes into account the combined longitudinal and lateral slip. This approach is based on the theories brought forth by Schwanghart [26] and Grecenko [33]. In addition, the influence of tire profile (lug height) and the influence of the negative positive portion of the tire treads is included in the model, thus, the effects of tire tread can be investigated. However, it should be noted that lug shape is not included in the model. Additionally, another great aspect of this model is that it can be implemented for both steady state and transient conditions.

The *FTire* Model family [49-52] is comprised of three tire models: Flexible Ring Tire Model (FTire), Rigid Ring Tire Model (RTire), and the Finite Element Tire Model (FETire). This family of tire models is arguably among the most widely accepted tire models in the on-road vehicles industry community. The RTire model is a real-time model that is used for "*test-rig simulations of the standing or slowly rolling tire.*" On the other hand, the *FETire* model is a really detailed finite element model. Finally, the *FTire* model is probably the most widely used off-the-shelf on-road tire model in the market. It is a time-domain, spatial, nonlinear tire simulation model for high-frequency and short-wave-length excitation. The model is really complex and it includes modules for tread-wear, distributed thermal modules, tread pattern geometry and parameterization assistant.

The model for the tire is split into two sub-models, one for the belt-carcass-bead and another one for the mechanical and tribological properties of the tread. This model uses a discrete mass approach to model the tire by using between 100-200 belt elements that have three translational degrees of freedom and one torsional degree of freedom, illustrated in Figure 2-8 and Figure 2-9. It is important to note that this model uses non-linear spring/damper elements that allow for in-plane and out-of-plane displacements. It is also important to note that this model uses different fitting optimization techniques to parameterize and run the model. However, the specifics of these algorithms are not disclosed.

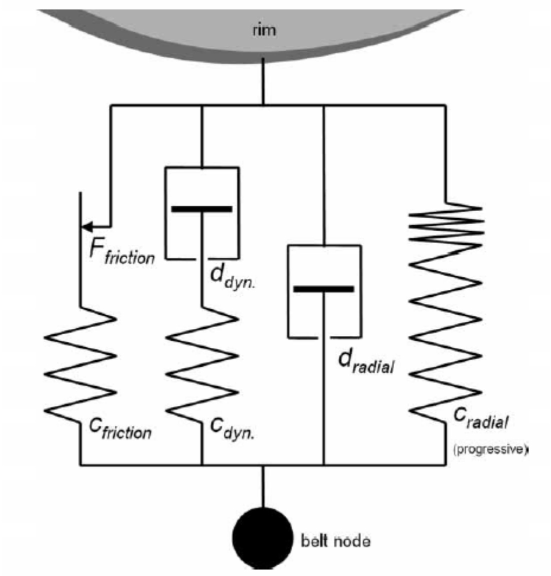

Figure 2-8. Force elements between single belt node and rim (only those in radial direction shown) (Reprinted from [51] with permission from Taylor & Francis)

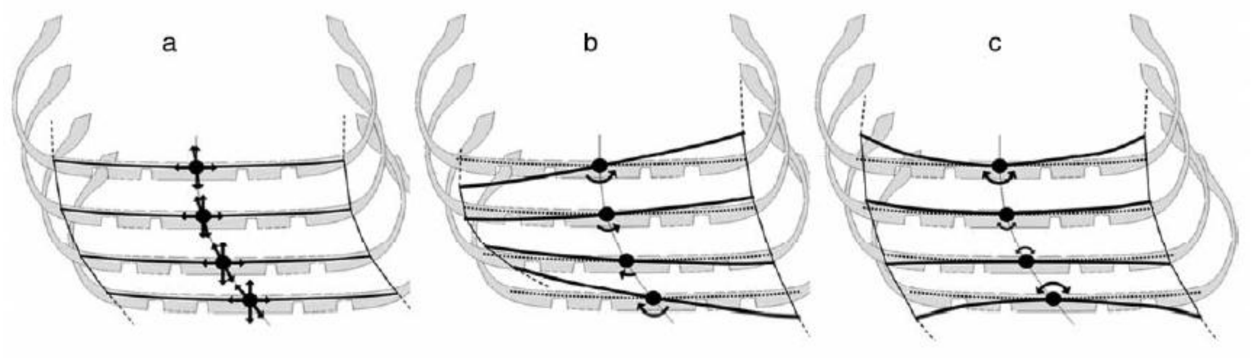

Figure 2-9. Belt elements degrees of freedom (Reprinted from [51] with permission from Taylor & Francis)

Even though this model was developed for on-road conditions, the new version of F-Tire (release v2011-1) has included Bekker's equations in an effort to adapt the model to off-road conditions. However, after contacting the developers of FTire they mentioned that no documentation was yet available on this addition, but mentioned that "*technically, the extension is another road input file type supported by FTire. The calling application passes the file name to FTire and the rest is handled internally. You don't have to set up the flexible road yourself and there is no additional* *interface work compared to any rigid road supported by FTire*. [53]” Thus, the applicability and accuracy of this off-road model is still to be determined.

Even though the work in this thesis was focused towards soft soil tire modeling, different on-road tire models were reviewed in an effort to document the state of the art in tire modeling. The first model reviewed was developed by LMS and its called CDTire. The CDTire family is also comprised of three different tire models [54] that are a compromise between the scope of the application and the computation time. The most basic model is called model 20 and it is a single plane rigid ring model, shown in Figure 2-10. The second model is still a single plane model, however, it has a flexible ring modeling approach. Finally, the most complex model is called the model 40. This is a flexible belt three-dimensional model.

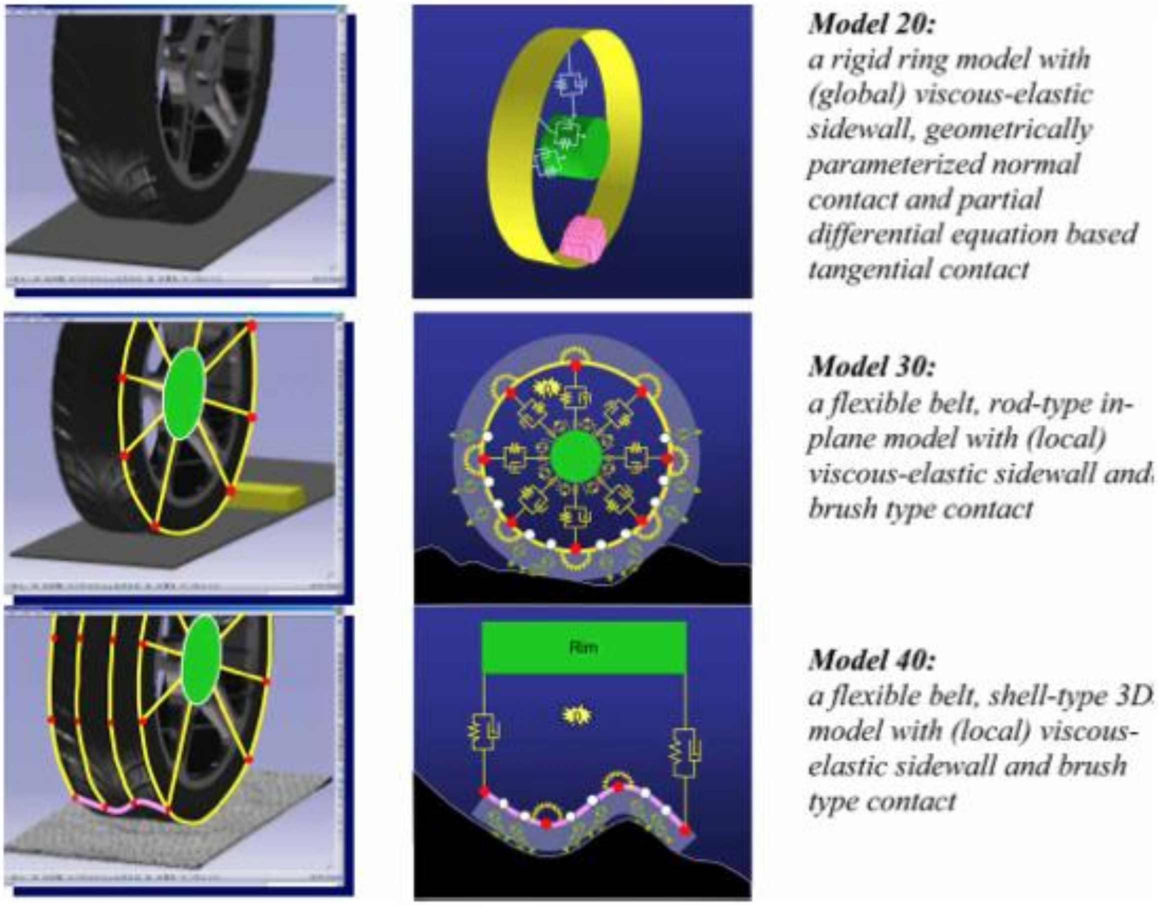

Model 20:
a rigid ring model with (global) viscous-elastic sidewall, geometrically parameterized normal contact and partial differential equation based tangential contact

Model 30:
a flexible belt, rod-type in-plane model with (local) viscous-elastic sidewall and brush type contact

Model 40:
a flexible belt, shell-type 3D model with (local) viscous-elastic sidewall and brush type contact

Figure 2-10. LMS CDTire models (Reprinted from [54] with permission from Taylor & Francis)

Even though three models are available, their creators advertise these models as being adequate for comfort and durability simulations. Similarly to the FTire model, this is a very complex model that includes different modules that help the user to parameterize the model and create road surfaces, but no publication was identified that would indicate its applicability to deformable soil conditions.

Another three dimensional on-road tire model that was investigated is called RMOD-K [55]. Similarly to CDTire, RMOD-K also has a family of models that can be used for different applications. In [56] the creators point out that the class *a* model is mainly used for steady state simulations. On the other hand, the class *b* model is used for the simulation of transient tire forces up to 80Hz. Moreover, this model is able to predict normal pressure distribution based on vertical load and other parameters. Finally, the class *c* tire model is the most complex tire model and it is used to calculate the tire forces over rough terrain or obstacles. This model is also able to predict normal pressure distribution.

properties	class a)	class b)	class c)
slip definition used	yes	no	no
discretizated contact	no	yes	yes
discretizated belt	no	no	yes
frequency range	< 2 Hz	< 80 Hz	< 300 Hz

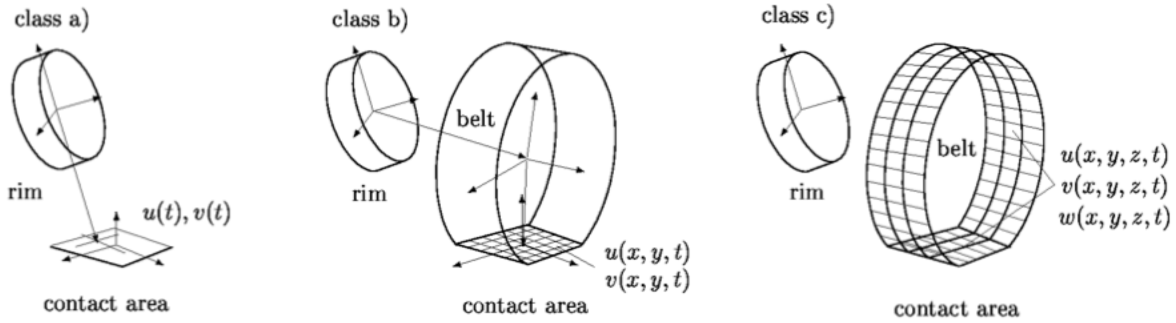

Figure 2-11. RMOD-K tire model classification (Reprinted from [55] with permission from Taylor & Francis)

Similarly, to FTire and CDTire this model also has a parameterization module that can be used to obtain the required tire parameters. Moreover, another good feature of this model is that it can be integrated into ADAMS for full-vehicle simulations.

2.3 Finite and Discrete Element Tire Models

In the last 20 years the use of finite element modeling techniques has increased exponentially. It is mostly due to the fact that computing power has increased, thus, making finite element modeling really useful when the researcher is interested in the internal forces of the tire. One of those researchers is Fervers. He developed a two-dimensional finite element model in [57] since three dimensional models were still too computationally expensive. As such, he transforms the three-dimensional model into a two-dimensional half space. He proposes that the only element that is highly influenced by the three-dimensional model is the carcass. Thus, he models the tread, the air-filled volume, the belt and the rim and replaces the carcass with a force-deflection relation. The results obtained by Fervers show not only good agreement with experimental data but also show good resolution. However, he suggests that more research needs to be done to be able to model the dynamic properties of the soils.

Nakashima and Oida have been other researchers that have pioneered the modeling of the tire-soil interaction problem with the use of the finite element method. However, in [58] they developed a model that implements FE methods to model the tire and the deep soil layer, and discrete element methods to model the soil surface layer. The reasoning behind this approach is that the discrete element method requires lots of computational power to determine contact between the elements; thus, a discrete method approach would be computationally really expensive. However, the discrete method simplifies the interaction between the wheel lugs and deformable soils. Thus, this method utilizes the best of both methods to model the tire-soil interaction. The drawback of this model is that it has not been validated yet and it can only account for static sinkage.

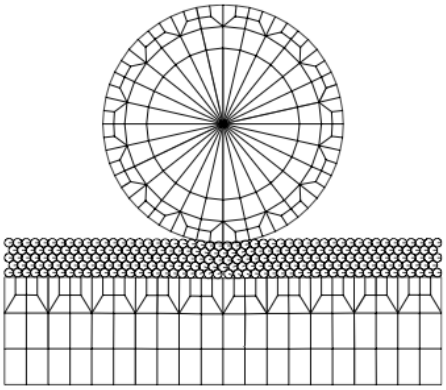

Figure 2-12. Nakashima and Oida's FE-DE tire-soil model after 15,500 steps (Reprinted from [58] with permission from Elsevier)

The FEM model called VENUS (Vehicle-nature Simulation) was developed at IKK and it is the result of the work of Fervers and Aubel [59]. The model consists of three different sub-models. The first one is the tire, which is made of three concentric circles that represent the tread, carcass and the wheel-rim. The tire has elastic properties; however, it is not clear how the parameters for the tire are acquired. The soil sub-model uses the Drucker and Prager formulation to predict the three-dimensional state of stress limits. Moreover, they use elasto-plastic properties to model the soil, which makes this model adequate not only for frictional soils but also for cohesive soils. Finally, the last sub-model is the interaction sub-model, where the interaction of the soil and the tire is modeled. It is important to note that in this interaction model the deformations of not only the tire are outputted but also the soil deformation in the contact patch and around it. Thus, the capabilities of this model are really good since the influence of different parameters can be investigated. Moreover, it can even be extended to find the effect a tire can have on vegetation or slope stability.

Lee et al. also developed a finite element model for snow in [60]. However, one of the most comprehensive FE models for snow was developed by Shoop at the US Army Corps of Engineers. The model described in [61] was initially developed for snow, which is a really plastic terrain. However, in the past few years it has been expanded to include other types of soils and sands. Nonetheless, the main drawback of this model and most FE models is that the model requires a relatively large number of parameters to characterize the tire accurately, which may be feasible if a tire manufacturer provides the parameters

This model uses a modified cap Drucker-Prager plasticity theory model [62] to accurately simulate the surface. On the other hand, it uses the Darnell tire model [63] to properly characterize the elastic tire. This model was chosen because of its relatively low computation time. The principle of this model is to model the tire "*using material properties for the composite material rather than the individual components [61].*" Thus, "*the composite properties were obtained by sectioning the tire and performing laboratory tests on each of the mayor section components (tread, sidewall, and shoulder) [61].*" This creates "*an efficient, accurate, three-dimensional model to predict spindle (axle) forces but not the internal stresses in the tire [61].*" Furthermore, the model can also approximate the tire as being rigid for the times where the terrain used is very soft.

2.4 Review of Literature: Summary

The most well-known and accepted tire and tire-soil/sand/snow models in the terramechanics community were reviewed. Moreover, some of the most relevant and comprehensive commercial tire models were also presented in an effort to document the state of the art in the field. Furthermore, it was shown that there are different types of models that are used for different kinds of applications.

The literature review revealed that many improvements can still be made in the off-road tire modeling field. The mass discretization methods used in the on-road community have yielded very good results, thus, they will be used in an effort to obtain a better resolution and a more representative tire-soil interaction at the contact patch. Moreover, employing the velocity dependent pressure-sinkage methods proposed by Grahn can improve the predicted tire sinkage. However, in order to be able to apply this method, consistent and accurate soil testing methods need to be developed; since current testing methods only account for static conditions. Similarly, the literature review revealed the need to develop more accurate soil models that account for the elastic properties of the soil.

3 Model Development

This section goes over the details of the proposed tire model. The section begins by giving a short overview of tire construction. It will then present the different coordinate systems used, the equations of motion, and the tire-soil interaction model. This explanation is followed by a description of tire and soil parameter identification. Finally, the graphical interface created and some implementation details are discussed.

3.1 Tire Construction Background

This section briefly discusses different types of tires on the market. Specifically, it will show the differences between the two mayor tire constructions: bias-ply and radial tires. Moreover, it will discuss the different parts that make up a tire and the functions that a tire has to be able to perform.

The different parts of a tire are really complex and they can be seen in Figure 3-1. Each of these parts serves a specific function. For example, the liner serves the function of air retention, while the belt provides the lateral and circumferential stiffness. Thus, when it comes to tire modeling it is a great challenge to represent all of these sections accurately.

As it was previously mentioned, tires are one of the most important parts of a vehicle. The reason is that they provide the vehicle with a variety of functions. These functions include but are not limited to: carry load, transmit drive/braking torque, produce cornering force, provide steering response, cushion road inputs and give dimensional stability. Moreover, they have to perform all these tasks according to the following criteria: minimum power consumption, low noise / vibration, tolerate poor maintenance, durable and safe performance, and long wear life. Given the vast amount of functions that the tire has to perform it is really hard to obtain a good performance simultaneously in all of these categories. As such, depending on the application, a compromise needs to be done.

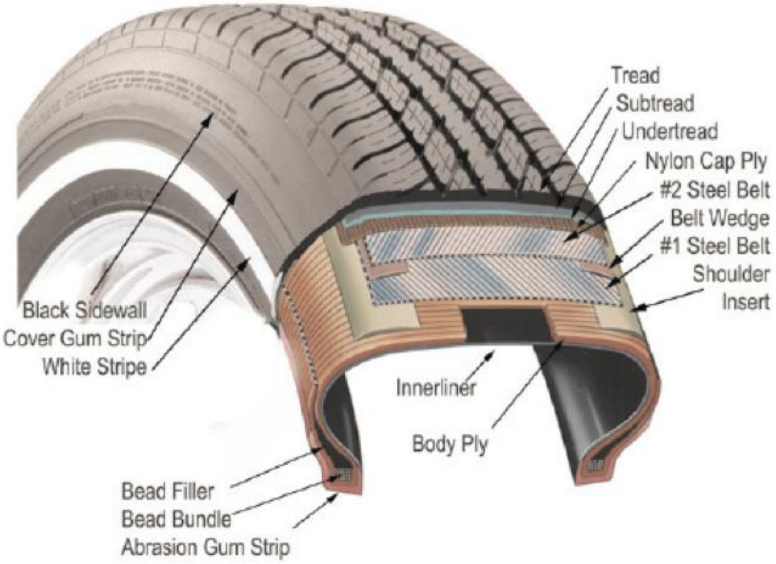

Figure 3-1. Different sections that make up a tire (Reprinted from [64], obtained from NHTSA report DOT-HS-810-561 under the FOIA)

3.1.1 Bias-ply vs. Radial Tires

Even though both radial and bias-ply tires have similar parts, their construction is different. Bias-ply tires were the first tires used in automobiles and they are still being used for a select number of applications. The main difference between bias ply and radial tires is the belt orientation. As it can be observed in Figure 3-2 the belts in the bias-ply tire have a 45° orientation, while the belts in the radial tires are oriented perpendicular to the direction of travel.

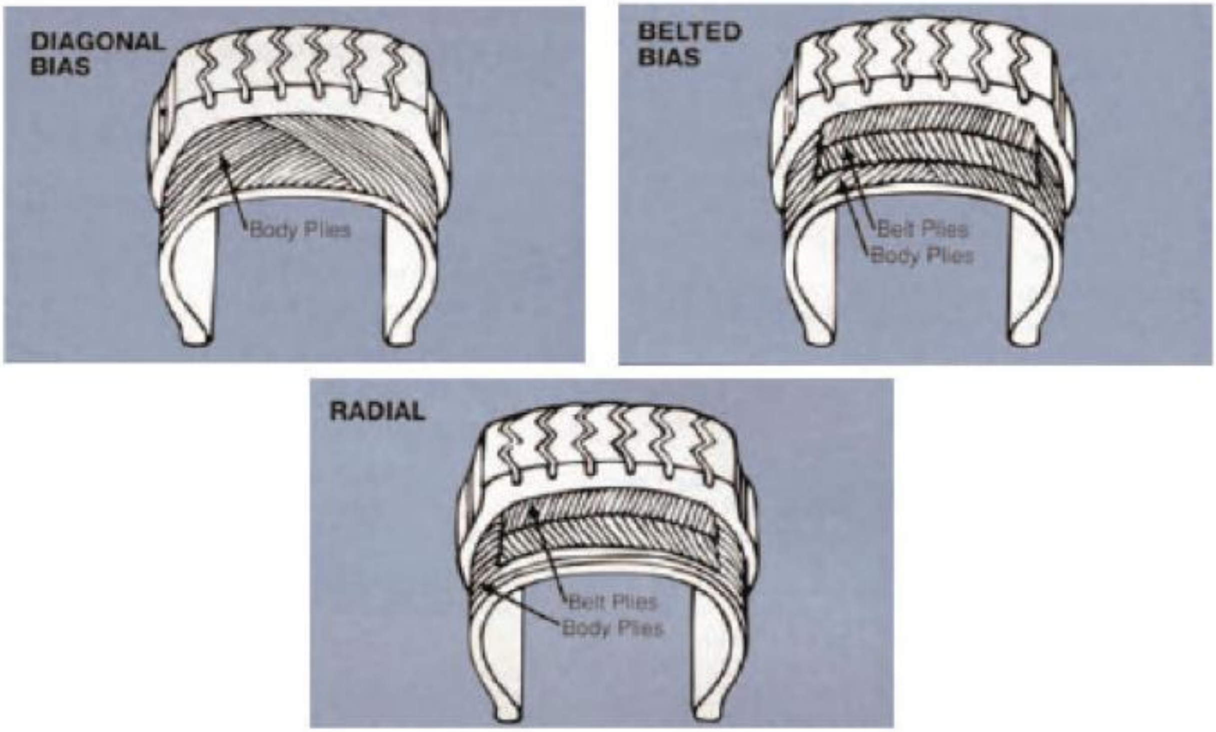

Figure 3-2. Difference between bias-ply and radial tires. Note the belt orientation in both tires (Reprinted from [64], obtained from NHTSA report DOT-HS-810-561 under the FOIA)

The main drawback in bias-ply tires is the increased rolling resistance caused by the scrubbing of the belts. This increased friction will cause higher fuel consumption and higher wear, which makes them less desirable. Moreover, the tread contact area is smaller than that for radial tires, hence, they have less traction. On the other hand, the main advantage of bias-ply tires is their higher load-carrying capabilities. As such, it makes them desirable for towed trailers and other specific applications. Nevertheless, radial tires have replaced bias-ply tires in the passenger vehicle market.

Even though the radial tires were developed after the bias-ply tires, their performance far exceeds the bias-ply tires in almost all aspects. They provide better traction, better fuel efficiency, less noise, longer tread life, better handling and ride comfort.

3.2 Structure of Proposed Tire Model

This section goes over the details of the tire model. Specifically, it will present to the mathematical formulation derived to model the tire.

3.2.1 Model Overview

The proposed soft soil tire model is intended for mobility, traction, and handling applications, and it can also be extended for durability studies. For such reason, a complex semi-analytical tire modelling approach is the best fit.

The schematic of the proposed model can be observed in Figure 3-3. It employs a discretized lumped mass approach that uses springs and dampers in multiple configurations to represent the different sections of the tire. One novelty of this model is that it is structured in three parallel planes, two of them representing the sidewalls (pictured in blue), and one of them represents the belt and tread (pictured in red) of the tire. By differentiating between the sidewall and the belt a more realistic application of the local forces can be implemented, as it can be seen in Figure 3-3. Each plane consists of N_m number of masses; N_m is suggested between 80 and 100, but it is user defined in an effort to increase the versatility of the model. This approach has the advantage of being modular, allowing the user the flexibility in determining the resolution of the model.

The rigid wheel represents the rim of the tire and it is directly connected to the sidewall layers. Thus, the wheel has six degrees of freedom; three translational and three rotational. On the other hand, each lumped mass has three degrees of motion: the translational motion in all directions. Moreover, there is relative motion between masses in the same plane and between masses in adjacent planes, as well. Relative motion is also allowed between lumped masses and the rigid wheel in the circumferential direction, which is another novelty introduced by this model. The total number of degrees of freedom of the model are,

$$DOF = 9N_m + 6 \tag{3.1}$$

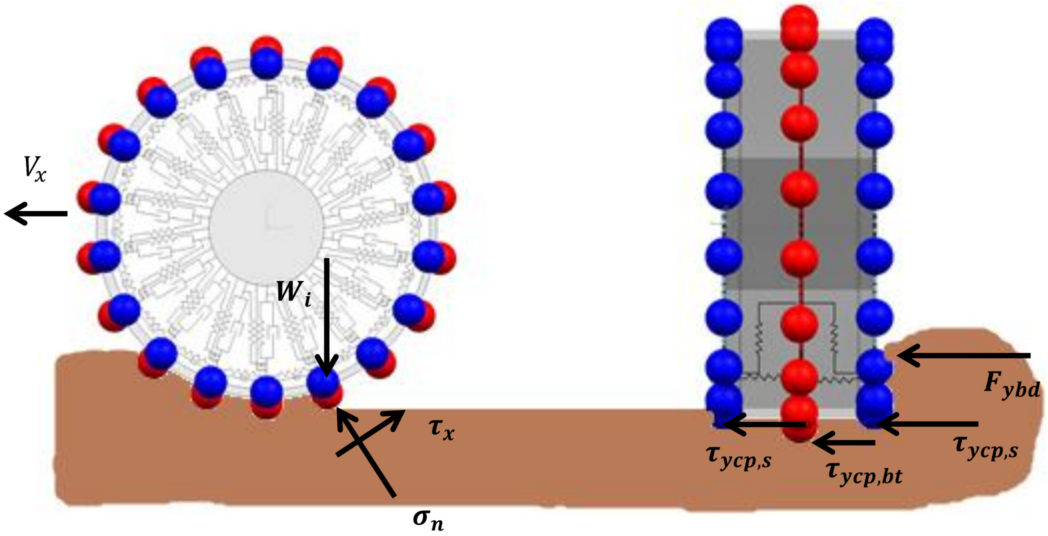

Figure 3-3. Diagram of the tire model. Note that all the soil forces are labelled in black.

The tire model requires several input parameters. The soil model also requires multiple input parameters. All the parameters needed for the tire and the soil models are listed in section 3.5 - Soil and Tire Parameter Identification. The simulation inputs are: slip angle, slip ratio, camber angle, tire load, time for simulation, and finally either a driving torque or a longitudinal velocity. On the other hand, the outputs predicted by the model are: tire deformation, forces and moments in all directions, sinkage for sidewall and tread and belt layers and pressure distribution at the contact patch.

3.2.2 Sidewall Element

The sidewall element is more complex than the belt and tread element because it is directly connected to the rigid wheel. A diagram of the model can be observed in Figure 3-4 and Figure 3-5, and a description of each element can be found in Table 4-1. Notice how each sidewall mass has elastic and damping elements in all three directions. The mass of a single sidewall element ($m_{i,s}$) is calculated using equation (3.2).

$$m_{i,s} = \frac{0.5m_{sidewall}}{N_m} \tag{3.2}$$

The undeformed radius of each sidewall element is the undeformed radius of the tire minus the tread height as shown below,

$$R_s = R_u - h \tag{3.3}$$

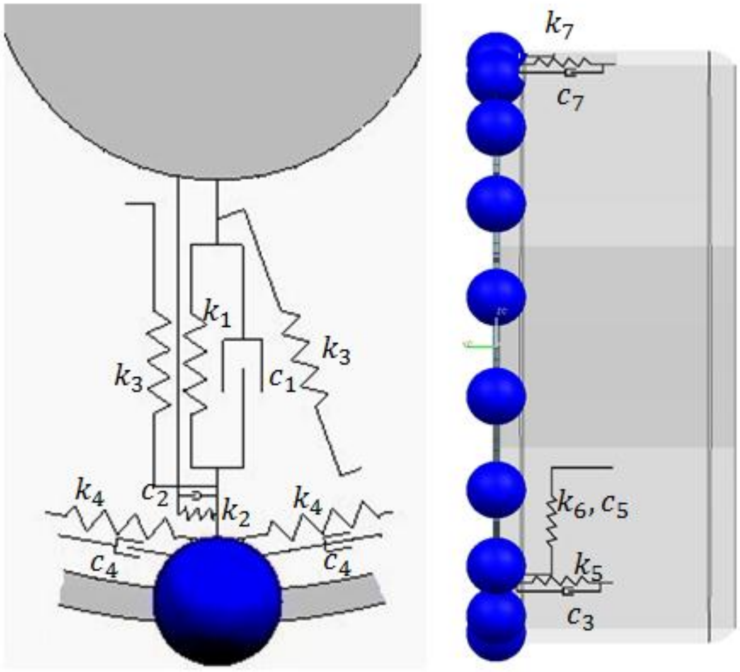

Figure 3-4. Sidewall diagram. Left- the in-plane connections; right - the out-of-plane connections. (k_8 and c_6 not pictured)

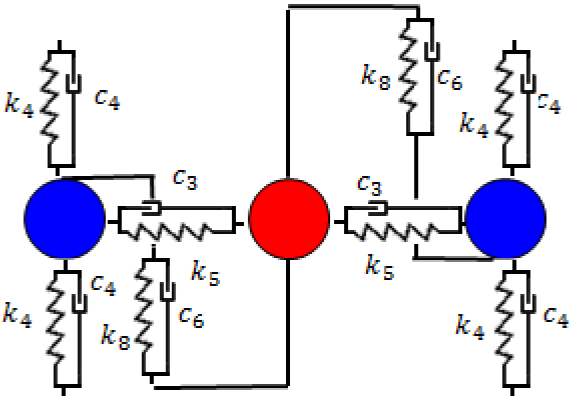

Figure 3-5. Top view of the elements in the circumferential plane.

3.2.3 Belt and Tread Element

The belt and tread element is really different from the sidewall element. This is due to the fact that the tread and belt layer is not directly connected to the rigid wheel. The diagram for the belt and tread element can be found in Figure 3-6. It is important to note that there is an extra set of springs and dampers that connect the sidewall and belt and tread layers in the circumferential direction that is not shown in this figure. However, it can be seen in Figure 3-5. A description of each element can be found in Table 4-1.

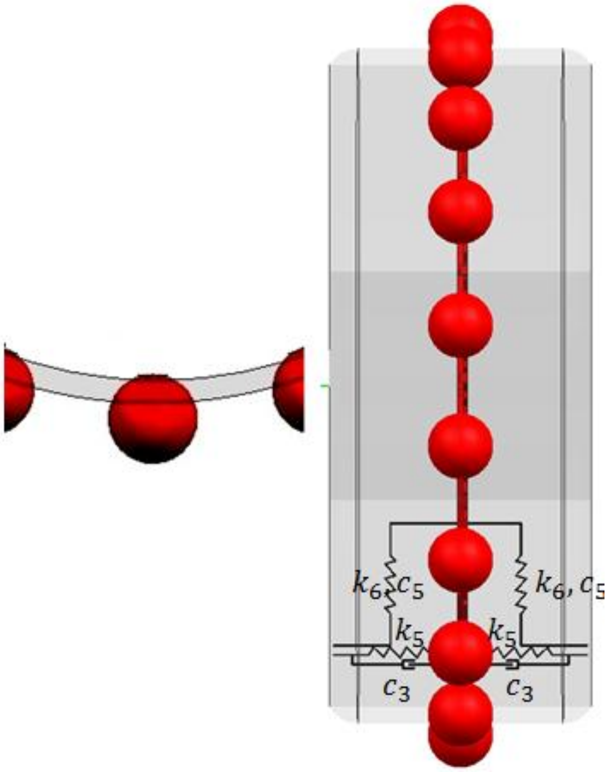

Figure 3-6. Belt and tread element diagram. Left - in-plane view; right - out-of-plane view. (k_8 and c_8 not pictured)

It is also important to note that the undeformed radius of the belt and tread plane (R_u) is equal to what is traditionally understood by the undeformed radius of the tire (R_u); this is larger than the undeformed radius of the sidewall layer; thus the model accounts for the curved shape of the tire.

Table 3-1. Description of tire model elements

Element	Definition
k_1 & c_1	Sidewall radial spring stiffness and damping coefficient (in-plane)
k_2 & c_2	Wheel-sidewall circumferential spring stiffness and damping coefficient (in-plane)

k_3	Inter-element radial spring stiffness (in-plane)
k_4 & c_4	Circumferential inter-element spring stiffness and damping coefficient (in-plane)
k_5 & c_3	Lateral inter-element spring stiffness and damping coefficient (out-of-plane)
k_6 & c_5	Radial inter-element spring stiffness and damping coefficient (out-of-plane)
k_7 & c_7	Sidewall-wheel lateral spring stiffness and damping coefficient (out-of-plane)
k_8 & c_6	Circumferential inter-element spring stiffness and damping coefficient (out-of-plane)

The mass of a single belt and tread element ($m_{i,bt}$) is calculated using the equation,

$$m_{i,bt} = \frac{m_{tread} + m_{belt}}{N_m} \tag{3.4}$$

3.2.4 Coordinate Systems

The model uses the following coordinate systems to describe the position of the wheel and of the lumped masses:

The *X*-*Y*-*Z* coordinate frame is the global reference frame. This global coordinate system follows the ISO 8855 standard, presented in Figure 3-7. Therefore, the positive z-axis is pointing upwards.

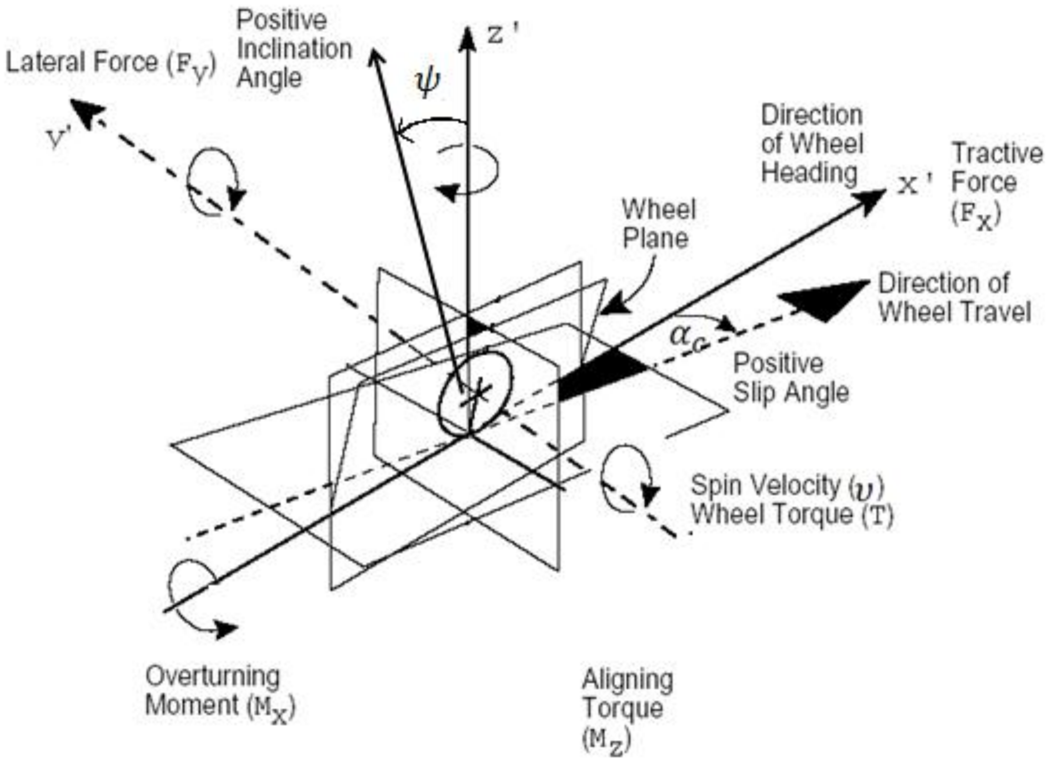

Figure 3-7. ISO 8855 wheel coordinate system. Adapted from [65].

The x_0-y_0-z_0 is the local reference frame fixed to the rigid wheel.

Each lumped mass can be positioned with respect to the local wheel reference frame. Since the lumped masses have relative displacements in all three directions with respect to the rigid wheel, the springs and dampers included in the model along those directions will sustain deformations/displacement. To ease the calculation of deformation forces in the springs and damping forces in the dampers, these forces are computed along the directions of a local reference frame, x_i-y_i-z_i, attached to each of the lumped mass, as seen in Figure 3-8. The lumped mass frames are oriented in such a way that the x_i reference frame points in the circumferential direction and the z_i reference points in the radial direction. Thus, it is worth noticing that these lumped mass reference frames are in fact always rotated with a fixed angle with respect to the directions of the position vectors that locate the mass in the rigid wheel reference frame.

The simulation is carried out in two steps, as explained below. To illustrate the use of the coordinate systems, two random masses where chosen in a two-dimensional space, the first one is denoted with a letter *C* and it is mass 1. The second is mass *i* and it is denoted by the letter *A*.

Initially, the masses are located at positions A and C, which are identified by an angle θ_i, which is calculated using equation (3.5).

$$\theta_i = \frac{2\pi}{N_m}(i-1) \tag{3.5}$$

The first step in the simulation is the rotation of the rigid wheel by an angle υ. Thus, the masses move to locations A' and C' and have angles $\theta_i + \upsilon$. In the second step the lumped masses deform and go to locations A'' and C''. Note that arbitrary deformations where chosen to illustrate the methodology used, in practice the masses can translate in all three directions. It is important to mention that the same method is used to locate the masses in each of the three planes.

Even though the lumped masses are allowed to translate in all directions, it is assumed that the displacements are very small, such that a translation in a given direction doesn't affect those in other directions. This assumption can be made because we are using a very large number of masses. This is a valid assumption for this particular application because this model is to be run on smooth surfaces at relatively slow speeds, which guarantees that we will not be getting large deformations in the tire.

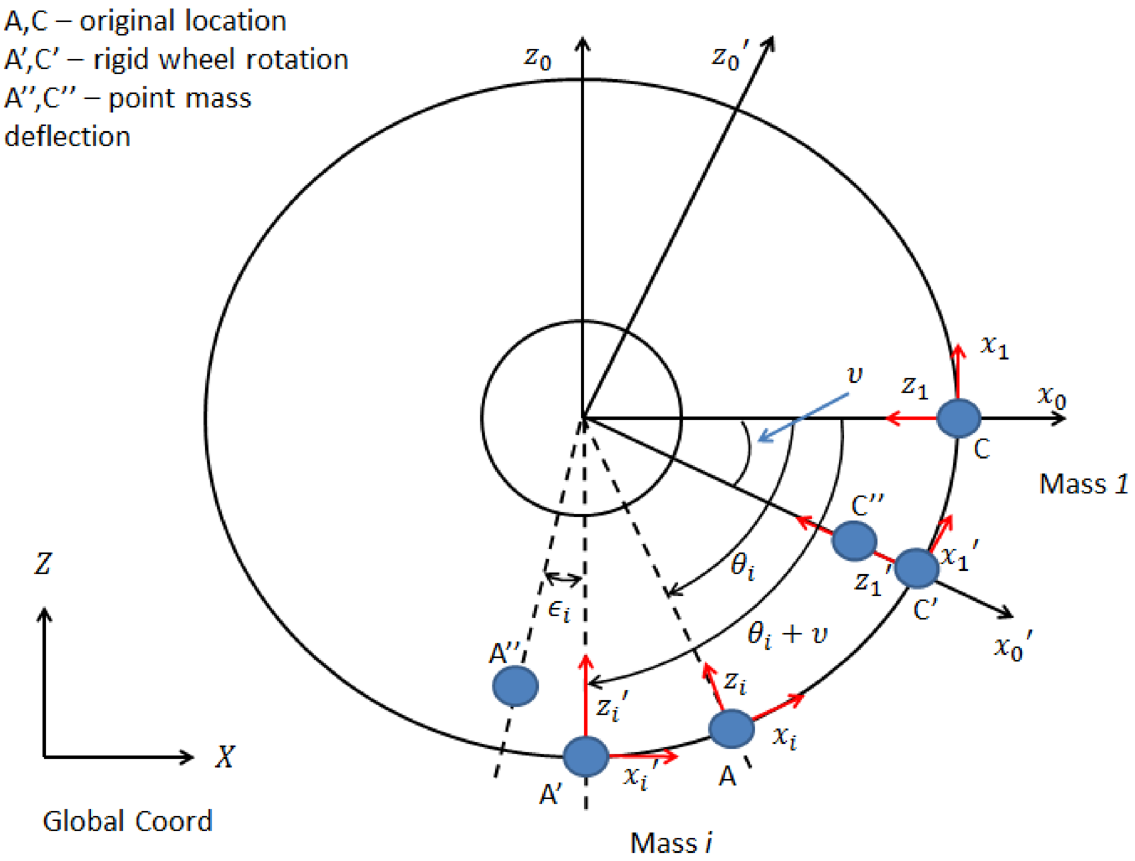

Figure 3-8. Diagram of the coordinate systems used for one plane. Note that Y, y0 and y_i are positive going outside of the page

3.2.5 Equations of Motion

For illustrative purposes all equations presented in this section will be derived for N_m is equal to 1. In the multibody dynamics community a vector of generalized coordinates **q** represents the position and orientation of all bodies. The number of generalized coordinates for this model is $9N_m + 6$. Thus, for the condition that N_m is equal to 1, vector **q** is defined by equation (3.6), where *i* is equal to 1. Note that if N_m is greater than 1 then the pattern will continue; left sidewall coordinates, right sidewall coordinates and finally belt and tread coordinates. It is important to mention that the first index (*i*) represents the mass number and the second one the layer (l- left sidewall, r- right sidewall, bt- belt and tread).

$$\mathbf{q} = [x_0 \quad y_0 \quad z_0 \quad v \quad \psi \quad \alpha_c \quad x_{i,l} \quad y_{i,l} \quad z_{i,l} \quad x_{i,r} \quad y_{i,r} \quad z_{i,r} \quad x_{i,bt} \quad y_{i,bt} \quad z_{i,bt}]^T \quad (3.6)$$

Having defined the generalized coordinate vector the equations of motion are defined by equation (3.7),

$$M\ddot{\boldsymbol{q}} + C\dot{\boldsymbol{q}} + K\boldsymbol{q} = \boldsymbol{F} \tag{3.7}$$

where the vector **F** is defined by the applied external forces, *C* and *K* are the damping and stiffness matrices, and *M* is the generalized mass matrix,

$$M = \begin{bmatrix} M_0 & 0 & 0 & 0 \\ 0 & M_{i,l} & 0 & 0 \\ 0 & 0 & M_{i,r} & 0 \\ 0 & 0 & 0 & M_{i,bt} \end{bmatrix} \tag{3.8}$$

3.2.5.1 Equations of motion for the wheel

The mass matrix for the wheel is defined below,

$$M_0 = \begin{bmatrix} m_0 & 0 & 0 & 0 & 0 & 0 \\ 0 & m_0 & 0 & 0 & 0 & 0 \\ 0 & 0 & m_0 & 0 & 0 & 0 \\ 0 & 0 & 0 & I_y & 0 & 0 \\ 0 & 0 & 0 & 0 & I_x & 0 \\ 0 & 0 & 0 & 0 & 0 & I_z \end{bmatrix} \tag{3.9}$$

The moments of inertia $(I_x, I_y and\ I_z)$ are calculated in equations (3.10) and (3.11) under the assumption that the wheel is a solid cylinder.

$$I_y = \frac{m_0 r_0^2}{2} \tag{3.10}$$

$$I_x = I_z = \frac{m_0(3r_0^2 + b^2)}{12} \tag{3.11}$$

In order to derive the equations of motion for the wheel it is important to first present the transformation matrices used to (i) change between reference frames and (ii) to orient the bodies in the three-dimensional space. The transformation matrix from the lumped mass reference frame to the global reference frame is described by equation (3.12), not that each lumped mass has a different transformation matrix.

$$A_1 = \begin{bmatrix} \sin(\theta_i + \upsilon) & 0 & -\cos(\theta_i + \upsilon) \\ 0 & 1 & 0 \\ \cos(\theta_i + \upsilon) & 0 & \sin(\theta_i + \upsilon) \end{bmatrix} \tag{3.12}$$

The rotation about the y-axis for each mass has the following transformation from the lumped mass reference frame to the global reference frame,

$$A_2 = \begin{bmatrix} \cos(\theta_i + \upsilon) & 0 & \sin(\theta_i + \upsilon) \\ 0 & 1 & 0 \\ -\sin(\theta_i + \upsilon) & 0 & \cos(\theta_i + \upsilon) \end{bmatrix} \tag{3.13}$$

The rotation about the x-axis from the lumped mass reference frame to the global reference frame is described by (3.14). It is pertinent to note that all masses have the same transformation.

$$A_3 = \begin{bmatrix} 1 & 0 & 0 \\ 0 & \cos(\psi) & \sin(\psi) \\ 0 & -\sin(\psi) & \cos(\psi) \end{bmatrix} \tag{3.14}$$

The rotation about the z-axis from the lumped mass reference frame to the global reference frame is also the same for all masses and it is described by equation (3.15).

$$A_4 = \begin{bmatrix} \cos(\alpha_c) & \sin(\alpha_c) & 0 \\ -\sin(\alpha_c) & \cos(\alpha_c) & 0 \\ 0 & 0 & 1 \end{bmatrix} \tag{3.15}$$

The forces acting on the wheel due to the springs and dampers are the following,

$$\begin{aligned} \begin{bmatrix} F_{2,i} \\ F_{7,i} \\ F_{1,i} \end{bmatrix} &= \begin{bmatrix} 0 & 0 & 0 & 0 & 0 & 0 & c_2 & 0 & 0 & c_2 & 0 & 0 & 0 & 0 & 0 \\ 0 & 0 & 0 & 0 & 0 & 0 & 0 & c_7 & 0 & 0 & c_7 & 0 & 0 & 0 & 0 \\ 0 & 0 & 0 & 0 & 0 & 0 & 0 & 0 & c_1 & 0 & 0 & c_1 & 0 & 0 & 0 \end{bmatrix} \dot{q} \\ &+ \begin{bmatrix} 0 & 0 & 0 & 0 & 0 & 0 & k_2 & 0 & 0 & k_2 & 0 & 0 & 0 & 0 & 0 \\ 0 & 0 & 0 & 0 & 0 & 0 & 0 & k_7 & 0 & 0 & k_7 & 0 & 0 & 0 & 0 \\ 0 & 0 & 0 & 0 & 0 & 0 & 0 & 0 & k_1 & 0 & 0 & k_1 & 0 & 0 & 0 \end{bmatrix} q \end{aligned} \tag{3.16}$$

where the first index denotes the direction of the force, and the second one the mass number. Note that the mass number index 0 refers to the rigid wheel.

The forces due to the springs and dampers acting on the wheel are the following in the global reference frame,

$$\begin{bmatrix} F_{x,0} \\ F_{y,0} \\ F_{z,0} \end{bmatrix} = \sum_{i=1}^{N_m} A_4 A_3 A_1 \begin{bmatrix} F_{2,i} \\ F_{7,i} \\ F_{1,i} \end{bmatrix} \tag{3.17}$$

Observing equation (3.17) it is evident that the forces in the springs and dampers connected to the wheel are multiplied by the transformation matrices to bring them back to the global reference frame. The order in which these matrices are multiplied is really important. In this case, the tire is first rotated about the y-axis, this rotation is followed by a rotation of the x-axis and finally by a rotation of the z-axis. In the multibody dynamics community this would be described as an YXZ rotation.

The equations of motion for the wheel are shown in equation (3.18). The term *W* is the applied vertical load on the wheel center, while *T* is the applied driving torque, M_x is the applied torque about the x-axis, and M_z is the applied torque about the z-axis.

$$M_0 \ddot{q}_0 = \begin{bmatrix} F_{x,0} \\ F_{y,0} \\ F_{z,0} - m_0 g - W \\ T \\ M_x \\ M_z \end{bmatrix} \tag{3.18}$$

The following equations are used to obtain the forces and moments at the wheel in the global reference frame,

$$F_x = F_{x,0} \tag{3.19}$$

$$F_y = F_{y,0} \tag{3.20}$$

$$F_z = F_{z,0} \tag{3.21}$$

$$T_\phi = \sum_{i=1}^{N_m} F_{2,i} r_0 \tag{3.22}$$

$$T_\psi = \sum_{i=1}^{N_m} -F_{1,i} \sin(\theta_i + v)\, yy_i - F_{2,i} \cos(\theta_i + v)\, yy_i - F_{7,i} r_0 sign(\sin(\theta_i + v)) \tag{3.23}$$

$$T_{\alpha_c} = \sum_{i=1}^{N_m} -F_{1,i} \cos(\theta_i + v)\, yy_i + F_{2,i} \sin(\theta_i + v)\, yy_i - F_{7,i} r_0 sign(\cos(\theta_i + v)) \tag{3.24}$$

where yy_i is the relative location of the mass in the lateral direction with respect to the belt and tread layer. The command "*sign*" used in equations (3.23) and (3.24) returns a -1 if the corresponding element's angle is less than zero, a 1 if it is greater than zero, and a 0 if it equals zero.

3.2.5.2 Equations of motion - sidewalls

The mass matrix for the sidewalls is the same for both sidewalls since it is assumed that an equal number of masses is used in each sidewall.

$$M_{i,l} = M_{i,r} = \begin{bmatrix} m_{i,s} & 0 & 0 \\ 0 & m_{i,s} & 0 \\ 0 & 0 & m_{i,s} \end{bmatrix} \tag{3.25}$$

Thus, the forces acting on the springs and dampers connected to the left sidewall are presented in equations (3.26), (3.27) and (3.28).

$$\begin{aligned} &\begin{bmatrix} F_{x,i,l} \\ F_{y,i,l} \\ F_{z,i,l} \end{bmatrix} \\ &= \begin{bmatrix} 0 & 0 & 0 & 0 & 0 & 0 & -c_2 - c_6 & 0 & 0 & 0 & 0 & 0 & c_6 & 0 & 0 \\ 0 & 0 & 0 & 0 & 0 & 0 & 0 & -c_7 - c_3 & 0 & 0 & 0 & 0 & 0 & c_3 & 0 \\ 0 & 0 & 0 & 0 & 0 & 0 & 0 & 0 & -c_1 - c_5 & 0 & 0 & 0 & 0 & 0 & c_5 \end{bmatrix} \dot{q} \\ &+ \begin{bmatrix} 0 & 0 & 0 & 0 & 0 & 0 & -k_2 - k_8 & 0 & 0 & 0 & 0 & 0 & k_8 & 0 & 0 \\ 0 & 0 & 0 & 0 & 0 & 0 & 0 & -k_7 - k_5 & 0 & 0 & 0 & 0 & 0 & k_5 & 0 \\ 0 & 0 & 0 & 0 & 0 & 0 & 0 & 0 & -k_1 - k_6 & 0 & 0 & 0 & 0 & 0 & k_6 \end{bmatrix} q \end{aligned} \tag{3.26}$$

$$\begin{aligned} F_{4,i,l} = {} & k_4\left(-z_{i-1,l} \sin \Delta\theta + x_{i-1,l} \cos \Delta\theta \, - x_{i,l}\right) \\ & - k_4\left(-z_{i+1,l} \sin \Delta\theta - x_{i+1,l} \cos \Delta\theta \, + x_{i,l}\right) \\ & + c_4\left(-\dot{z}_{i-1,l} \sin \Delta\theta + \dot{x}_{i-1,l} \cos \Delta\theta \, - \dot{x}_{i,l}\right) \\ & - c_4\left(-\dot{z}_{i+1,l} \sin \Delta\theta - \dot{x}_{i+1,l} \cos \Delta\theta \, + \dot{x}_{i,l}\right) \end{aligned} \tag{3.27}$$

$$\begin{aligned} F_{3,i,l} = {} & k_3\left(x_{i-1,l} \sin \Delta\theta + z_{i-1,l} \cos \Delta\theta \, - z_{i,l}\right) \\ & - k_3\left(x_{i+1,l} \sin \Delta\theta - z_{i+1,l} \cos \Delta\theta \, + z_{i,l}\right) \end{aligned} \tag{3.28}$$

On the other hand, the forces on the right sidewall are the following,

$$\begin{bmatrix} F_{x,i,r} \\ F_{y,i,r} \\ F_{z,i,r} \end{bmatrix}$$
$$= \begin{bmatrix} 0 & 0 & 0 & 0 & 0 & 0 & 0 & 0 & 0 & -c_2 - c_6 & 0 & 0 & c_6 & 0 & 0 \\ 0 & 0 & 0 & 0 & 0 & 0 & 0 & 0 & 0 & 0 & -c_7 - c_3 & 0 & 0 & c_3 & 0 \\ 0 & 0 & 0 & 0 & 0 & 0 & 0 & 0 & 0 & 0 & 0 & -c_1 - c_5 & 0 & 0 & c_5 \end{bmatrix} \dot{q} \tag{3.29}$$
$$+ \begin{bmatrix} 0 & 0 & 0 & 0 & 0 & 0 & 0 & 0 & 0 & -k_2 - k_8 & 0 & 0 & k_8 & 0 & 0 \\ 0 & 0 & 0 & 0 & 0 & 0 & 0 & 0 & 0 & 0 & -k_7 - k_5 0 & 0 & 0 & k_5 & 0 \\ 0 & 0 & 0 & 0 & 0 & 0 & 0 & 0 & 0 & 0 & 0 & -k_1 - k_6 & 0 & 0 & k_6 \end{bmatrix} q$$

$$\begin{aligned} F_{4,i,r} = {} & k_4\left(-z_{i-1,r} \sin \Delta\theta + x_{i-1,r} \cos \Delta\theta \ - x_{i,r}\right) \\ & - k_4\left(-z_{i+1,r} \sin \Delta\theta - x_{i+1,r} \cos \Delta\theta \ + x_{i,r}\right) \\ & + c_4\left(-\dot{z}_{i-1,r} \sin \Delta\theta + \dot{x}_{i-1,r} \cos \Delta\theta \ - \dot{x}_{i,r}\right) \\ & - c_4\left(-\dot{z}_{i+1,r} \sin \Delta\theta - \dot{x}_{i+1,r} \cos \Delta\theta \ + \dot{x}_{i,r}\right) \end{aligned} \tag{3.30}$$

$$\begin{aligned} F_{3,i,r} = {} & k_3\left(x_{i-1,r} \sin \Delta\theta + z_{i-1,r} \cos \Delta\theta \ - z_{i,r}\right) \\ & - k_3\left(x_{i+1,r} \sin \Delta\theta - z_{i+1,r} \cos \Delta\theta \ + z_{i,r}\right) \end{aligned} \tag{3.31}$$

The equations of motion for the left sidewall are defined by equation (3.32). The first terms are due to the internal forces in the springs and dampers attached to the mass, while the second set of terms represent the external force. The ground forces will be explained in detail in section 3.3 Tire – Soft Soil Interaction.

The equations of motion for the right sidewall are presented in equation (3.33)

$$M_{i,l}\ddot{q}_{i,l} = \begin{bmatrix} F_{x,i,l} + F_{4i,l} \\ F_{y,i,l} \\ F_{z,i,l} + F_{3,i,l} \end{bmatrix} + \begin{bmatrix} -m_{i,s} g \cos(\theta_i + v) + F_{xcp,i,l} \\ -F_{ycp,i,l} + F_{ybd,i,l} \\ -m_{i,s} g \sin(\theta_i + v) - m_i R_{i,l} \dot{v}^2 + \sigma_{n,i,l} \end{bmatrix} \tag{3.32}$$
$$M_{i,r}\ddot{q}_{i,r} = \begin{bmatrix} F_{x,i,r} + F_{4i,r} \\ F_{y,i,r} \\ F_{z,i,r} + F_{3,i,r} \end{bmatrix} + \begin{bmatrix} -m_{i,s} g \cos(\theta_i + v) + F_{xcp,i,r} \\ -F_{ycp,i,r} - F_{ybd,i,r} \\ -m_{i,s} g \sin(\theta_i + v) - m_{i,s} R_{i,r} \dot{v}^2 + \sigma_{n,i,r} \end{bmatrix} \tag{3.33}$$

Finally, the position vectors of the lumped masses in the left and right sidewall are described by equations (3.34) and (3.35).

$$\boldsymbol{r}_{i,l} = \begin{bmatrix} x_0 \\ y_0 \\ z_0 \end{bmatrix} + A_4A_3A_2 \begin{bmatrix} R_s \\ -\dfrac{w}{2} \\ 0 \end{bmatrix} + A_4A_3A_2 \begin{bmatrix} -z_{i,l} \\ y_{i,l} \\ x_{i,l} \end{bmatrix} \tag{3.34}$$

$$\boldsymbol{r}_{i,r} = \begin{bmatrix} x_0 \\ y_0 \\ z_0 \end{bmatrix} + A_4A_3A_2 \begin{bmatrix} R_s \\ \dfrac{w}{2} \\ 0 \end{bmatrix} + A_4A_3A_2 \begin{bmatrix} -z_{i,r} \\ y_{i,r} \\ x_{i,r} \end{bmatrix} \tag{3.35}$$

3.2.5.3 Equations of motion - belt and tread

The mass matrix for the belt and tread layer is defined below,

$$M_{i,bt} = \begin{bmatrix} m_{i,bt} & 0 & 0 \\ 0 & m_{i,bt} & 0 \\ 0 & 0 & m_{i,bt} \end{bmatrix} \tag{3.36}$$

The forces acting on the belt and tread elements due to the connected springs and dampers are described below,

$$\begin{aligned} &\begin{bmatrix} F_{x,i,bt} \\ F_{y,i,bt} \\ F_{z,i,bt} \end{bmatrix} \\ &= \begin{bmatrix} 0 & 0 & 0 & 0 & 0 & 0 & c_6 & 0 & 0 & c_6 & 0 & 0 & -2c_6 & 0 & 0 \\ 0 & 0 & 0 & 0 & 0 & 0 & 0 & c_3 & 0 & 0 & c_5 & 0 & 0 & -2c_3 & 0 \\ 0 & 0 & 0 & 0 & 0 & 0 & 0 & 0 & c_5 & 0 & 0 & c_5 & 0 & 0 & -2c_5 \end{bmatrix} \dot{q} \\ &+ \begin{bmatrix} 0 & 0 & 0 & 0 & 0 & 0 & k_8 & 0 & 0 & k_8 & 0 & 0 & -2k_8 & 0 & 0 \\ 0 & 0 & 0 & 0 & 0 & 0 & 0 & k_5 & 0 & 0 & k_5 & 0 & 0 & -2k_5 & 0 \\ 0 & 0 & 0 & 0 & 0 & 0 & 0 & 0 & k_6 & 0 & 0 & k_6 & 0 & 0 & -2k_6 \end{bmatrix} q \end{aligned} \tag{3.37}$$

As such, the equations of motion for the belt and tread layer are defined by equation

$$M_{i,bt}\ddot{q}_{i,bt} = \begin{bmatrix} F_{x,i,bt} \\ F_{y,i,bt} \\ F_{z,i,bt} \end{bmatrix} + \begin{bmatrix} -m_{i,bt}g\cos(\theta_i + \upsilon) + F_{xcp,i,bt} \\ -F_{ycp,i,bt} \\ -m_{i,bt}g\sin(\theta_i + \upsilon) - m_{i,bt}R_{i,bt}\dot{\upsilon}^2 + \sigma_{n,i,bt} \end{bmatrix} \tag{3.38}$$

Using the same formulation as the sidewall masses, the location of the lumped masses in the belt and tread layer is determined using the following equation,

$$\boldsymbol{r}_{i,bt} = \begin{bmatrix} x_0 \\ y_0 \\ z_0 \end{bmatrix} + A_4A_3A_2 \begin{bmatrix} R_u \\ 0 \\ 0 \end{bmatrix} + A_4A_3A_2 \begin{bmatrix} -z_{i,bt} \\ y_{i,bt} \\ x_{i,bt} \end{bmatrix} \tag{3.39}$$

3.3 Tire – Soft Soil Interaction

This section reviews the soil model used; thus, it goes into the different formulations used to calculate the shear stresses and the normal pressure. Moreover, it goes into the details of how the interaction between the tire and the soil model is done. A general schematic of the different variables used is shown in Figure 3-9.

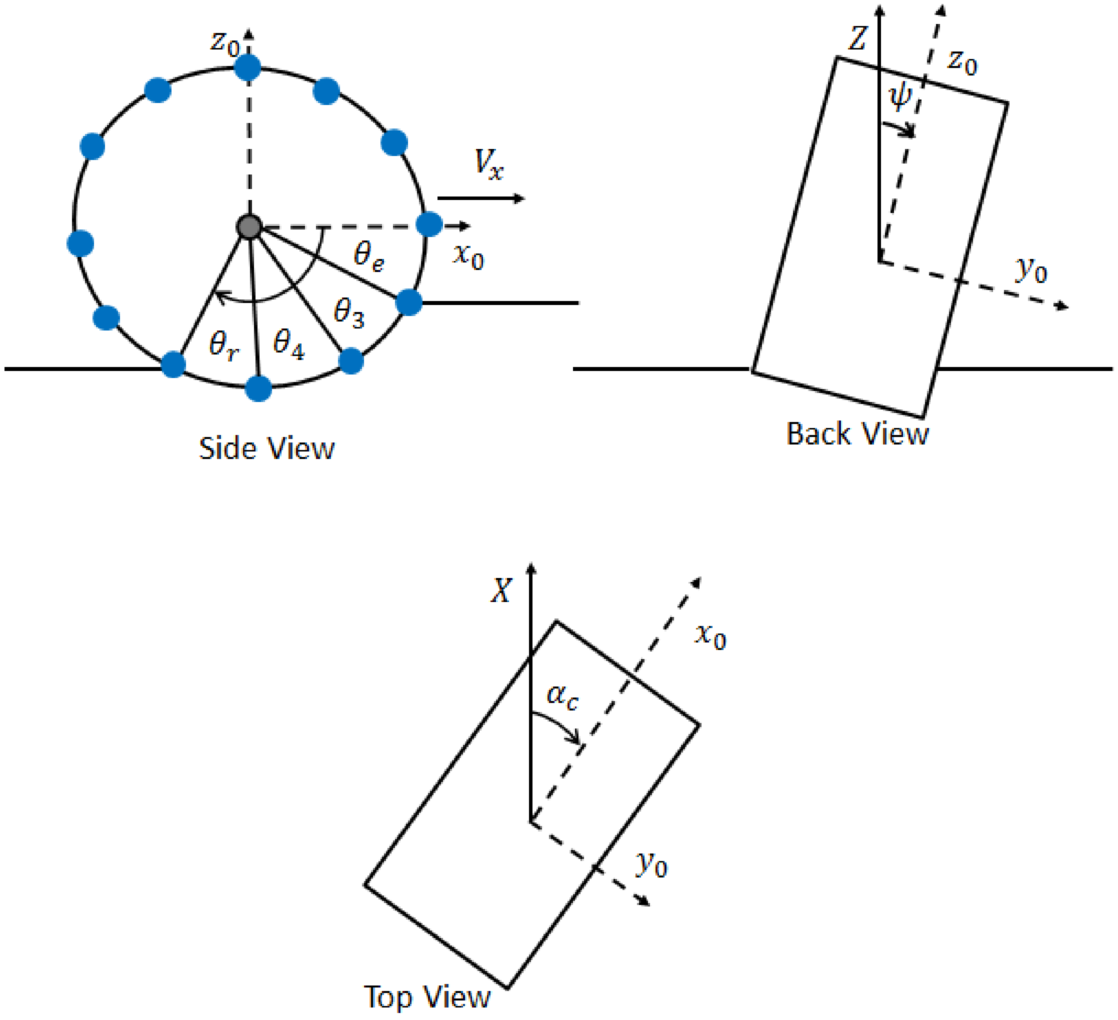

Figure 3-9. Variables used to orient the tire

Most soils have elastic and plastic properties. Thus, the ideal behavior of an elasto-plastic material is described by Figure 3-10. However, parameter identification for the elastic properties of soils is really difficult. As such, the theory of plasticity will be used to model the soil. This assumes that all deformation in the soil is permanent, so the rut and the sinkage are assumed to be the same.

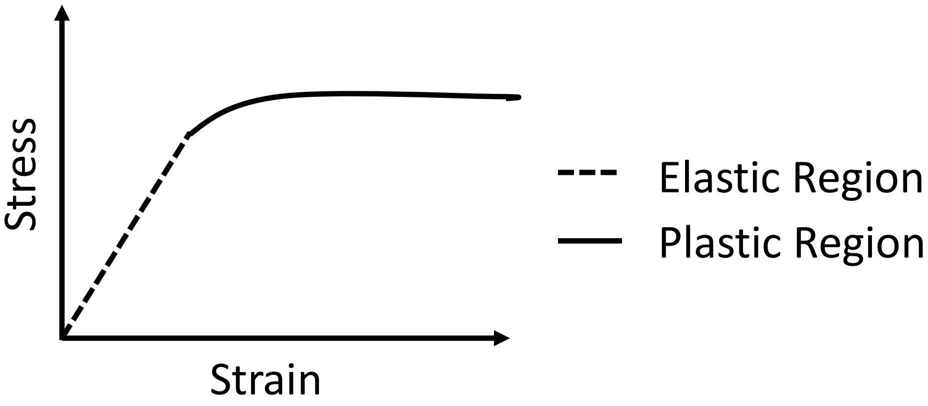

Figure 3-10. Ideal behaviour of an elasto-plastic material

By discretizing the tire into multiple masses and planes, a better resolution can be obtained for the forces in the contact patch. As shown in Figure 3-11, the width of the tire (b) is divided into three sections that represent the sidewall and tread and belt layers. The formulation for the width of each section (w_i) is only dependent on the width of the tire,

$$w_i = \frac{b}{3} \tag{3.40}$$

On the other hand, the length (s_i) of each section is dependent on the deformed radius and the number of masses. The formulation is the following,

$$s_i = R_i \frac{2\pi}{N_m} \tag{3.41}$$

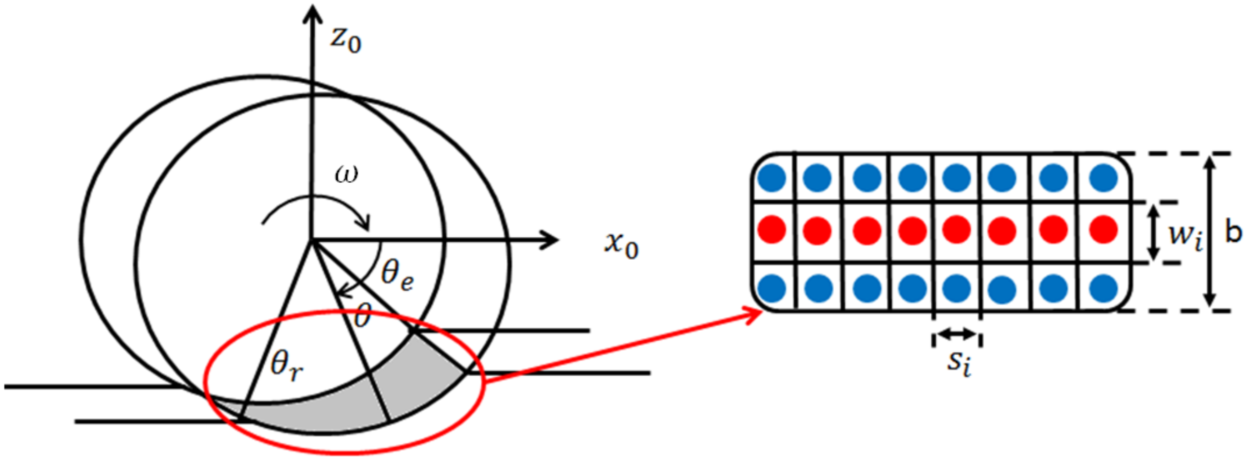

Figure 3-11. Discretization of the contact patch

Before the formulation for the ground forces is presented it is pertinent to define the longitudinal slip or slip ratio (s_d). The slip is really important when it comes to off-road locomotion because without any slip, motion would not be possible. The slip ratio in this thesis is calculated using the SAE standard, which is defined by the equation below,

$$s_d = 1 - \frac{V_x}{R_i \omega} \tag{3.42}$$

where V_x is the longitudinal velocity of the vehicle and ω is the radial velocity of the wheel.

3.3.1 Normal Ground Stress

One of the most important aspects of the interaction of the tire with soft soil is the computation of the normal pressure. The normal pressure is assumed to be perpendicular to the surface of the tire contact patch and it is dependent on the sinkage of the tire; a diagram of this contact force is shown in Figure 3-12. The pressure distribution in the longitudinal direction is depicted in the diagram on the left of Figure 3-12. At the entry angle the pressure in the radial direction is equal to zero and it increases until the location of peak pressure, which according to Reece and Wong [21, 22] will shift with skidding or slipping; the pressure will then decrease until it reaches zero at the exit angle. On the other hand, the pressure distribution in the lateral direction is symmetric left to right, as shown in the diagram to the right of Figure 3-12. However, for steering manoeuvres or straight line driving with a camber angle, the distribution is no longer symmetric about the centre. The shape of the contact patch will change from a rectangle to a trapezoidal shape.

In this study we implement an approach developed by Grahn [27, 28] to calculate the normal pressure (p_i), which is a method derived from Bekker's formulation [12], but with additional features; it includes the effects of longitudinal slip, vehicle velocity, and vertical penetration velocity. The results by Grahn shown in Figure 2-4 demonstrate the large influence that penetration velocity has on the pressure-sinkage relationship, thus motivating the need to account for it in our model.

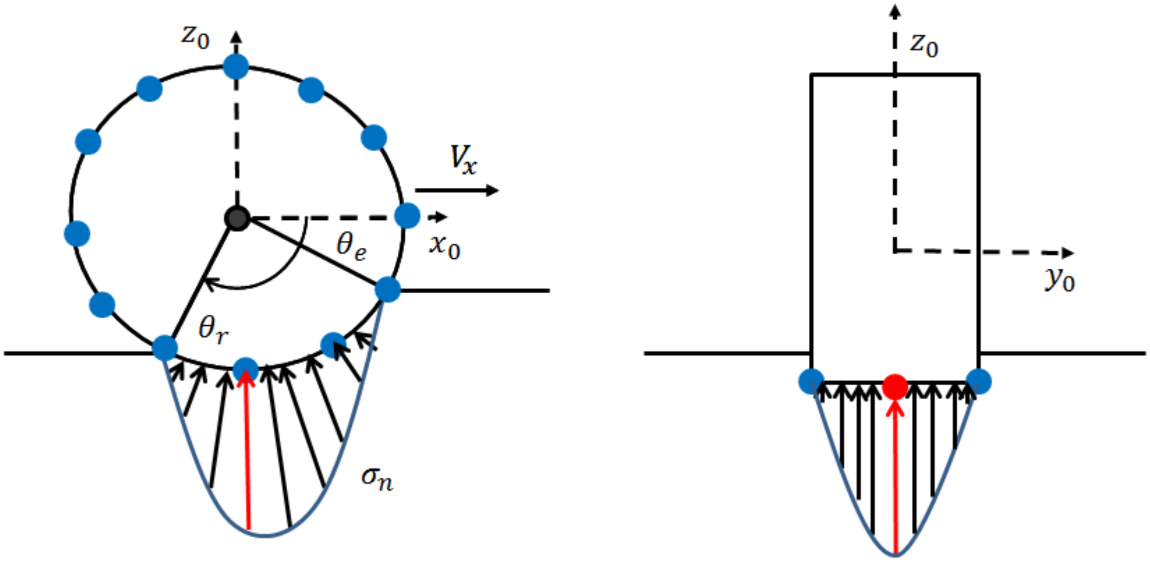

Figure 3-12. Left- Longitudinal pressure distribution in the contact patch. Right – Lateral pressure distribution in the contact patch for straight line driving. The red arrow depicts the location of peak pressure

Using this methodology, the sinkage (z_i) is computed for each section i in the discretized tire model. The pressure in the radial direction on each mass can be computed using equation (3.44). Note that if $m = 0$ then these equations yield Bekker's quasi-static formulation [28]. Thus, the model uses equation (3.43) to calculate the pressure. Furthermore, it also important to note that equation (3.44) is only valid for penetration velocities larger than 0.1 cm/s. Thus, when this condition is not met the model uses (3.43).

$$p_i = \left(\frac{k_c}{s_i} + k_\phi\right) z_i^n \tag{3.43}$$

$$p_i = \left(\frac{k_c}{s_i} + k_\phi\right) z_i^n \left[\frac{V_x}{1 - s_d} \sin\left[\arccos\left(1 - \frac{z_0 - z_i}{R_i}\right)\right]\right]^m \tag{3.44}$$

Once the pressure is obtained at each section, the ground force ($\sigma_{n,i}$) is calculated using the equation shown in equation (3.45),

$$\sigma_{n,i} = p_i w_i s_i \tag{3.45}$$

As it was previously mentioned, the theory of plasticity is used to model the soil. Thus, the ground force is applied to the tire only when the vertical velocity of the wheel is either negative (tire sinks into the ground) or equal to zero (tire touches the surface).

The first step in the simulation is to load the tire. Solving the equations of motion yields the positions, velocities and accelerations of the wheel and lumped masses. Thus, the "*find*" command is used in MATLAB to determine the first mass that has sinkage, which in turn returns the entry angle (θ_e). Similarly, the "*find*" command is also used to determine the last mass that has sinkage, yielding the exit angle (θ_r). Consequently, higher number of masses (N_m) will yield more accurate entry and exit angle.

The second step in the simulation is to start rolling the tire. This steps starts from the initial conditions identified in the dynamic settling performed in step one. For this scenario the entry angle is found in a similar manner. However, for the determination of the exit angle, the "*max*" command is used. This command will find the mass that has the highest sinkage, and thus, yield the exit angle. It is important to note that an algorithm is also used to determine if there are other masses that have the same maximum sinkage. This guarantees that if the contact patch is flat, the correct exit angle is found.

Having computed the normal pressure, the total drawbar pull (*DP*) of the tire is the following,

$$\begin{aligned} DP = &\sum_{i=1}^{N\_m} \left(F_{xcp,i,l} \sin\theta_{i,l} - \sigma_{n,i,l} \cos\theta_{i,l}\right) + \sum_{i=1}^{N\_m} \left(F_{xcp,i,r} \sin\theta_{i,r} - \sigma_{n,i,r} \cos\theta_{i,r}\right) \\ &+ \sum_{i=1}^{N\_m} \left(F_{xcp,i,bt} \sin\theta_{i,bt} - \sigma_{n,i,bt} \cos\theta_{i,bt}\right) \end{aligned} \tag{3.46}$$

where F_{xcp} is the lateral shear force, which is referred to as the shear trust in the terramechanics community. The computation of this force will be addressed in the following section. On the other hand, the ground force term is referred to as the compaction resistance.

In contrast, the computation of forces in the vertical direction is defined by equation (3.47),

$$W = \sum_{i=1}^{N_m} \left(F_{xcp,i,l} \cos\theta_{i,l} + \sigma_{n,i,l} \sin\theta_{i,l}\right) + \sum_{i=1}^{N_m} \left(F_{xcp,i,r} \cos\theta_{i,r} + \sigma_{n,i,r} \sin\theta_{i,r}\right) + \sum_{i=1}^{N_m} \left(F_{xcp,i,bt} \cos\theta_{i,bt} + \sigma_{n,i,bt} \sin\theta_{i,bt}\right) \tag{3.47}$$

where W is the normal load applied to the wheel.

3.3.2 Shear Stress

The shear stress allows the tire to have friction with the ground and be able to move. In this model the shear stress in the contact patch is computed using Janosi and Hanamoto's approach [32]. This approach uses the tangential velocity or interface velocity to calculate the shear displacement in the longitudinal direction ($j_{x,i}$) for each mass in the contact patch. The soil shear displacement will be zero at the entry angle and it will increase until it reaches the exit angle.

$$j_{x,i} = R_i[(\theta_i - \theta_e) - (\cos\theta_e - \cos\theta_i) + s_d(\cos\theta_e - \cos\theta_i)] \tag{3.48}$$

On the other hand, the lateral shear displacement ($j_{y,i}$) is calculated using the lateral slip velocity. The lateral soil shear displacement behaves in the same way as in the longitudinal displacement where it starts at zero and keeps increasing until it reaches the exit angle.

$$j_{y,i} = R_i(1 - s_d)(\theta_i - \theta_e)\tan\alpha_c \tag{3.49}$$

Once the shear displacements are calculated, the longitudinal and lateral shear stress ($\tau_x \; and \; \tau_y$) can be evaluated using equations (3.50) and (3.51) respectively. This approach uses the Mohr-Coulomb soil strength failure criterion.

$$\tau_{x,i} = \left(c + \sigma_{n,i} \tan(\phi)\right)\left(1 - e^{-\frac{j_{x,i}}{k_x}}\right) \tag{3.50}$$

$$\tau_{y,i} = \left(c + \sigma_{n,i} \tan(\phi)\right)\left(1 - e^{-\frac{j_{y,i}}{k_y}}\right) \tag{3.51}$$

where c is the soil cohesion, ϕ is the internal angle of friction, and k_x and k_y are the longitudinal and lateral shear deformation modulus, respectively.

Equations (3.50) and (3.51) are valid for either pure longitudinal or pure lateral simulations. However, for combined slip scenarios the shear strength envelope of the soil needs to be considered. The approach followed in the thesis is consistent with that developed by Sandu and Chan in [42] where the Mohr-Coulomb soil strength failure criterion is used to define the maximum shear strength of the soil,

$$\tau_{max,i} = \left(c + \sigma_{n,i} \tan(\phi)\right) \tag{3.52}$$

Thus, the maximum shear stress envelope is characterized by an elliptical constraint defined by the following equation,

$$\left(\frac{\tau_{x,i}}{\tau_{max,i}}\right)^2 + \left(\frac{\tau_{y,i}}{\tau_{max,i}}\right)^2 \leq 1 \tag{3.53}$$

$$\left(\tau_{x,i}\right)^2 + \left(\tau_{y,i}\right)^2 = \left(\tau_{i,max}\right)^2\Big|_{\theta=\theta_a} \tag{3.54}$$

where θ_a is the angle where the stresses transition from sticking to sliding. Simplifying equation (3.54) yields equation (3.55), which can then be solved numerically to find θ_a.

$$\left(1 - e^{-\frac{R_i[(\theta_a-\theta_e)-(\cos\theta_e-\cos\theta_a)+s_d(\cos\theta_e-\cos\theta_a)]}{k_x}}\right)^2 + \left(1 - e^{-\frac{R_i(1-s_d)(\theta_a-\theta_e)\tan\alpha_c}{k_y}}\right)^2 = 1 \tag{3.55}$$

Consequently, the longitudinal and lateral shear stresses are defined by the following equations,

$$\tau_{x,i} = \begin{cases} \tau_{max,i}\left(1 - e^{-\frac{j_{x,i}}{k_x}}\right) & \theta_e \geq \theta \geq \theta_a \\ \tau_{max,i} & \theta_a > \theta \geq \theta_r \end{cases} \tag{3.56}$$

$$\tau_{y,i} = \begin{cases} \tau_{max,i}\left(1 - e^{-\frac{j_{y,i}}{k_y}}\right) & \theta_e \geq \theta \geq \theta_a \\ \tau_{max,i} & \theta_a > \theta \geq \theta_r \end{cases} \tag{3.57}$$

In principle, equations (3.56) and (3.57) guarantee that the shear strength of the soil never exceeds the failure envelope, however, the bulldozing force is not included in this formulation. Therefore, there might be times were the shear strength of the soil could be exceeded since the bulldozing is added on top of the shear force. However, this simple approach is a good approximation, since the bulldozing stress is relatively small compared to the lateral shear stress.

Using the same approach as in the calculation of the normal force, the longitudinal and lateral shear forces acting on each mass are the following,

$$F_{xcp,i} = \begin{cases} \tau_{x,i} s_i w_i & \theta_e \geq \theta \geq \theta_a \\ \dfrac{\mu_x^2 s_d}{\sqrt{\left(\mu_y \tan \alpha_c\right)^2 + (\mu_x s_d)^2}} \tau_{max,i} s_i w_i & \theta_a > \theta \geq \theta_r \end{cases} \tag{3.58}$$

$$F_{ycp,i} = \begin{cases} \tau_{y,i} s_i w_i & \theta_e \geq \theta \geq \theta_a \\ \dfrac{\mu_y^2 \tan \alpha_c}{\sqrt{\left(\mu_y \tan \alpha_c\right)^2 + (\mu_x s_d)^2}} \tau_{max,i} s_i w_i & \theta_a > \theta \geq \theta_r \end{cases} \tag{3.59}$$

where μ_x and μ_y are the friction coefficients; and they are computed using equation (3.60). The use of these coefficients is really important because it limits the available traction at the contact patch to 1, thus, assuring that the shear forces will not exceed the shear envelope. Furthermore, since the shear forces are bounded, the solver doesn't encounter any convergence issues due to the sliding forces exceeding the maximum shear strength of the soil.

$$\mu_x = \mu_y = \min\left(\frac{\tau_{max,i}}{\sigma_{n,i}}, 1\right) \tag{3.60}$$

3.3.3 Bulldozing Force

The bulldozing effect is created when a volume of the soil in the contact patch is displaced to the sidewall of the tire when cornering. As such, a lateral force is created on the sidewall of the tire. A graphical representation of this phenomenon can be observed in Figure 3-13.

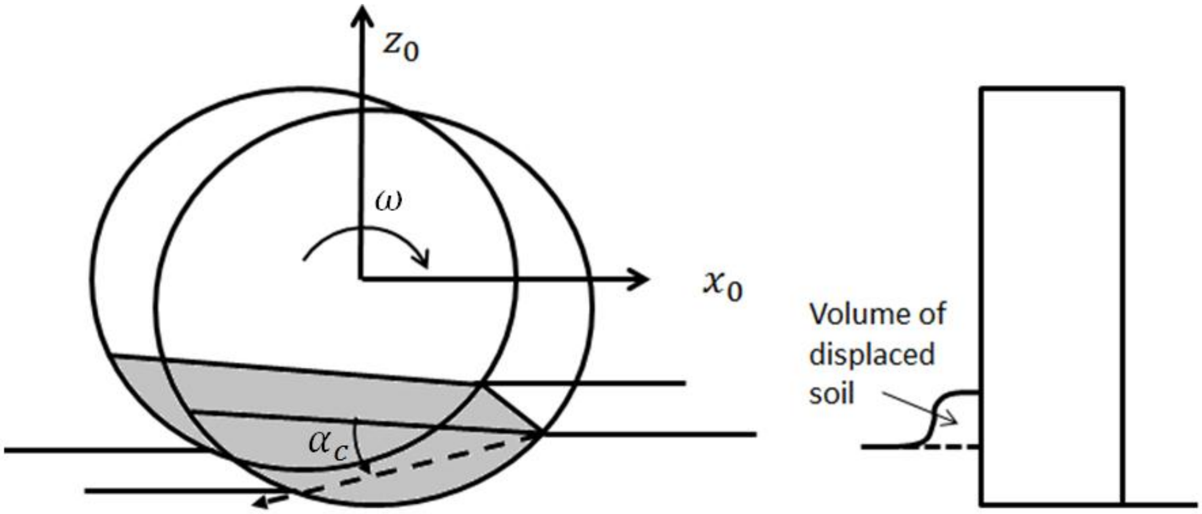

Figure 3-13. Representation of the bulldozing force [42]

Few tire models account for the bulldozing component of the lateral force. Those that incorporate it applied it at the single mass that represents the contact patch. In the current study, due to the discretization of the tire, the bulldozing effect can be applied directly on the sidewall elements, thus increasing the realism of the model. However, it is important to note that this bulldozing force can only be applied at the location of the discrete masses representing the sidewall.

Thus, a bulldozing force will be applied at each mass, which is also a more realistic representation. The formulation used to determine the bulldozing effect is based on the principle of passive ground resistance developed by Terzaghi, which is presented in [26, 44, 66]. This formulation has different dimensionless soil resistance coefficients (N_γ, N_c, N_q) that according to Wong [12] are dependent on the soil angle of friction ϕ. On the other hand, q is the surcharge load from the accumulated soil, which is calculated by assuming that the soil displaced in the lateral direction on each side of the wheel is the same as the volume of soil displaced by the area shaded in grey in Figure 3-13. Thus, the surcharge load q is discretized by the method used in Figure 3-14 and found using the equation below,

$$q_i = \frac{\gamma_s V_{soil,i}}{m_b z_i} \tag{3.61}$$

Where

$$m_b \approx \tan\left(\frac{\pi}{4} + \frac{\phi}{2}\right) \tag{3.62}$$

$$V_{soil,i} = A_i \lambda_i \tan(\alpha_c) \tag{3.63}$$

$$A_i = z_i s_i \tag{3.64}$$

$$\lambda_i = R_i(\cos\theta_e - \cos\theta_i) \tag{3.65}$$

The Terzaghi soil resistance coefficients [67] are found using the succeeding equations,

$$N_q = \frac{e^{2\left(\frac{3\pi}{4} - \frac{\phi}{2}\right)\tan\phi}}{2\cos\left(\frac{\pi}{4} + \frac{\phi}{2}\right)^2} \tag{3.66}$$

$$N_c = \cot\phi\left(N_q - 1\right) \tag{3.67}$$

$$N_\gamma = 2(N_c + 1)\tan(\phi) \tag{3.68}$$

Once the surcharge is determined the bulldozing force is obtained using equation (3.69).

$$F_{ybd,i} = A_i\left(\gamma_s z_i^2 N_\gamma + c z_i N_c + q_i z_i N_q\right)\cos\psi \tag{3.69}$$

It is important to note that the bulldozing force is only applied to the outside sidewall when cornering, thus, assuming that no soil is displaced to the inside of the corner. Furthermore, it is also important to mention that it is estimated that equation (3.69) is applicable to slip angles under 45°.

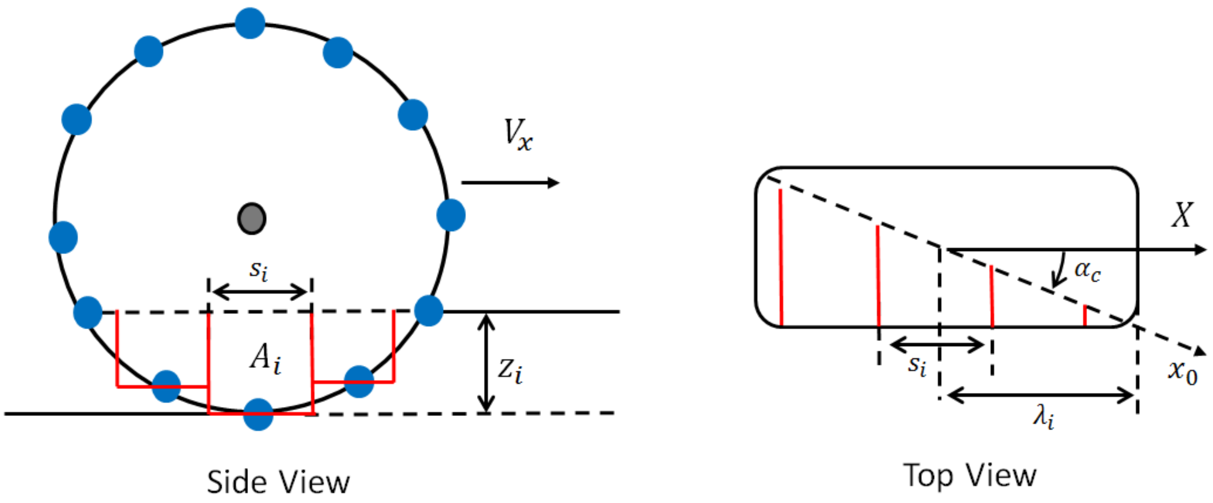

Side View

Top View

Figure 3-14. Volume discretization for the calculation of the bulldozing force

The total lateral force generated by the tire is the summation of the lateral forces at each layer plus the lateral force created by a camber angle,

$$
\begin{aligned}
F_y &= F_{y,i,l} + F_{y,i,r} + F_{y,i,bt} + F_{camber} \\
&= \sum_{i=1}^{N_m}\left(-F_{ycp,i,l} + F_{ybd,i,l}\right) + \sum_{i=1}^{N_m}\left(-F_{ycp,i,r} - F_{ybd,i,r}\right) + \sum_{i=1}^{N_m}\left(-F_{ycp,i,l}\right) \\
&\quad + W \sin\psi
\end{aligned}
\tag{3.70}
$$

3.3.4 Response to Repetitive Loading

The multi-pass is a really important effect for soft soil interaction. The impact of a tire on the soil is dependent on a variety of factors. One such factor is the type of pass. A towed wheel will not alter the properties of the terrain in the same manner as a driven wheel, which induces larger changes [21, 22]. The number of passes also has an influence on the terrain properties. Moreover, the slip ratio also affects the soil properties for repetitive loading scenarios.

Wong in [12] observed that the pressure-sinkage relationship for repetitive loading follows a behavior similar to that of Figure 3-15. The first loading cycle goes from 0-A and the first unloading cycle follows that of A-B. The soil is the reloaded at point B and it follows a path similar to that of the unloading cycle until it reaches the maximum pressure of the first loading cycle; at this point if pressure is increased then sinkage will also increase and it will have a behavior similar to the curve A-C shown in Figure 3-15. According to Wong a similar pattern is observed for subsequent loading and unloading cycles.

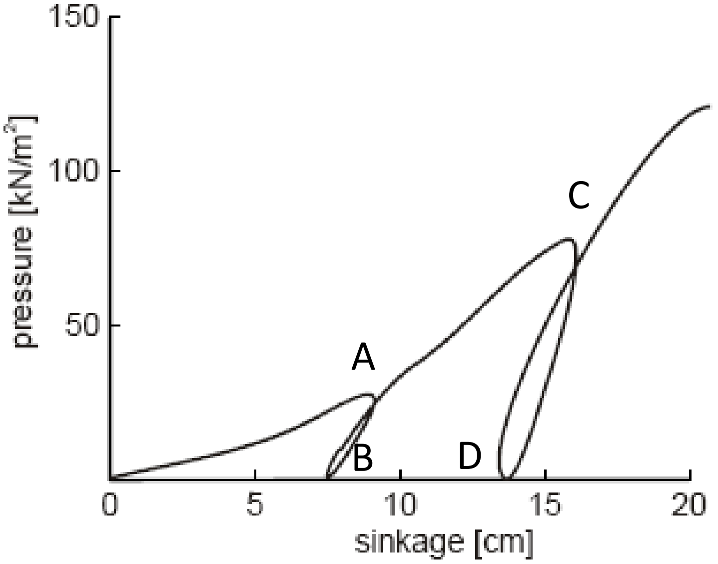

Figure 3-15. Pressure as a function of sinkage for repetitive loading (Reprinted from [68] with permission from Elsevier)

Observing Figure 3-15 it is evident that the loading and unloading cycles do not overlap, phenomenon attributed in [12] to the hysteresis in the soil. However, he proposes a linear relationship that approximates the pressure-sinkage relationship for repetitive loading cycles,

$$p = p_u - k_u(z_u - z) \tag{3.71}$$

where p and z are the pressure and sinkage during unloading or reloading; p_u and z_u are the pressure and sinkage when the unloading begins, and k_u is the pressure-sinkage parameter that approximates the slope of the unloading-reloading line (A-B) and it can be approximated using the following equation,

$$k_u = k_0 + A_u z_u \tag{3.72}$$

where k_0 and A_u are soil parameters that describe the response of the soil to repetitive loading. It is important to note that if the slope of line A-B is vertical the soil has no elasticity and all the deformation is plastic.

Wong in [12] also suggests that the multi-pass effect not only has an effect on the pressure-sinkage relationship, but also on the shear strength of the soil. Observing Figure 3-16 it is evident that consecutive shearing cycles (CDE) follow a similar behavior of that of the first cycle (OAB), which implies that further shear displacement is required to obtain maximum shear stress.

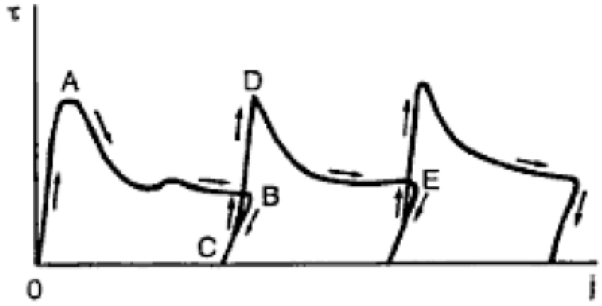

Figure 3-16. Response to repetitive shear loading on dry sand (Reprinted from [68] with permission from Elsevier)

Even though other researchers such as Harnisch et al. [48] have used Wong's approach with satisfactory results, this study will rely on the work of Holm [69] and Senatore [43] to predict the response to the multi-pass effect. The main idea of this approach is to estimate new parameters for the soil based on the pass type, slip, and number of passes.

Observing the results of Holm in Figure 3-17 it is evident that the drawbar pull increases as the number of passes increases. This is mainly due to the fact that the compaction of each successive pass reduces the rolling resistance. Moreover, it is also evident that driven wheels will create more compaction than towed wheels, and thus, have higher drawbar pulls as the number of passes increases. Furthermore, it also evident that the greatest variation in drawbar pull occurs between the first and second pass. Thus, the following relationships were developed to predict the change in soil conditions due to repetitive loading,

$$c = (c + c_{sd}) + c_1 s_d \tag{3.73}$$

$$\gamma_s = (\gamma_s + \gamma_{sd}) + \gamma_{s1} s_d \tag{3.74}$$

$$k_x = (k_x + k_{sd}) + k_{x1} s_d \tag{3.75}$$

where c_{sd}, γ_{sd}, and k_{sd} are parameters that are dependent on the type of pass, and c_1,γ_{s1}, and k_{x1} are functions of number of passes. In the case of a towed wheel, c_{sd}, γ_{sd}, and k_{sd} are equal to zero. On the other hand, for driven wheels their value is dependent on the wheel slip. Instead, for the parameters that are dependent on the number of passes, their value is equal to zero for the first pass and then it is contingent to the number of passes.

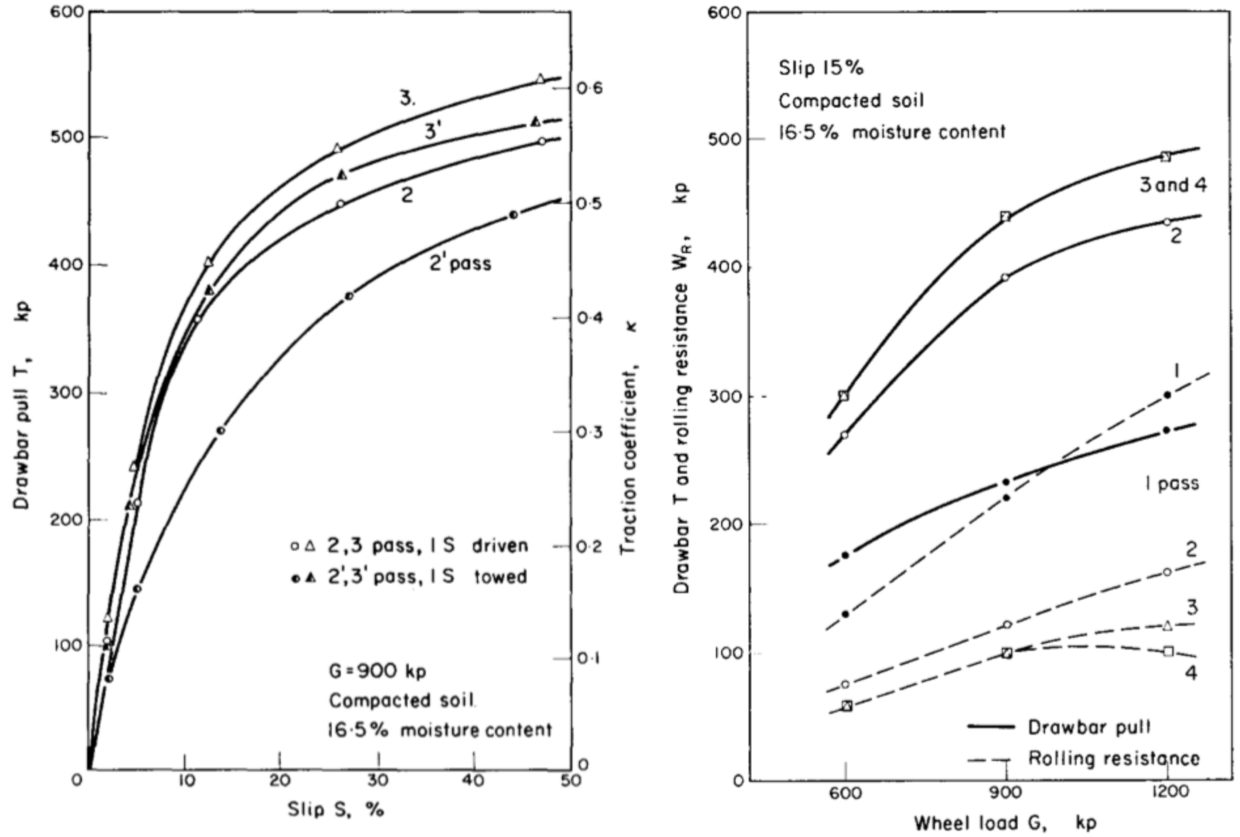

Figure 3-17. Repetitive loading results obtained by Holm. Left – Drawbar pull as a function of slip ratio for driven and towed wheel. Right – Drawbar pull and rolling resistance as a function of wheel load. (Reprinted from [69] with permission from Elsevier)

3.4 Implementation

The model is developed as a MATLAB m-file for version 7.12 (R2011a). Several built-in MATLAB solvers were used to solve the simulations. Nonetheless, the best performing solver was ODE113, which is a variable time step, non-stiff, variable order solver. Another solver that was used was ODE45, which is also a variable time step, non-stiff solver that uses the Runge-Kutta method (4-5 order).

It is important to note that the solvers used in this thesis cannot account for discontinuities, therefore, in order to model the contact between the tire and the ground the hyperbolic tangent function was used to model the transition between contact and no contact. By introducing this hyperbolic tangent, the discontinuity in the contact formulation is avoided and the solver is able to perform.

3.5 Soil and Tire Parameter Identification

This section goes over the different tests that were performed to obtain the required tire and soil parameters to run the tire model developed. Moreover, it gives some background on the indoor terramechanics rig at AVDL at Virginia Tech, which was the rig used to validate the model.

3.5.1 Tire Parameters

Tire parameter identification is a complicated task. As it was mentioned previously, the large number of tire parts makes it really difficult to characterize it. Moreover, different kind of testing procedures might yield different testing results. In an effort to minimize this discrepancy, this section will detail the tests needed to identify the tire parameters required to run the model.

Ideally, dynamic tire parameters would be desired; however, due to the lack of equipment available for this project, this is not feasible. As such, tire parameter identification was done for static conditions. Due to the fact that the case scenarios being ran in the thesis are all for steady state low velocity simulations it is not critical that the parameters be determined in a dynamic matter. However, if high speed or transient dynamic will be carried out, it is highly recommended to do dynamic testing for parameter identification since tire vibration becomes a determining factor at high speeds. The parameters required to run the model are shown in Table 3-2.

Table 3-2. Definitions of the required tire parameters required to run the model

Element	Definition
k_1 & c_1	Sidewall radial spring stiffness and damping coefficient (in-plane)
k_2 & c_2	Wheel-sidewall circumferential spring stiffness and damping coefficient (in-plane)

k_3	Inter-element radial spring stiffness (in-plane)
k_4 & c_4	Circumferential inter-element spring stiffness and damping coefficient (in-plane)
k_5 & c_3	Lateral inter-element spring stiffness and damping coefficient (out-of-plane)
k_6 & c_5	Radial inter-element spring stiffness and damping coefficient (out-of-plane)
k_7 & c_7	Sidewall-wheel lateral elements and damping coefficient (out-of-plane)
k_8 & c_6	Circumferential inter-element elements and damping coefficient (out-of-plane)
m_{rim}	Wheel mass
$m_{sidewall}$	Sidewall mass (both sidewalls)
m_{belt}	Belt mass
m_{tread}	Tread mass
b	Tire width
R_u	Undeformed tire radius
h	Tread height

The vertical tire stiffness (k_1) was found by Anake Umsrithong and Scott Naranjo from AVDL using a quarter car test setup, shown in Figure 3-18. The tire is fixed to the test rig without any suspension or steering mechanisms. Thus, assuring that all deflections are due to tire deflection and not due to compliance in other members. Moreover, a rigid surface is also used to isolate the tire from the surface. The procedure used was the following,

1. Mark the tire at 32 different locations at equally spaced and known locations.
2. Load the tire using the hydraulic actuator and record the location of the point located at 0 degrees; the applied load should also be recorder.
3. Repeat step 2 for different loads.
4. Once all desired loads are tested, rotate the tire by 90 degrees and repeat steps 2 and 3 recording the location of the point at 90 degrees. Rotating the tire and performing all the measurements again will reduce the experimental error due to any deformities in the shape of the tire or errors in the marking of the tire. This procedure should be repeated for tire locations of 0, 90, 180 and 270 degrees.
5. Average the location of each point for their respective applied load.

Once all these steps have been performed, a load versus deformation plot like the one in Figure 3-19 was created. The slope of this line should be the effective total vertical stiffness of the tire. It is important to note that this line will not always be perfectly straight since the tire has a non-linear behavior. In order to translate the total vertical stiffness to k_1, this value has to be divided by the number of masses in contact to obtain k_1.

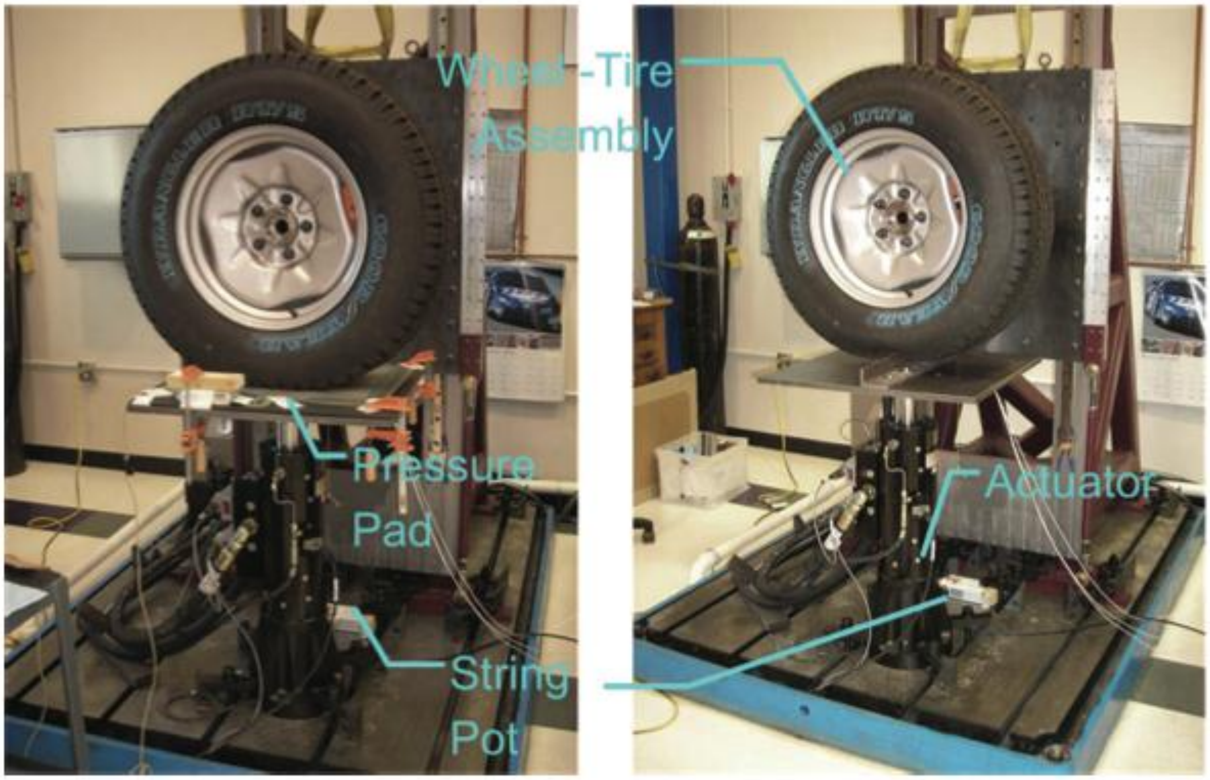

(a) (b)

Figure 3-18. Test setup used to determine tire parameters. (a) Flat surface loading. (b) Point loading. Image taken from [42]

To obtain the value of the inter-element radial stiffness (k_3) rigid cleats should be used, which are shown in Figure 3-18b. The same procedure for determining the vertical stiffness should be used, however, instead of using flat ground, a single rigid cleat should be used. This cleat creates a deformation in one of the points of the tire; thus, we are able to determine the displacements at adjacent points. The displacement at these two points should then be averaged and plotted against the applied load to determine k_3.

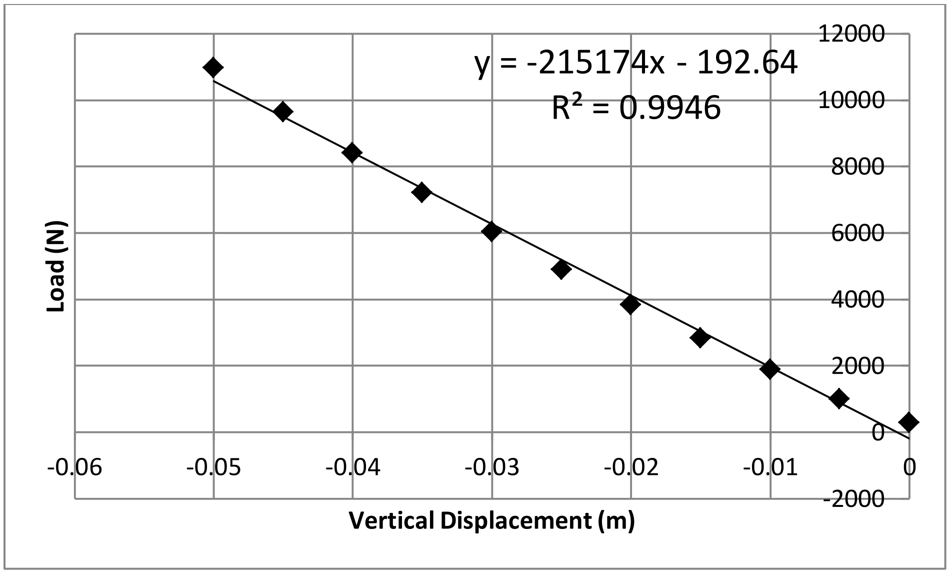

Figure 3-19. Vertical displacement as a function of mean load applied

Finding the value of the inter-planar radial stiffness (k_6) requires a procedure really similar to that of k_3. Nevertheless, instead of having the cleat going all the way along the width of the tire, it should only be in contact with the center of the tire. This allows for the recording of the displacements along the sidewalls of the tire.

For the lateral stiffness of the tire (k_5 and k_7) the same kind of tests should be performed. Nonetheless, the tire should be oriented laterally, so the lateral deformation in the tire can be recorded.

The circumferential parameters (k_4 and k_8) are the hardest parameters to identify. Ideally, these parameters can be found by cutting a section of the tire and stretching it to determine the stiffness. However, if this is not possible, then the same tests performed to obtain k_1 should be performed. Nonetheless, the displacements in the circumferential direction should be recorded, which was the approach used in this research.

3.5.2 Soil Parameters

This section gives some background for the conventional methods used for soil parameter identification. Moreover, it also presents and discusses the methods used in this thesis to obtain the soil parameters.

The soil parameters needed to run this model are presented in Table 3-3.

Table 3-3. Parameters required to run the model and their respective method of determination

Parameter	Equation	Method
Cohesion (c)	Shear Stress - Janosi/ Hanamoto	Bevameter
Angle of friction (ϕ)		
Shear deformation parameter (k_x *and* k_y)		
Index of static pressure (n)	Pressure-sinkage - Bekker	
Coefficient of cohesion (k_c)		
Coefficient of friction (k_ϕ)		
Index of dynamic pressure (m)	Pressure-Sinkage - Grahn	Modified bevameter
Soil Density (γ)	Bulldozing Force	Drive cylinder
Multipass coefficients (c_1,γ_{s1}, k_{x1}, c_{sd}, γ_{sd}, and k_{sd})	Multi-pass – Holm/Senatore	Experimental testing

Ideally, the Bekker parameters are determined using a bevameter. The bevameter is a device that uses different sized plates to record the pressure-sinkage relationship [63]. The bevameter also uses shear rings to determine the parameters needed to use the Janosi/Hanamoto equation for shear stress. On the other hand, the index of dynamic pressure can be obtained using a modified bevameter [27]. The bevameter needs to be able to control the rate of penetration in the vertical direction.

Once the bevameter tests have been performed different techniques are used to process the data and identify the parameters. Apfelbeck et al. in [6] uses a general minimization problem to identify the parameters. Wong in [4] uses the weighted least squares technique to derive the Bekker parameters. Nevertheless, regardless of the methods used to determine the parameters, at least two different tests need to be performed using different sized plates. However, repetitions lead to more reliable parameter identification.

The soil used for the validation of this experiment is classified as silky sand (SM) by the Unified Soil Classification System (USCS; ASTM D2487), as A-2-4 in the American Association of

State Highway and Transportation Officials System (AASHTO; ASTM D3282), and as "*loamy sand*" in the United States Department of Agricultural System (USDA). The specific soil data obtained can be found in the appendix. As it can be observed in Figure 3-20 this type of soil is made up of primarily sand and silt. According to the U.S. Army Engineer Waterways Experiment Station [70], in general, silky sands have low or no plasticity. From the tests performed on soil from the terramechanics rig at AVDL, Schnabel Engineering also confirmed this claim by finding that the Plasticity Index (PI) of the soil is 0.

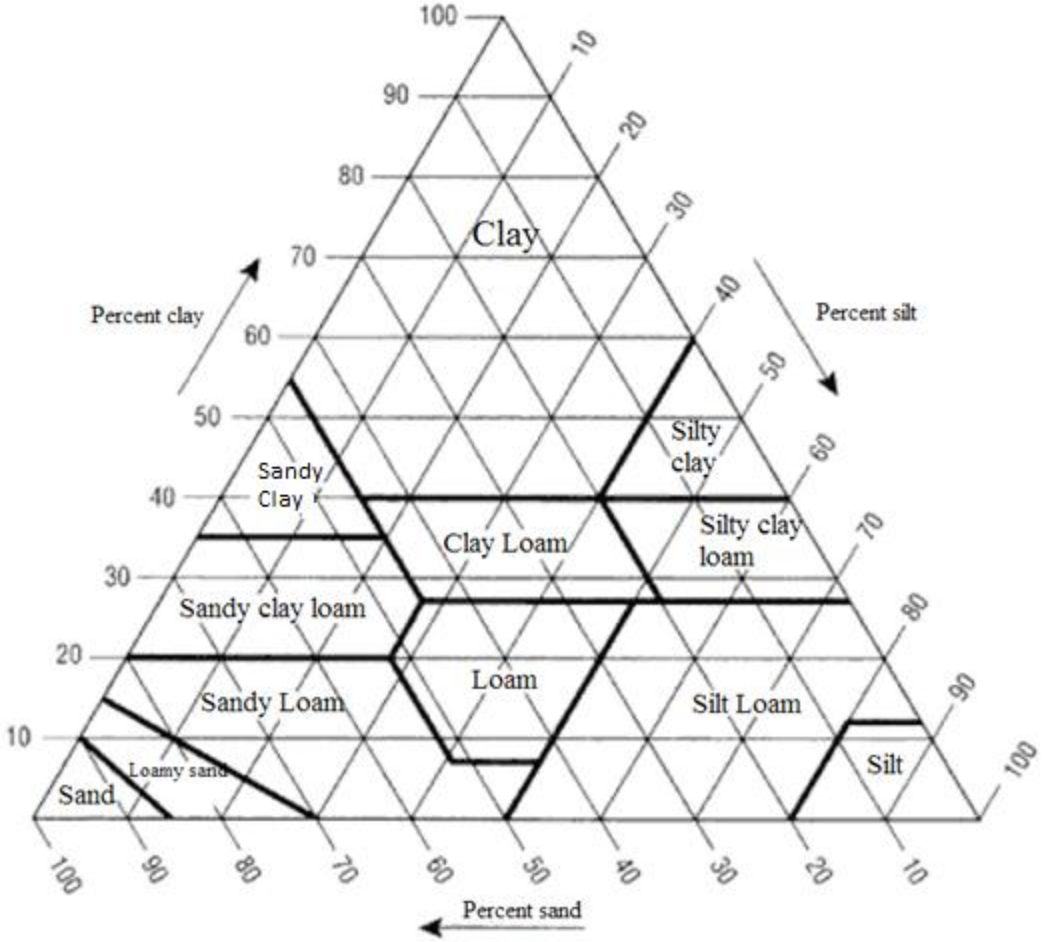

Figure 3-20. USDA soil particle size classification [5]

The procedures performed on the soil to obtain the parameters necessary to run the model are all standard procedures used in the civil engineering environment. This was done for the following reasons: (i) to be accurately understood and repeated by labs worldwide and (ii) because we did not have the capabilities to perform our own tests; thus, the tests were performed by a highly qualified geotechnical laboratory that specializes in soil testing for civil engineering applications (Schnabel Engineering).

Given the capabilities of Schnabel Engineering the first test performed was the gradation curve test and it was done to classify the soil according to the different standards mentioned previously. Following those tests, the Atterberg Limits (ASTM D4318) were investigated in an attempt to quantify the optimal moisture content and to determine feasible densities that could be achieved. Other tests performed were the California Bearing Ratio Test (ASTM D1883), 1-D Consolidation Test (ASTM D2435), and unconsolidated, undrained (UU) triaxial shear tests (ASTM D2850).

The California Bearing Ratio (CBR) test was used as a substitute to using a bevameter. This setup is really similar to a bevameter; thus, the Bekker parameters were derived from experiments using this test. On the other hand, the triaxial shear tests were used to determine the Janosi and Hanamoto parameters for shear strength. An unconsolidated-undrained triaxial compression test was chosen over consolidated-undrained or consolidated-drained because the unconsolidaded-undrained stress state is somewhat representative of soil-tire interaction conditions. Finally, the soil density can be found using a drive cylinder (ASTM D1556 and D2167).

The procedure used for parameter identification of Bekker parameters in this report follows that of Wong in [12] where at least two pressure-sinkage curves are obtained,

$$p_1 = \left(\frac{k_c}{b_1} + k_\phi\right) z^n \tag{3.76}$$

$$p_2 = \left(\frac{k_c}{b_2} + k_\phi\right) z^n \tag{3.77}$$

These equations are then transferred to the logarithmic scale,

$$\log p_1 = \log\left(\frac{k_c}{b_1} + k_\phi\right) + n \log z \tag{3.78}$$

$$\log p_2 = \log\left(\frac{k_c}{b_2} + k_\phi\right) + n \log z \tag{3.79}$$

Plotting these two curves it is evident that the exponent of static deformation is found from the slope of these two straight lines. Furthermore, at a sinkage of 1 the pressure is determined by the following equations,

$$(p_1)_{z=1} = \frac{k_c}{b_1} + k_\phi = a_1 \tag{3.80}$$

$$(p_2)_{z=1} = \frac{k_c}{b_2} + k_\phi = a_2 \tag{3.81}$$

Since the pressures and the widths of the plates are known, the only two unknowns are k_c and k_ϕ, which can be solved for using equations (3.82) and (3.83).

$$k_\phi = \frac{a_2 b_2 - a_1 b_1}{b_2 - b_1} \tag{3.82}$$

$$k_c = \frac{(a_1 - a_2) b_1 b_2}{b_2 - b_1} \tag{3.83}$$

On the other hand, to identify the Janosi and Hanamoto shear stress-shear displacement relationship parameters, a method discussed by Wong in [71] is used. This method uses the principle of weighted least squares to calculate the shear deformation parameter (K).

$$K = \frac{\sum \left(1 - \frac{\tau}{\tau_{max}}\right)^2 j^2}{\sum \left(1 - \frac{\tau}{\tau_{max}}\right)^2 j \left[\ln\left(1 - \frac{\tau}{\tau_{max}}\right)\right]} \tag{3.84}$$

where τ_{max} is the maximum shear stress and τ and j are the shear stress and corresponding shear displacement. The angle of friction and cohesion of the soil can be obtained through direct measurements.

The tests were all performed for quasi-static conditions and only accounted for plastic deformation. However, in the future it would be beneficial to introduce the elastic properties of the soils. Researchers like Hicher [72] and Sitharam et. al. [62] have investigated the dynamic and elastic properties of soil with really interesting conclusions. Nonetheless, there research is mostly focused on geotechnical and civil engineering applications.

3.5.2.1 Terramechanics Indoor Rig

Soft soil tire testing is a challenge and it is due to the fact that the reproduction of testing conditions is really difficult. Bekker [17, 18] at the Land Locomotion Lab was one of the first researchers to perform soft soil testing in a controlled environment. However, more recently other researchers, such as Kawase/Nakashima/Oida [73] and Yahya et al. [74], have constructed dedicated facilities to the investigation of soft soil tire testing. The testing rig that was used in this thesis is that of AVDL at Virginia Tech [75]; a picture of the rig is shown in Figure 3-21.

Figure 3-21. Picture of the indoor terramechanics rig at Virginia Tech. Notice the Kistler wheel hub sensor

The terramechanics rig at Virginia Tech was built between 2005-2007 and it is a very good tool to perform single wheel indoor testing. The rig is equipped with a wheel hub mounted Kistler

P650 system that is able to determine the forces and moments in all three directions at the wheel. Moreover, the rig has two independently driven motors that control both the longitudinal speed of the carriage and the angular velocity of the wheel. Thus, the rig is able to perform tests at varying slip ratios. The rig can also accommodate different camber angles (0-8°) and toe angles (±45°). Another good feature of the rig is that it has a variable soil vane, this makes it really versatile in that it can accommodate for different soils without there being a height boundary condition. The only downside of the rig is that it is only 25ft in length and has a maximum velocity of 2 miles/hour, which is a low speed. Furthermore, the testing facilities at Virginia Tech also have access to a Tekscan I-Scan 3150 pressure pad, which is used to measure normal load as well as pressure distribution. Moreover, different cone penetrometers are also available to ensure consistent compaction levels.

As it was previously mentioned, the repeatability of soil testing is really important to the accuracy of the results. As such, the soil preparation methods used follow a similar approach as those used by Taylor in [76] , which consists of (i) disturbing the soil, (ii) raking the soil, (iii) smoothing and leveling of the soil, (iv) compaction of the soil, and finally (v) another compaction with the roller. The steps of this process were developed by Scott Naranjo, and they are documented in Figure 3-22.

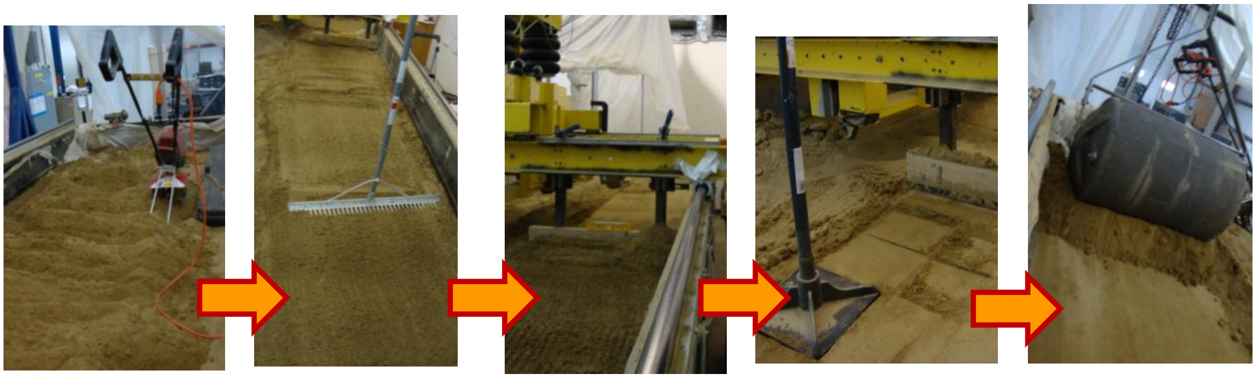

Figure 3-22. Soil preparation procedures used to ensure consistent testing conditions

4 Case Studies and Simulation Results

This section first introduces the tire and soil parameters used for all the simulations. It then presents the results for the dynamic loading of the tire on rigid ground. The experimental results are compared to the simulation results in an effort to validate the tire deformation. The succeeding section presents a case study for dynamic settling on sandy loam. Consequently, case studies for pure lateral, pure longitudinal and combined slip scenarios are discussed. Finally, a case study for repetitive loading is analyzed.

4.1 Tire and Soil Parameters

The tire chosen for the validation of this model is Michelin LTX A/T 2 tire (235/85R16), as shown in Figure 4-1. According to Michelin of North America [77] this is an all season off-road tire for a light truck. It has a max load of 3042lbs (13,531N) at 80psi (551.6kPa) (load index 120) and a speed rating of R.

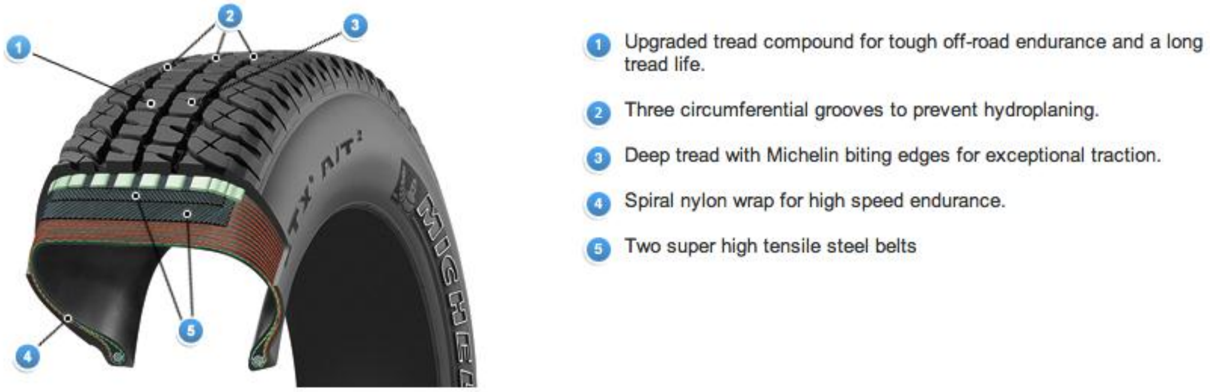

① Upgraded tread compound for tough off-road endurance and a long tread life.
② Three circumferential grooves to prevent hydroplaning.
③ Deep tread with Michelin biting edges for exceptional traction.
④ Spiral nylon wrap for high speed endurance.
⑤ Two super high tensile steel belts

Figure 4-1. Michelin LTX A/T 2 tire used for the model validation [77]

Due to the fact that we didn’t have enough test data for this tire, the parameters used are a mixture of measured and approximated values. All damping coefficients were approximated based on a recommendation made by Mr. Michael Gipser from FTire; thus, the damping coefficients are between 1-3% of the stiffness values in the respective direction. The lateral tire stiffness was provided by Dr. Said Taheri as an approximation based on a very similar tire. The sidewall, belt and tread masses are estimations based on the total mass of the tire. The remaining values were obtained by experimental means using the techniques presented in section 0.

Table 4-1. Tire parameters used for all simulations. Note that all this parameters need to be divided by the number of masses in contact and m_{total} is the total mass of the tire

Parameter	Value
m_{total}	19.83 kg
m_{rim}	11.52 kg
$m_{sidewall}$	m_{total}*(2/3) kg
$m_{belt} + m_{tread}$	m_{total}*(1/3) kg
b	0.2362 m
R_u	0.3937 m
h	0.0135 m
k_1	215,172 N/m
k_2	248,136 N/m
k_3	10^5 N/m
k_4	k_2 N/m
k_5	110,889 N/m
k_6	5*10^5 N/m
k_7	110,889 N/m
k_8	10^6 N/m
c_1	k_1*0.03 Ns/m
c_2	k_2*0.02 Ns/m
c_3	k_3*0.01 Ns/m
c_4	k_4*0.01 Ns/m
c_5	k5*0.05 Ns/m
c_6	k6*0.01 Ns/m
c_7	k_7*0.01 Ns/m

The sandy loam parameters were found from a source written by Wong [12], since at the time this thesis was written the extraction of the soil parameters for the sandy loam used in the terramechanics rig was still on-going. It is important to note that the index of dynamic pressure could not be found either through experimental testing or literature; therefore, the Grahn pressure-sinkage equation, although implemented in the code, cannot be used. As such, all the simulations presented in this paper use the Bekker formulation. Grahn's equation can be employed as soon as the missing parameters are experimentally obtained.

Table 4-2. Soil Parameters used for all simulation

Parameter	**Sandy Loam (11% Moisture Content)**
Cohesion (c)	**4830 Pa**
Angle of friction (ϕ)	**20°**
Index of static pressure (n)	**0.9**
Coefficient of cohesion (k_c)	**52,530 Pa**
Coefficient of friction (k_ϕ)	**1,127,970 Pa**
Shear stress stiffness (k_x & k_y)	**0.015 m**
Index of dynamic pressure (m)	**--**
Soil Density (γ)	**1258 kg/m^3**

4.2 Dynamic Settling

The dynamic settling of the tire is a really important step in the simulation because equilibrium needs to be attained between the tire and the soil. Moreover, the dynamic settling of the tire on a rigid surface was used to validate tire deformation.

4.2.1 Rigid Surface

The first step in the validation of the model was to compare the static deflection of the tire with the experimental data. The data used in this thesis was collected by Anake Umsrithong from Virginia Tech and it was collected for the same tire used in the soft soil validation. However, it is important to note that only the belt deformation will be validated since no data is available for the sidewall deformation. As such, for tire deflection validation purposes, the model was ran using only the belt and tread plane.

The setup for these tests was really simple. It consisted of loading and unloading the tire at different loads and then recording the deflection at 32 evenly spaced locations around the circumference of the tire. A picture of the test setup can be observed in Figure 4-2.

Figure 4-2. Quarter car rig testing setup used to validate static deflection

During the loading of the tire, pictures were taken perpendicular to the tire surface to use image processing to identify the deflections in the tire. Thus, two different loads where used to validate the model. The first one is an intermediate load of 5,128 N and the second is a high load of 11,022 N.

The comparison between the experimental and simulation results for the intermediate load can be observed in Figure 4-3. Each circle represents the location of the masses in the simulation and the points marked in the tire. The deformation predicted by the simulation predicts really close the deformation observed in the experimental testing (~1.14% error in the x-axis and ~6% in the z-axis).

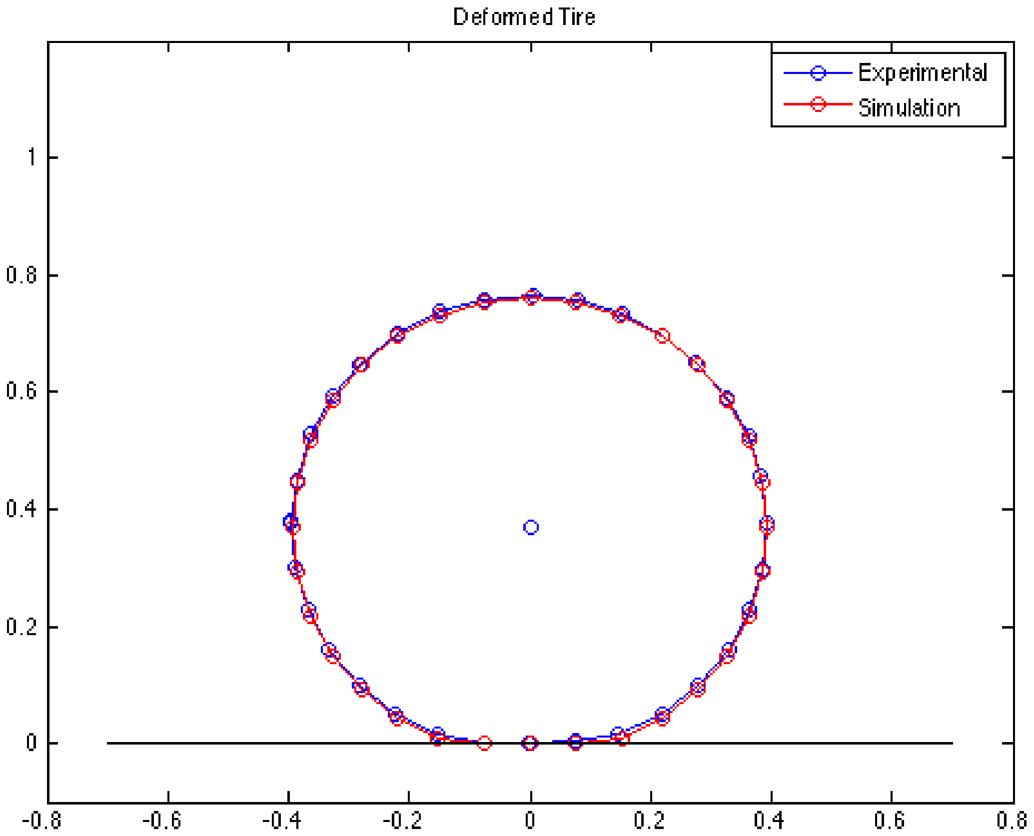

Figure 4-3. Static deflection comparison for a rigid surface under an intermediate load (5128N)

Figure 4-4 shows the deformation of the lumped masses in contact with the ground for both the radial and circumferential directions when a medium load (5,128 N) is applied. By analyzing the data it is evident that there is only a small deformation in the circumferential direction, while the largest radial deflection is around 2.5 cm.

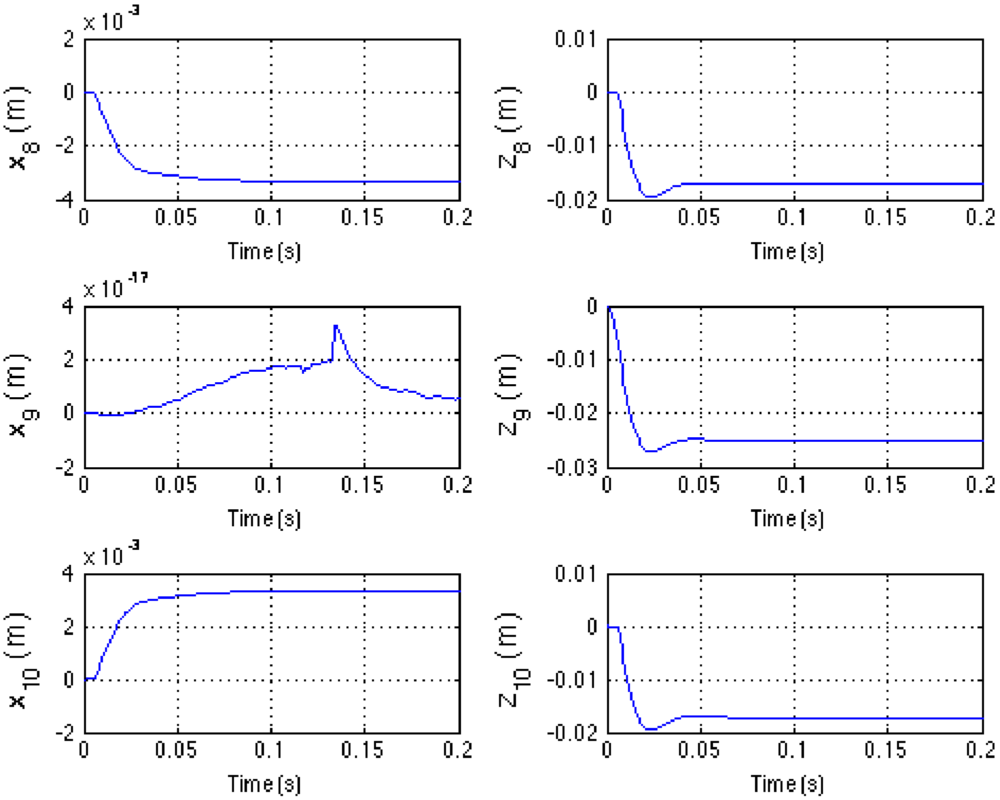

Figure 4-4. Lumped mass deformations in the circumferential (*x*) and radial (*z*) direction for masses in contact (8,9,10) at a medium load (5128N)

The results for the high load also show good agreement with the experimental data as illustrated in Figure 4-5. Moreover, by observing Figure 4-5 and Figure 4-6 it is evident that the deformation experienced by the tire is much larger for this higher load. Thus, the close resemblance between the collected data and the simulation suggests that the model is able to accurately predict tire deformation for static conditions.

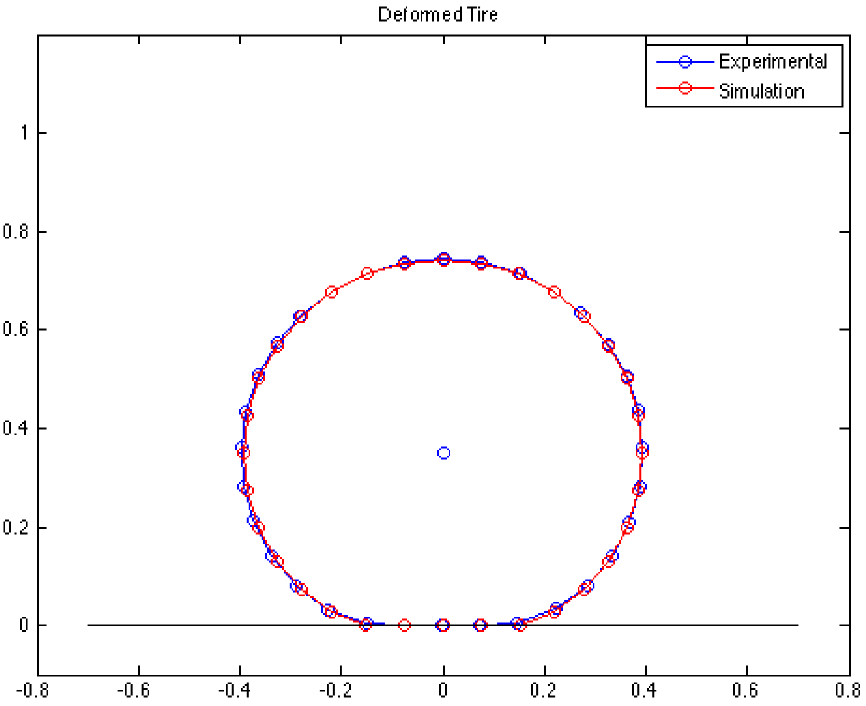

Figure 4-5. Static deflection comparison for a rigid surface under high load (11,022 N)

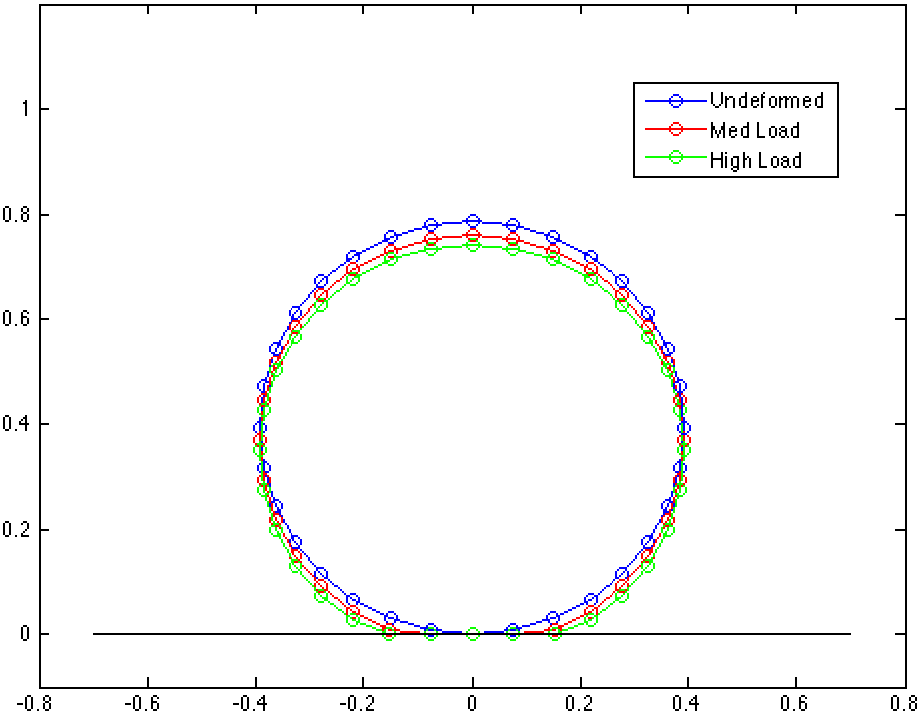

Figure 4-6. Simulation comparison of tire deformation for different loads under a rigid surface

4.2.2 Soft Soil

This section will go over the dynamic loading simulations that were done on sandy loam. The parameters for this sandy loam have already been presented in Table 4-2. Thus, the results presented in this section and the succeeding sections are more qualitative in nature. When available, the simulation will be compared to data collected in the terramechanics rig for the same tire. Even though the sandy loam being used in the simulation is the closest match to the silky sand in the terramechanics rig they are not identical, so these comparisons should not be taken as a direct validation, but more of as an indication that the tire model developed functions properly for this type of soil. Moreover, as it was mentioned previously, due to lack of soil parameters, the pressure-sinkage equation formulated by Grahn couldn't be used, as such, all the simulations in this investigation use Bekker's pressure-sinkage equation.

The dynamic loading of the tire is a really important step because equilibrium is reached between the tire and the ground. Thus, this is always the first step of the simulation. Figure 4-7 shows a plot of the vertical displacement and velocity of the wheel center as the tire is dropped into the soft ground. As expected, it can be observed that the wheel center has a larger vertical displacement as the normal load is increased. Similarly, the vertical velocity follows the same behavior.

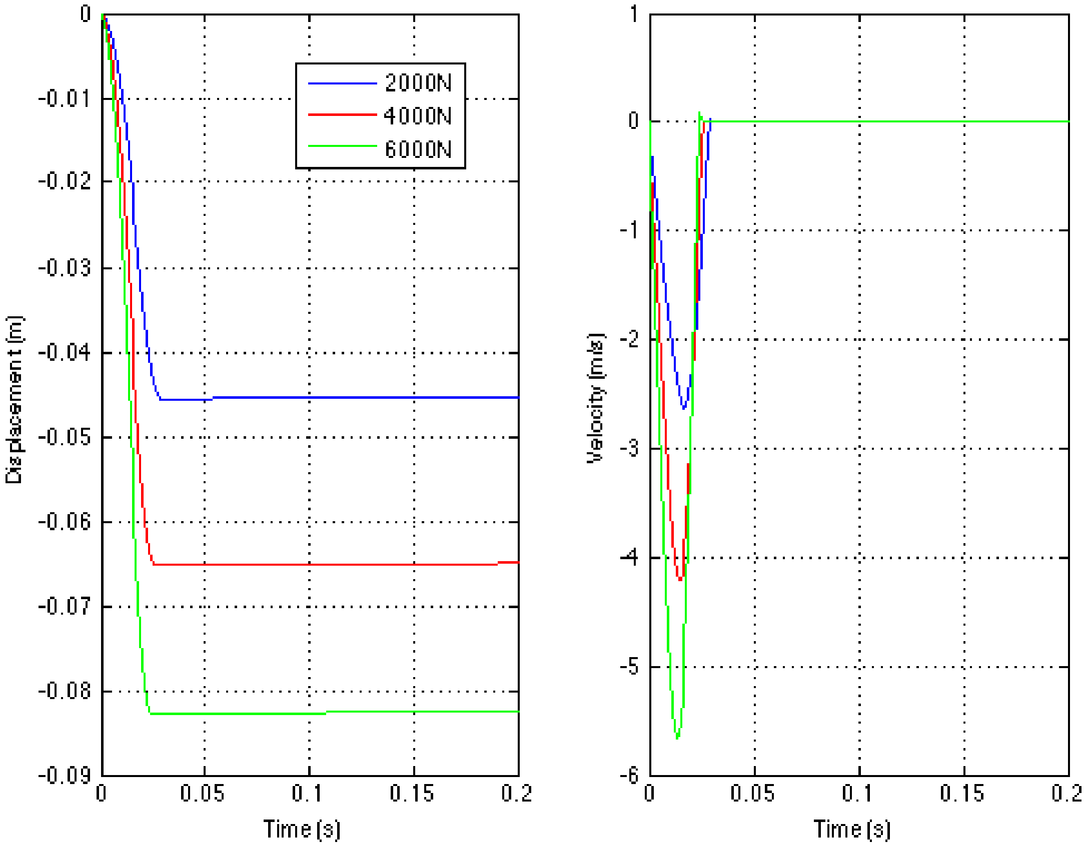

Figure 4-7. Left-Vertical displacement; Right- Vertical velocity for the rigid wheel for the dynamic settling scenario

Figure 4-8 shows the normal load fluctuation on the wheel center as the tire is dropped in the soft soil. As expected, the tire bounces slightly until it reaches equilibrium. However, by careful inspection is it evident that higher loads cause higher fluctuations. Moreover, due to the increased vertical velocity it is also observed that at higher loads the soil experiences higher pressure. It is important to note that different fluctuations were observed for different damping coefficients, however, since this thesis is not interested in the transient behavior of the tire this is not of great consequence.

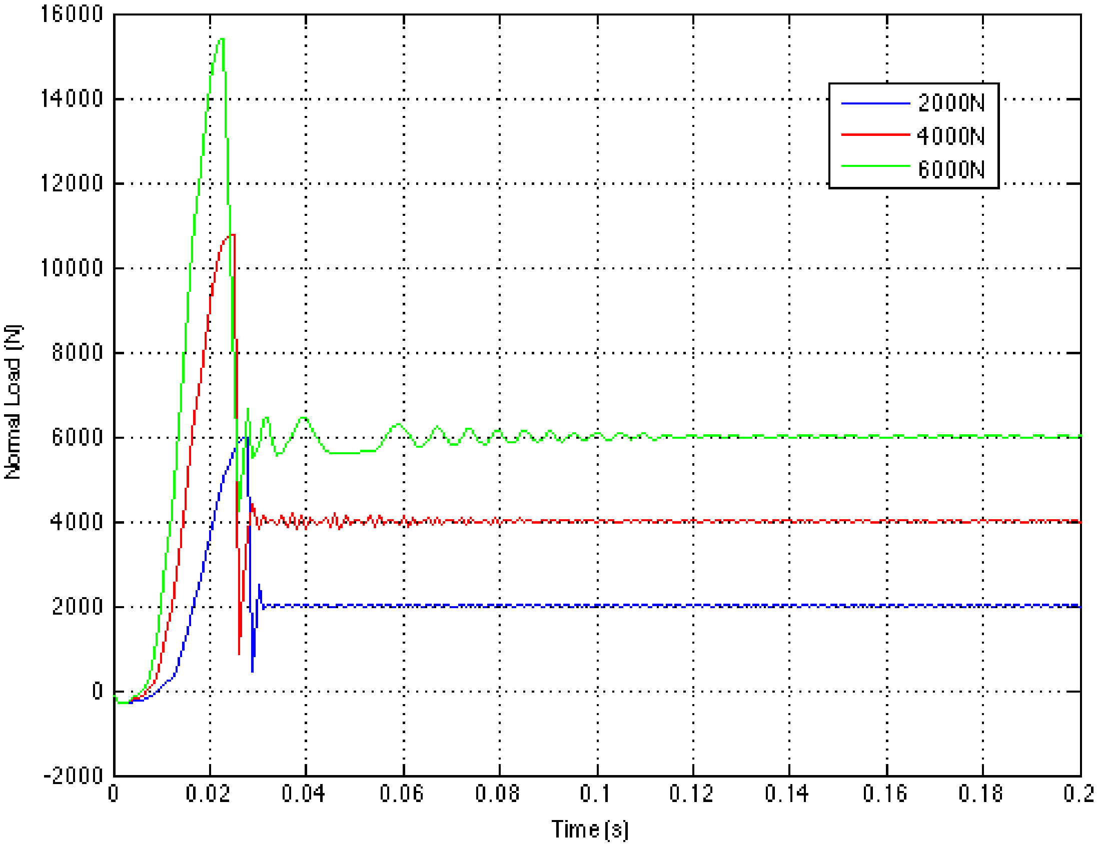

Figure 4-8. Forces at the wheel centre for the dynamic loading scenario

Besides the displacements and forces at the wheel center the model is able to predict rut height for both the sidewall and tread and belt layers. It is important to note that since a plastic model was adopted for the soil, the rut height will be equal to the sinkage of the tire. Observing the sinkage of both the sidewalls and tread and belt layers in Figure 4-9 it is evident that the belt and tread layer has a larger sinkage due to its larger radius. In Figure 4-9 the simulation results were compared to experimental data gathered in the terramechanics rig using the silky sand discussed earlier.

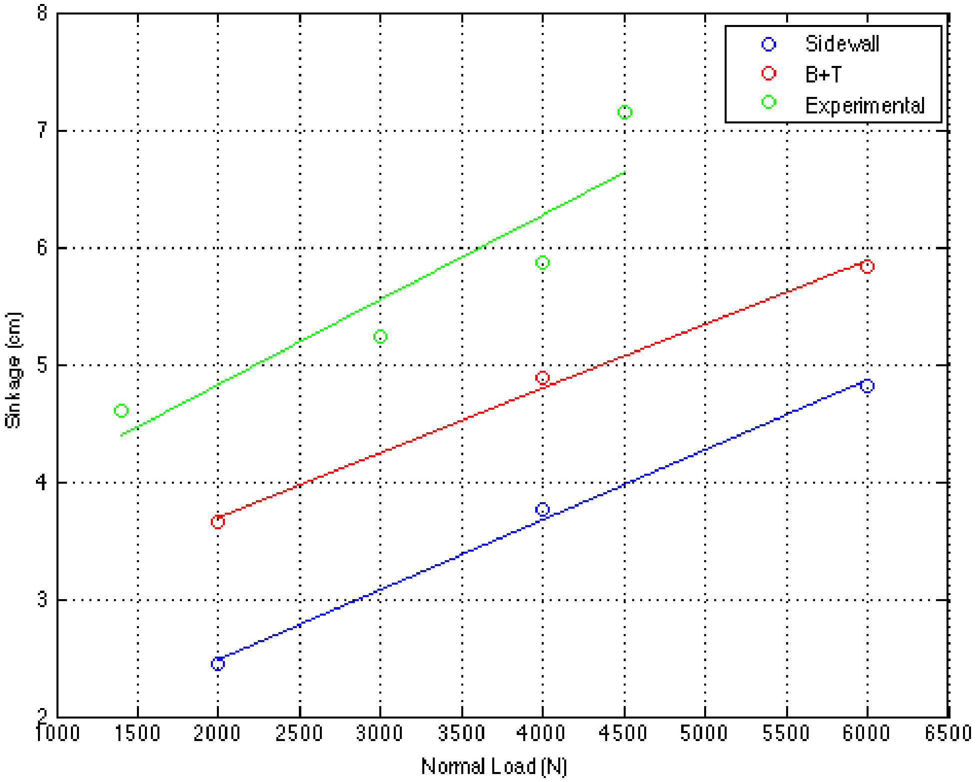

Figure 4-9. Sinkage as a function of normal load for the dynamic loading case. Note that the simulation results are obtained using a Sandy Loam (11% moisture content), while the experimental data is obtained using a Silky Sand (~2% moisture content)

Figure 4-10 shows the pressure distribution in the tire for a normal load of 6,000 N. The tire is divided into three layers; the middle layer represents the tread and belt layer, and the left and right layers the sidewalls. Each rectangle represents a lumped mass, thus, it is assumed that the pressure is the same in any location of that specific rectangle. Moreover, the color bar represents the normal pressure exerted on each lumped mass in Pascal's. By inspection, it is evident that the pressure distribution is symmetrical left-to-right, however, we can see that the pressure is higher for the tread and belt layer, which makes sense since it has a larger sinkage.

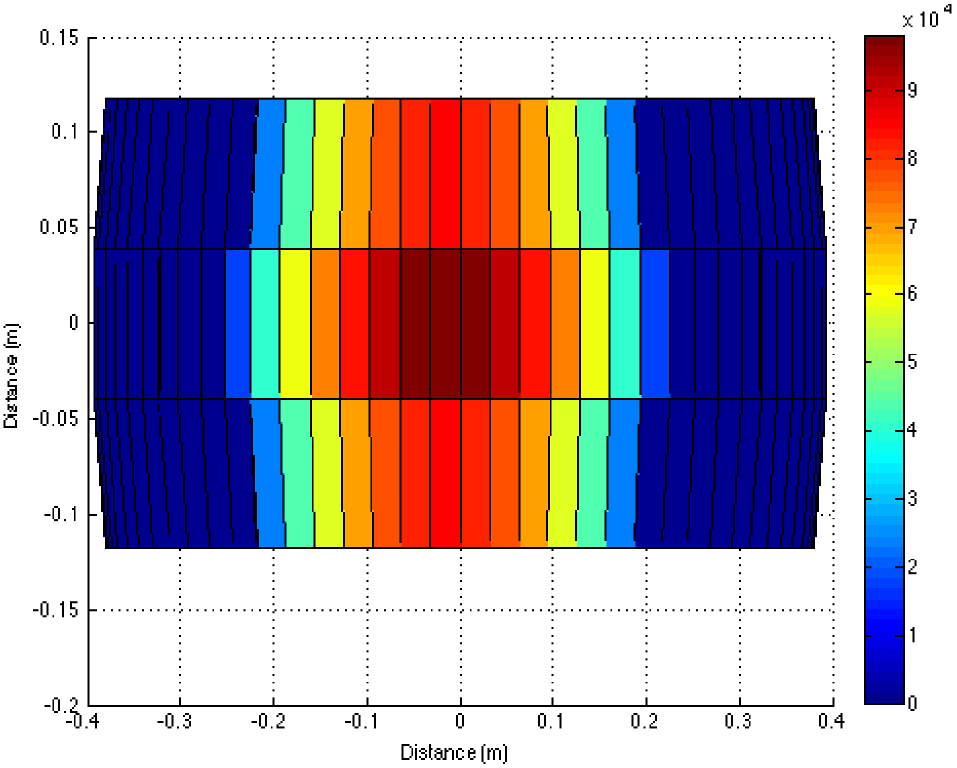

Figure 4-10. Pressure distribution for the dynamic loading case using a normal load of 6,000 N, note that the color bar represents the normal pressure in Pascal's.

Finally, in Figure 4-11 a diagram of the deformed tire is showed for the 6,000 N case. It can be observed that the tire experiences a considerable amount of deformation in the contact patch, which obviously increases with an increase in normal load.

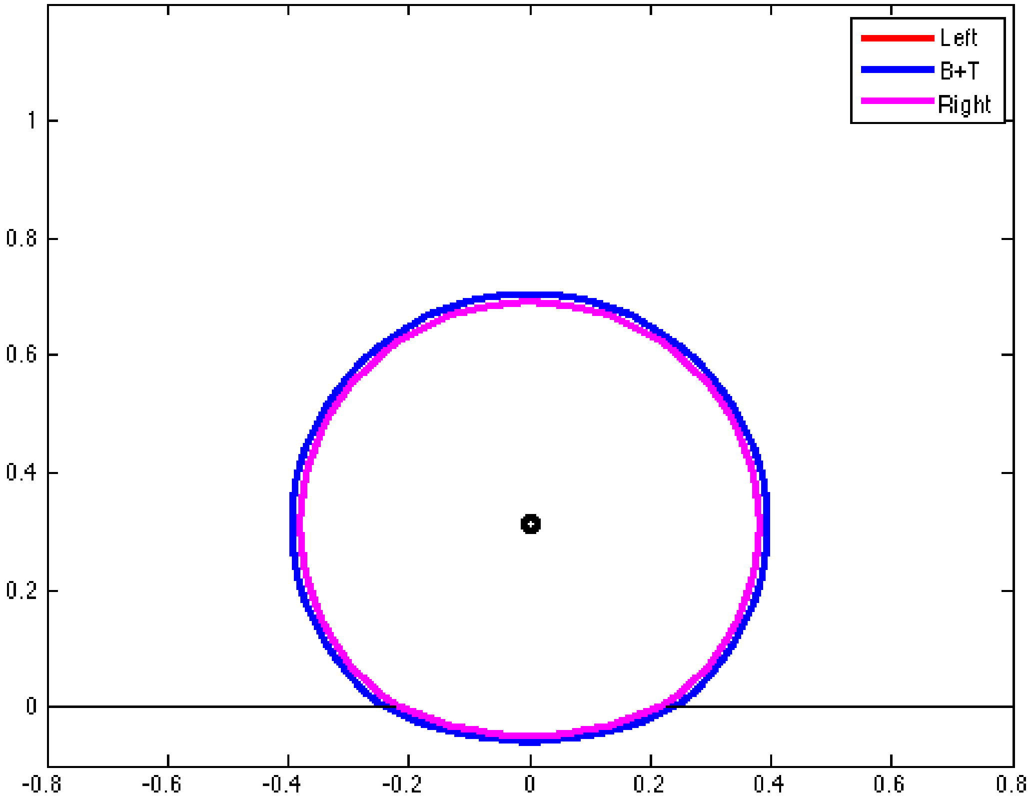

Figure 4-11. Deformed tire for the dynamic loading case using a normal load of 6,000N

4.3 Steady State - Pure Longitudinal Slip

The pure longitudinal slip case study was run using the sandy loam. For all simulations, a longitudinal velocity of 2 m/s was inputted, thus, the results presented in this section show the steady-state behavior of the tire. Furthermore, 72 lumped masses per layer of the tire model were used for all simulations.

Tire sinkage is really important when predicting the performance of off-road vehicles. Figure 4-12 shows the simulation results for sidewall sinkage at a normal load of 2,000 N for different slips. At first inspection it is evident that there is a lot of variation in the data, however, this is due to the fact that masses loss and gain contact with the ground constantly. Obviously, if the number of masses is increased it is expected that these fluctuations will decrease.

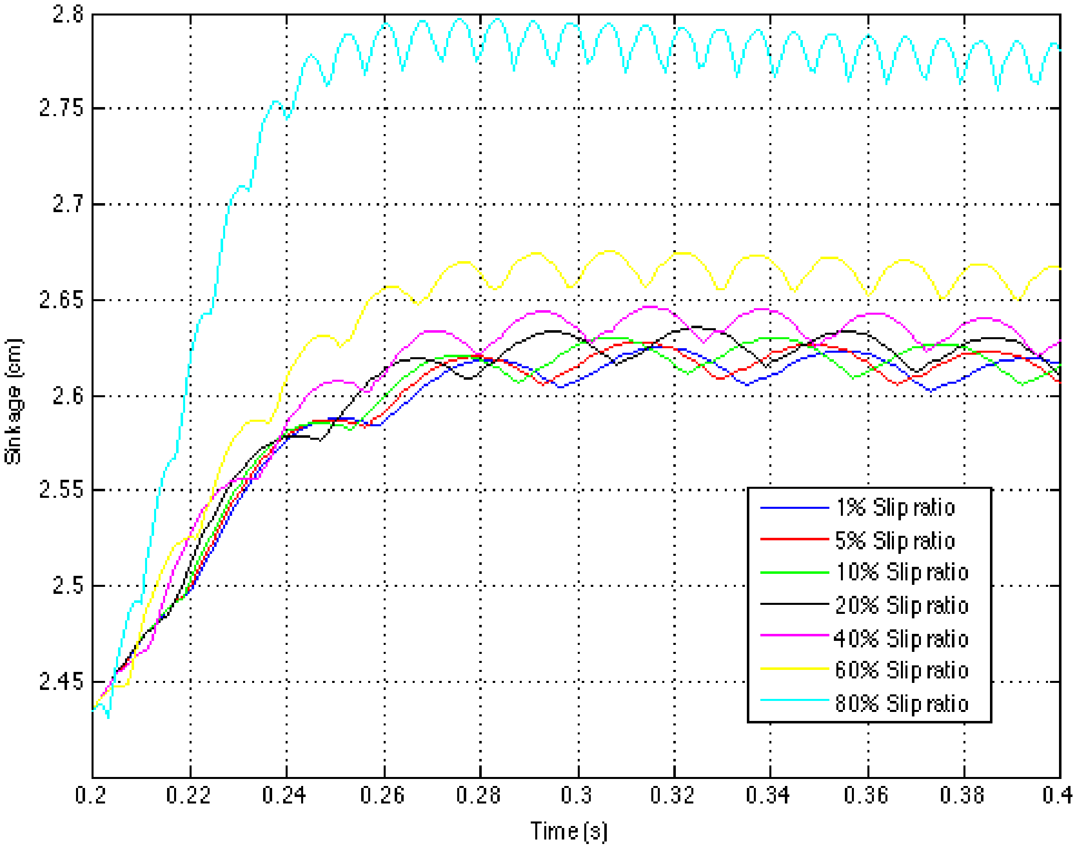

Figure 4-12. Sidewall sinkage for different longitudinal slips at a normal load of 2,000 N and zero slip angle

In order to process the data, mean sinkage values were calculated for the different normal loads and slip ratios, which are presented in Figure 4-17. In the same way as in the dynamic loading of the tire, the belt and tread layer has a higher sinkage due to its larger radius. It is also evident that sinkage has a slight increase for slip ratios of 1%-60%. However, for higher slip ratios higher sinkage is observed; this is referred as slip sinkage. Essentially, the slipping of the tire digs in the ground creating higher sinkage values.

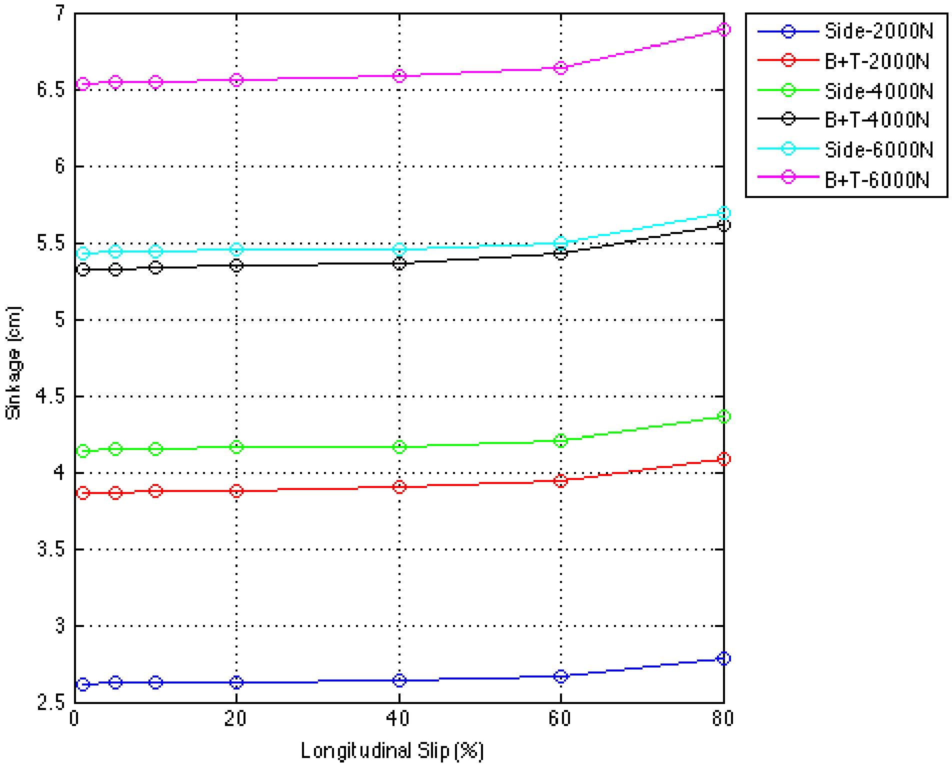

Figure 4-13. Sinkage as a function of slip for different normal loads at zero slip angle

The drawbar pull is probably the most important measure when it comes to off-road locomotion; since it predicts vehicle mobility. Figure 4-14 shows the drawbar pull as a function of time for different slip ratios at a normal load of 2,000 N. Similarly to Figure 4-12, fluctuations are observed in the data due to the loss and gain of contact of masses in the contact patch.

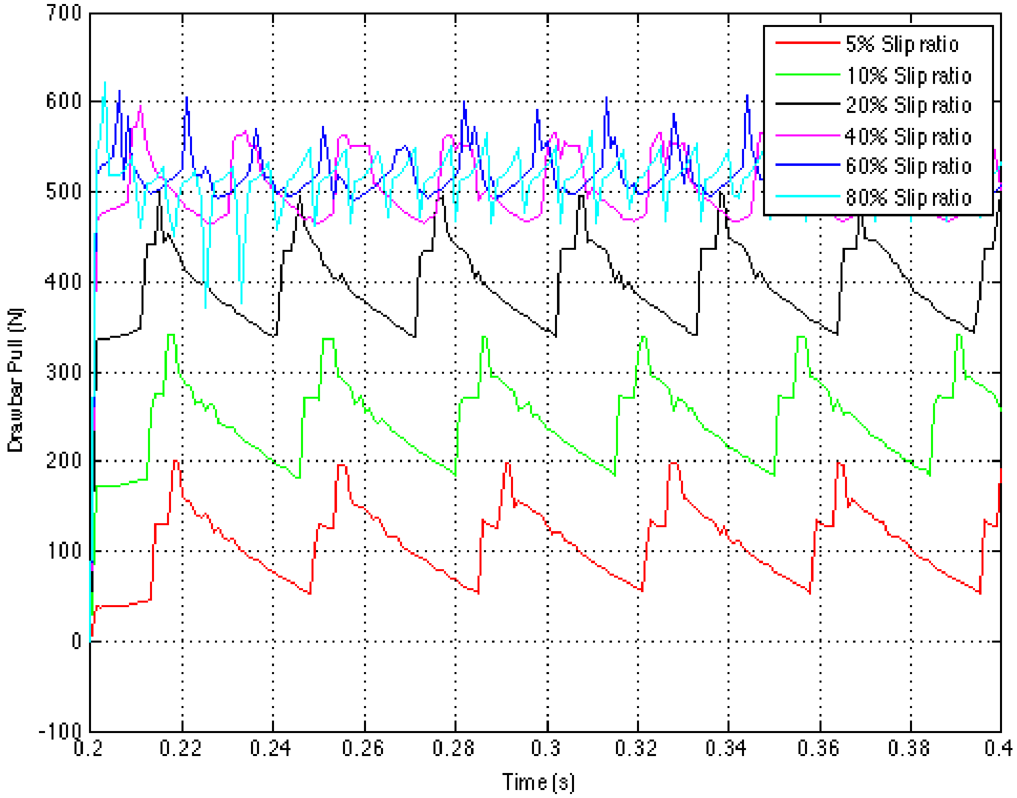

Figure 4-14. Drawbar pull for different slip ratios at a normal load of 2,000 N

As it was previously mentioned, an increase in lumped masses will decrease fluctuations, and this can be observed in Figure 4-15 and Figure 4-16. This simulation was ran using 200 masses, rather, than the standard 72 masses used for all other simulations. The fluctuations are significantly smaller for this simulation; however, the mean drawbar pull for the data set is really close to the simulation with 72 masses.

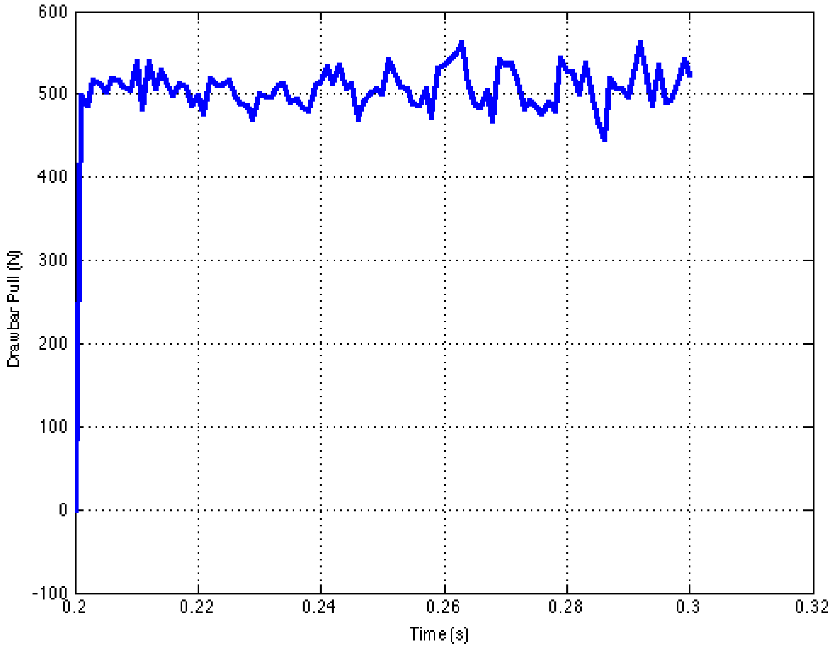

Figure 4-15. Drawbar pull as a function of time for 200 masses, a normal load of 2,000 N, and a slip ratio of 30%.

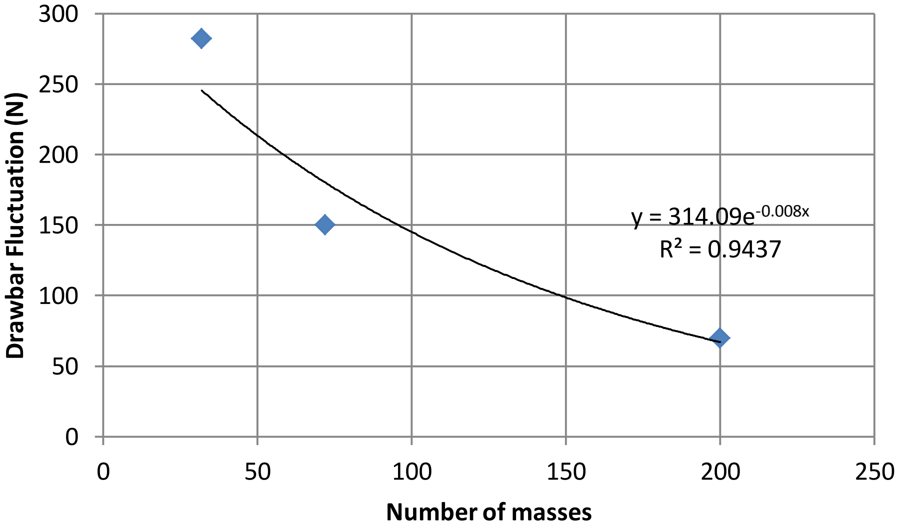

Figure 4-16. Drawbar pull fluctuation as a function of number of masses

In order to process the data presented in Figure 4-14, mean averages were calculated for each normal load and slip ratio. The result is Figure 4-17. As expected, an increase in normal load yields higher drawbar pulls. This is due to the fact that high loads create higher sinkage, thus, increasing the ground pressure and the longitudinal shear stress. Moreover, it can be seen in

Figure 4-17 that the drawbar pull increases with longitudinal slip until it reaches 40%, where it starts to decrease. This transition point defines the location where rolling resistance stops being the limiting factor, and the wheel slip becomes the limiting factor. Thus, the location of this transition point is heavily based on soil properties.

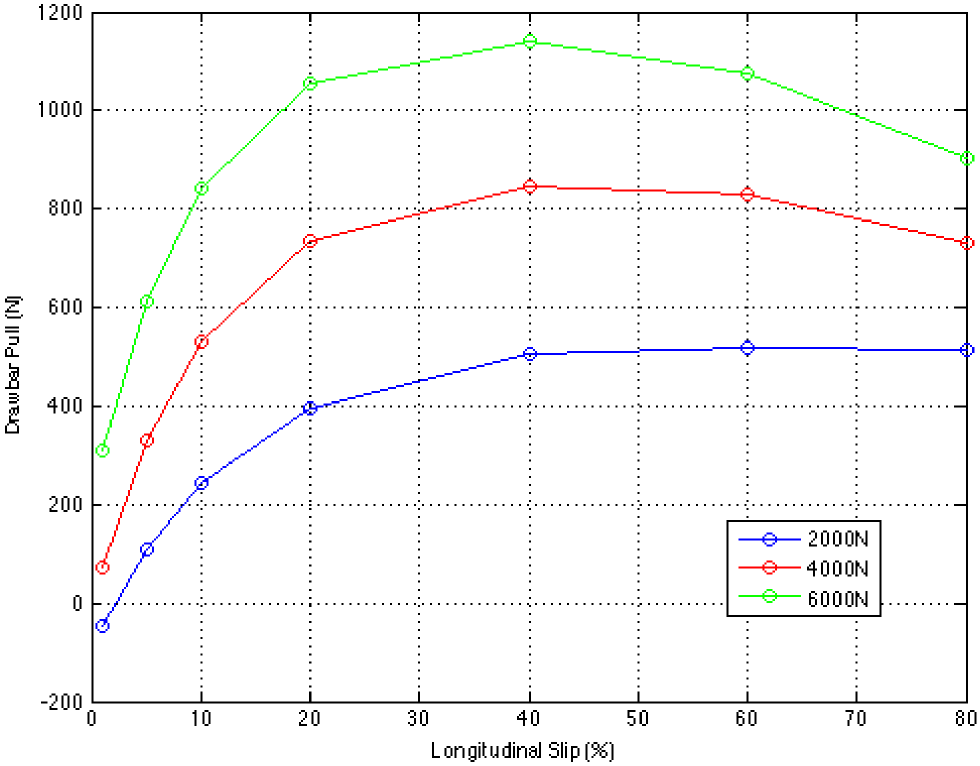

Figure 4-17. Drawbar pull as a function of longitudinal slip for different normal loads

Comparing the simulation results of Figure 4-17 with experimental data collected at AVDL in Figure 4-18 for a rigid wheel on GRC1 lunar soil simulant it is evident that the data follows a similar trend.

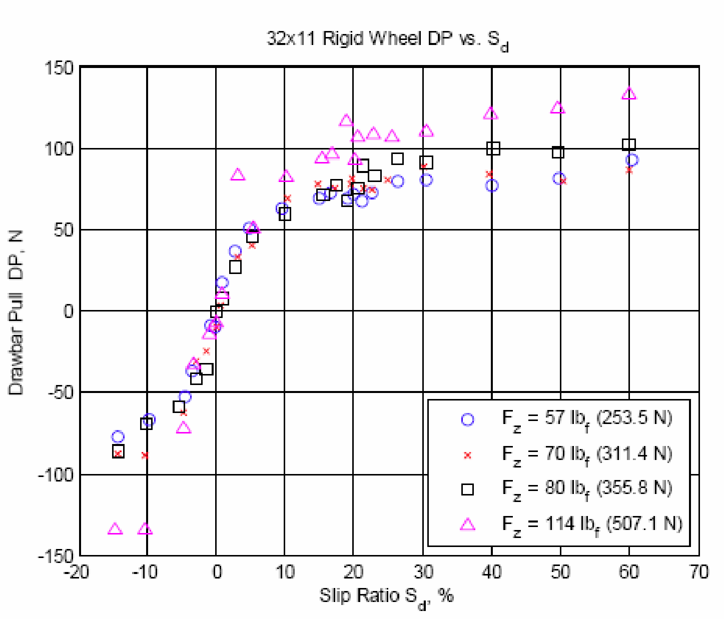

Figure 4-18. Drawbar pull vs. slip ratio for experimental results on a rigid wheel collected at AVDL using GRC1 lunar soil simulant [76]

The driving torque is another important measure when it comes to off-road mobility. Knowing the required torque to traverse a given terrain is important when determining the required power needed for a vehicle. Figure 4-19 shows the driving torque required to traverse the terrain at various normal loads and slip ratios. As expected, higher normal load yields higher torque.

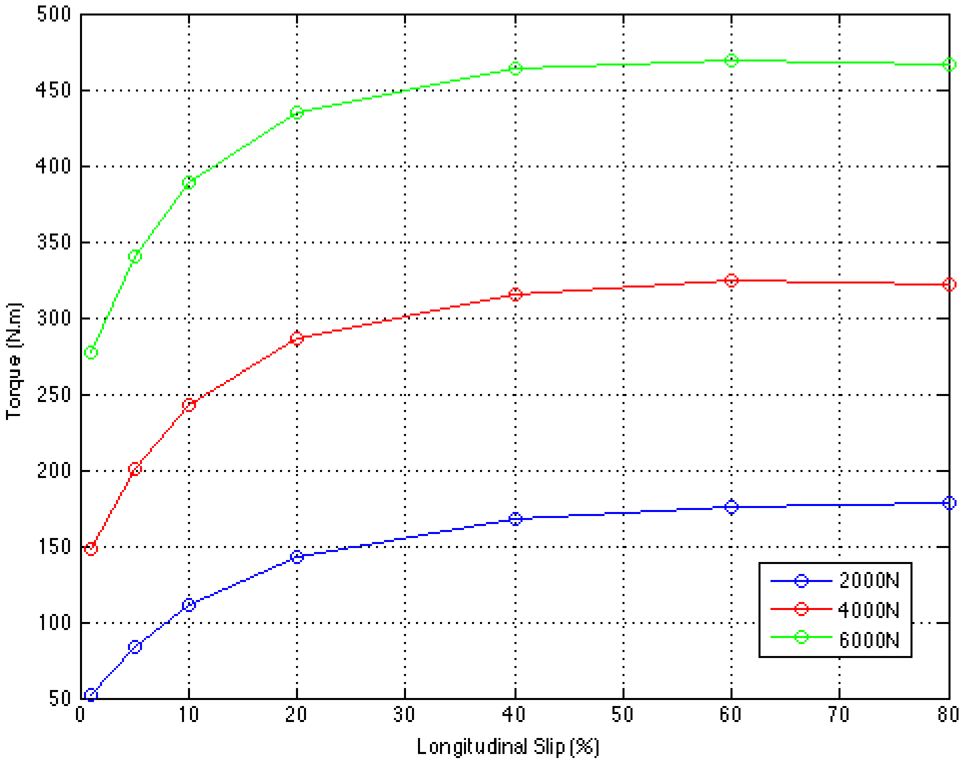

Figure 4-19. Driving torque as a function of longitudinal slip for different normal loads

The camber angle has an important influence in the prediction of soft soil locomotion. Most importantly, the camber has a large influence on the pressure distribution in the contact patch. Figure 4-20 shows the pressure distribution for a tire travelling at zero slip angle and zero camber. Similarly to Figure 4-10, it can be observed that the normal pressure is symmetric left to right. On the other hand, Figure 4-21 shows the pressure distribution for a tire travelling at 2° camber and zero slip angle. In this case, higher pressures are experienced by the right sidewall.

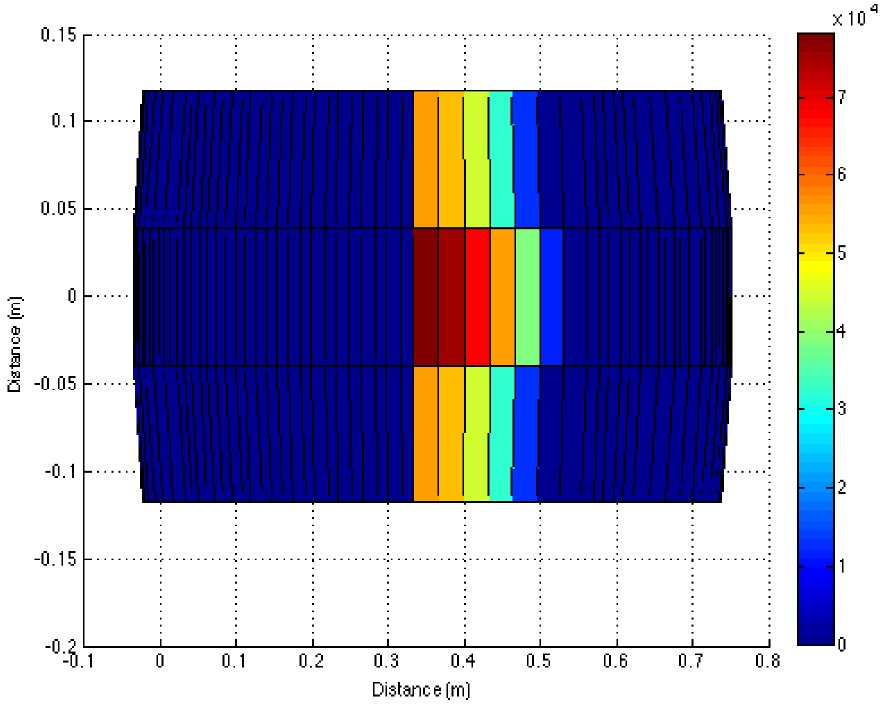

Figure 4-20. Pressure distribution for a normal load of 2,000 N and a longitudinal slip of 10% at zero slip angle, the color bar represents the normal pressure in Pascal's

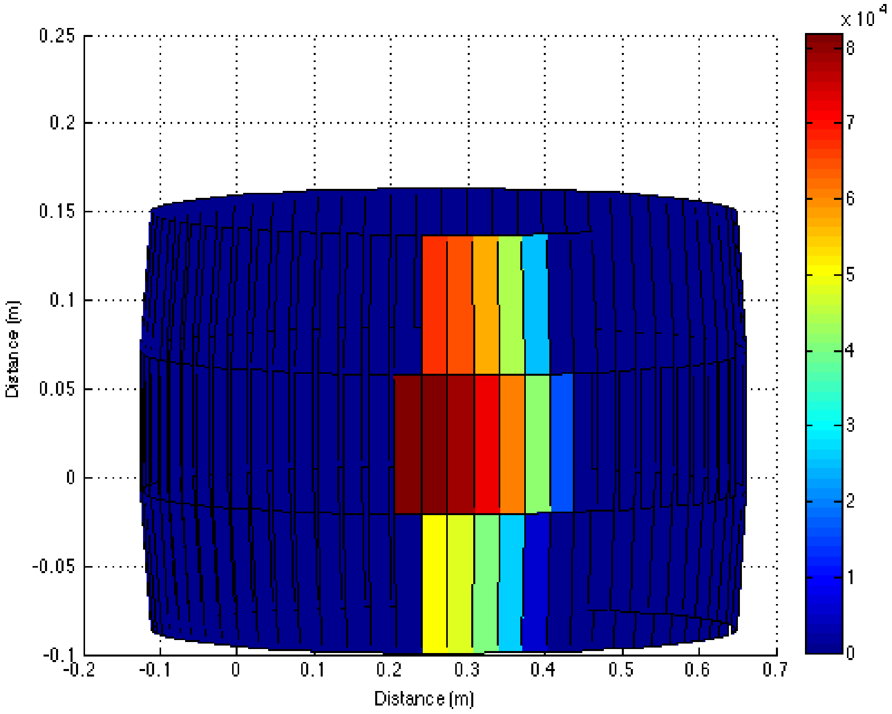

Figure 4-21. Pressure distribution for a normal load of 2,000 N, a longitudinal slip of 10%, zero slip angle and a camber angle of 2°, the color bar represents the normal pressure in Pascal's

Furthermore, the camber angle creates additional lateral forces that contribute to the overturning moment. Figure 4-22 shows both the driving torque and the overturning moment for a tire traveling with a camber angle. The driving torque is not affected by the camber angle; however, a small overturning moment can be observed. As it was previously mentioned, the fluctuations in the data are due to the change of masses in contact.

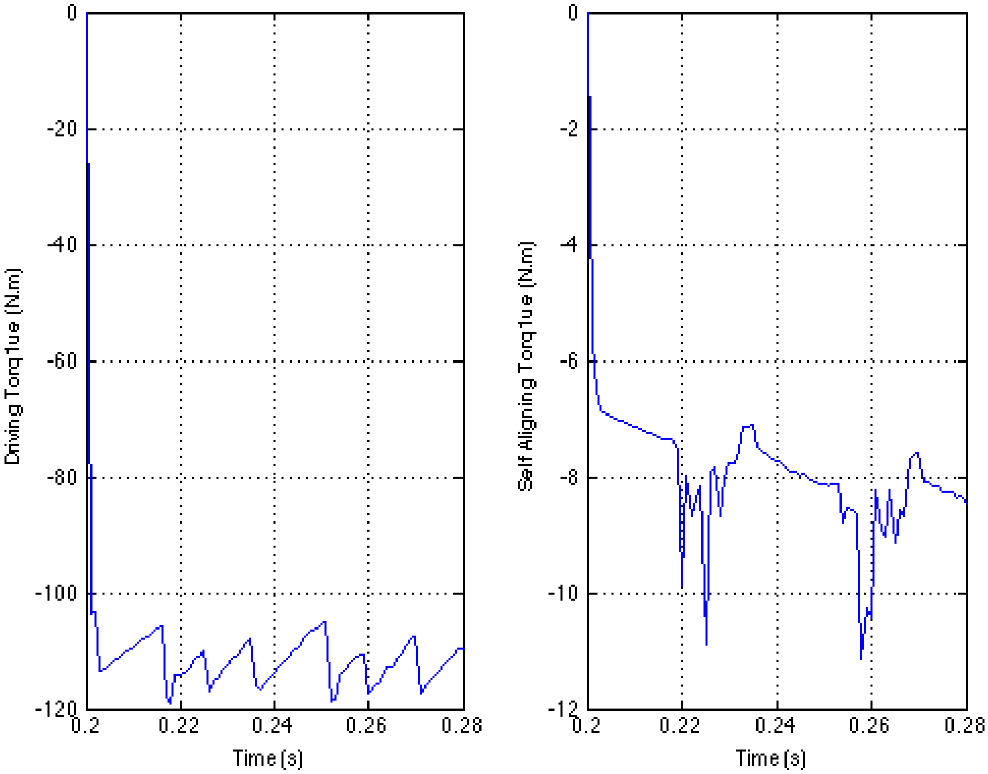

Figure 4-22. Left- Driving torque and Right- overturning moment for a normal load of 2,000 N, a longitudinal slip of 10% and a camber angle of 2°

4.4 Steady State - Pure Lateral Slip

The next case that will be investigated is the pure lateral slip. Figure 4-23 shows the lateral force as a function of slip angle for different normal loads. As expected, the lateral force increases with both slip angle and normal load. As it was shown in the previous section, higher normal load yields higher sinkage, thus, yielding higher lateral shear force. Likewise, the higher sinkage and slip angle will also increase the volume of soil displaced, consequently, increasing the bulldozing force. However, similarly to the drawbar pull plot in Figure 4-17 there is a transition point where the forces reach the soils shear strength, thus, they level out.

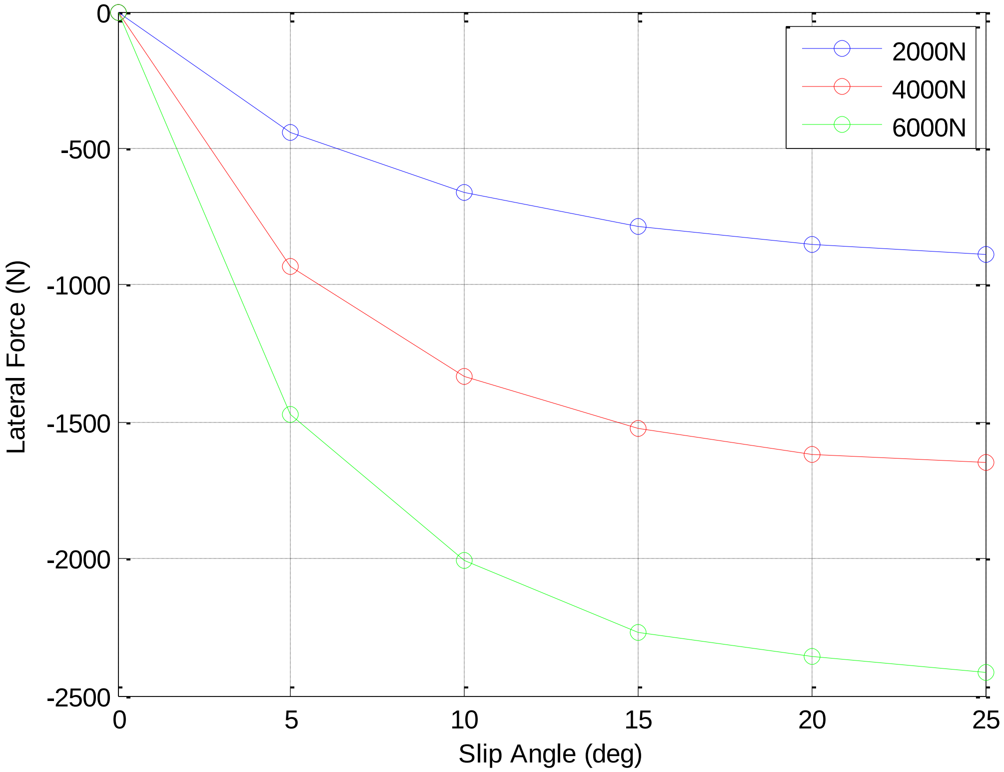

Figure 4-23. Lateral force as a function of slip angle for different normal loads at zero longitudinal slip

Figure 4-24 presents the overturning and self-aligning moments as a function of slip angle for different normal loads. It is evident that both moments follow really similar patterns; both increase with slip angle and normal load. Contrary to the lateral force, the moments start leveling out at around 25° slip angle.

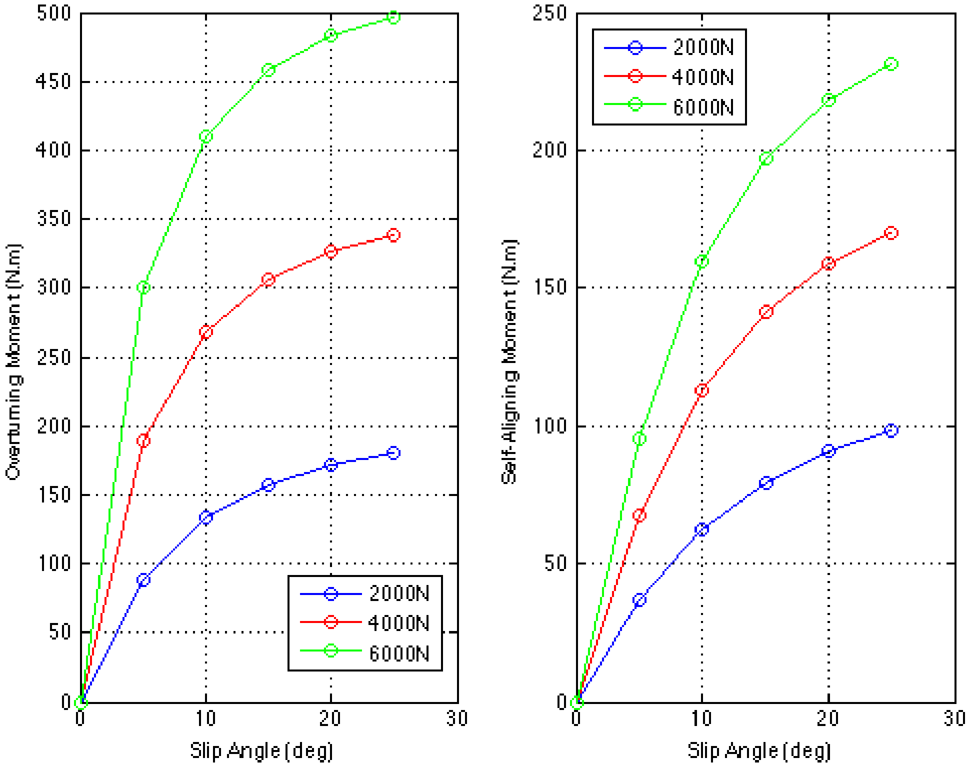

Figure 4-24. Left- Overturning moment; Right- Self-aligning moment as a function of slip angle for different normal loads at zero longitudinal slip

Finally, Figure 4-25 shows the pressure distribution for a steered tire. Due to the fact that camber is kept constant at 0°, the change in pressure from left to right is not that significant. However, some significant deformation due to the lateral shear and bulldozing forces is encountered in the lateral direction of the contact patch.

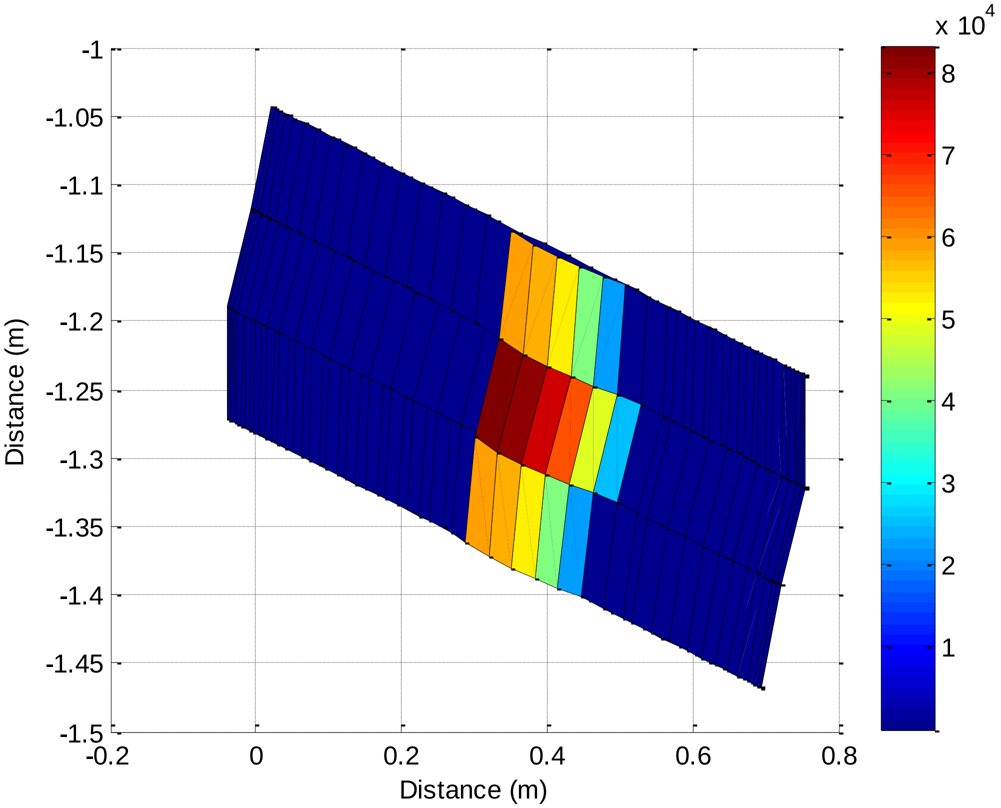

Figure 4-25. Pressure distribution in the contact patch for a slip angle of 15°, a slip ratio of 0% and a normal load of 2,000 N. Note the deformation in the lateral direction of the contact patch

4.5 Combined Slip

Pure lateral and pure longitudinal case studies are really common in tire modeling, however, most of the time vehicles are travelling under a combined slip scenario, therefore, it is really important to account for it.

Figure 4-26 shows the variation in drawbar pull for different slip angles at a normal load of 2,000 N. The figure shows that an increase in slip angle reduces the drawbar pull, which is consistent with the observations made by various researchers. This reduction is attributed to the fact that an increase in slip angle will increase the lateral shear stress, thus, reducing the longitudinal shear stress; since the combined forces cannot exceed the shear strength of the soil. However, it is important to note that at negative slip ratios the drawbar pull is higher than at their respective positive slips. This phenomena is attributed to the fact that braking will create higher sinkage, thus, increasing the longitudinal shear stress.

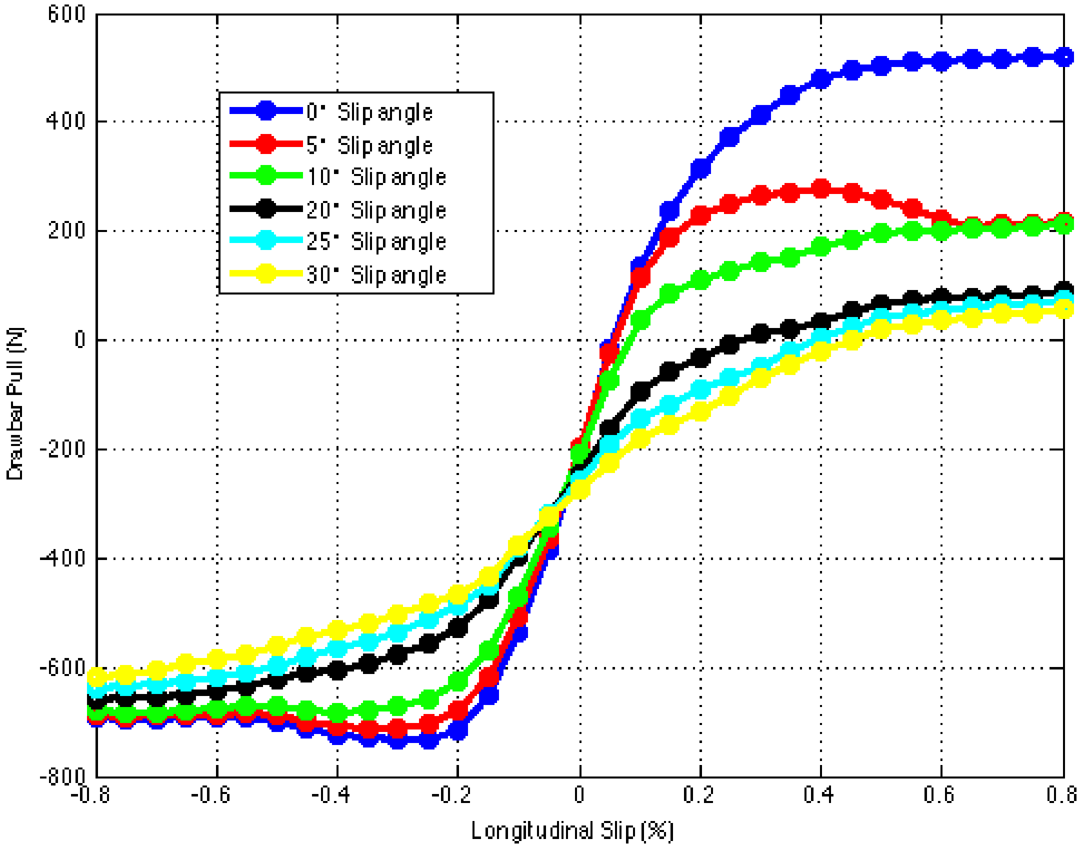

Figure 4-26. Drawbar pull as a function of longitudinal slip for different slip angles at a normal load of 2,000 N

Figure 4-27 shows the lateral force for different slip ratios at a normal load of 2,000 N. As anticipated, the lateral force decreases with an increase in slip ratio. Given the relationship between the longitudinal and the lateral shear stress, an increase in slip ratio will increase the longitudinal shear stress, thus reducing the lateral shear stress and vice versa.

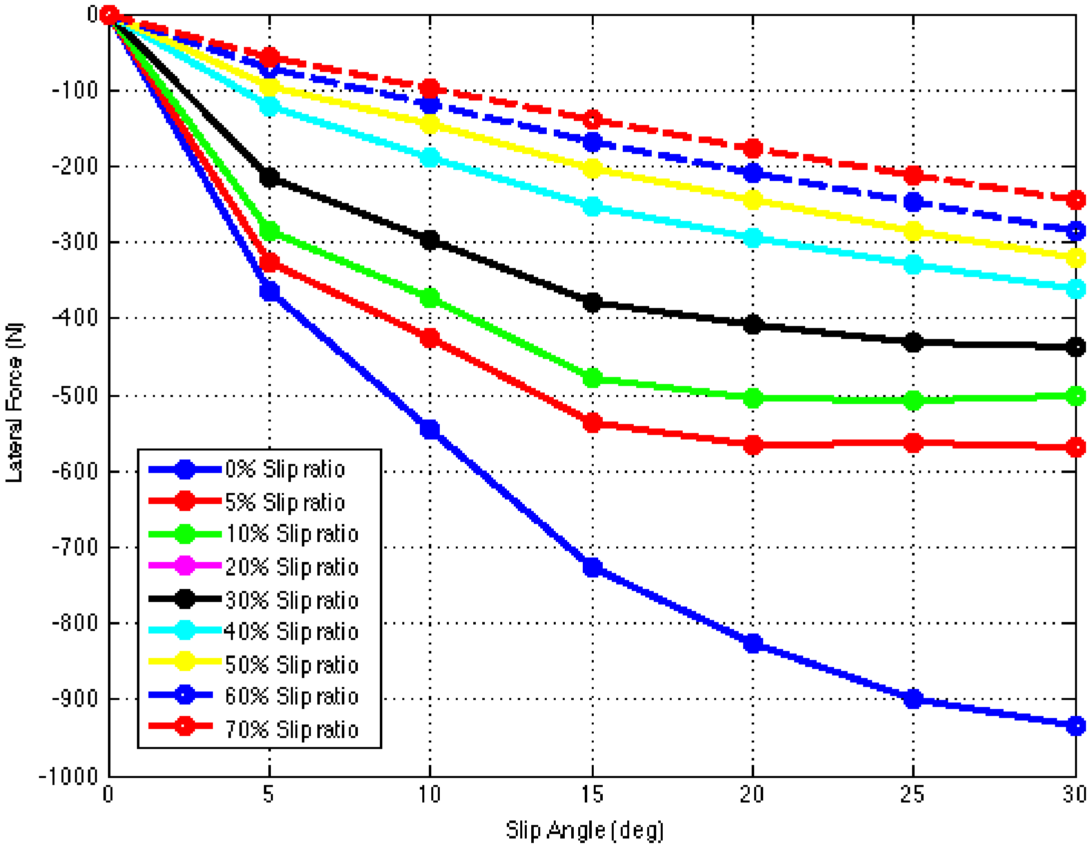

Figure 4-27. Lateral force as a function of slip angle for different longitudinal slips at a normal load of 2,000 N

Figure 4-28 shows the stress distribution at the contact patch for the combined slip scenario. As it can be observed, the longitudinal shear stress increases really quickly from the entry angle. However, at an angle θ_a, the tire starts to slide, which creates a drop in shear stress. Similarly, the lateral shear stress also increases until the angle θ_a, where it also drops. This decrease in shear stress at the angle θ_a guarantees that the Mohr-Coulomb failure criteria is upheld

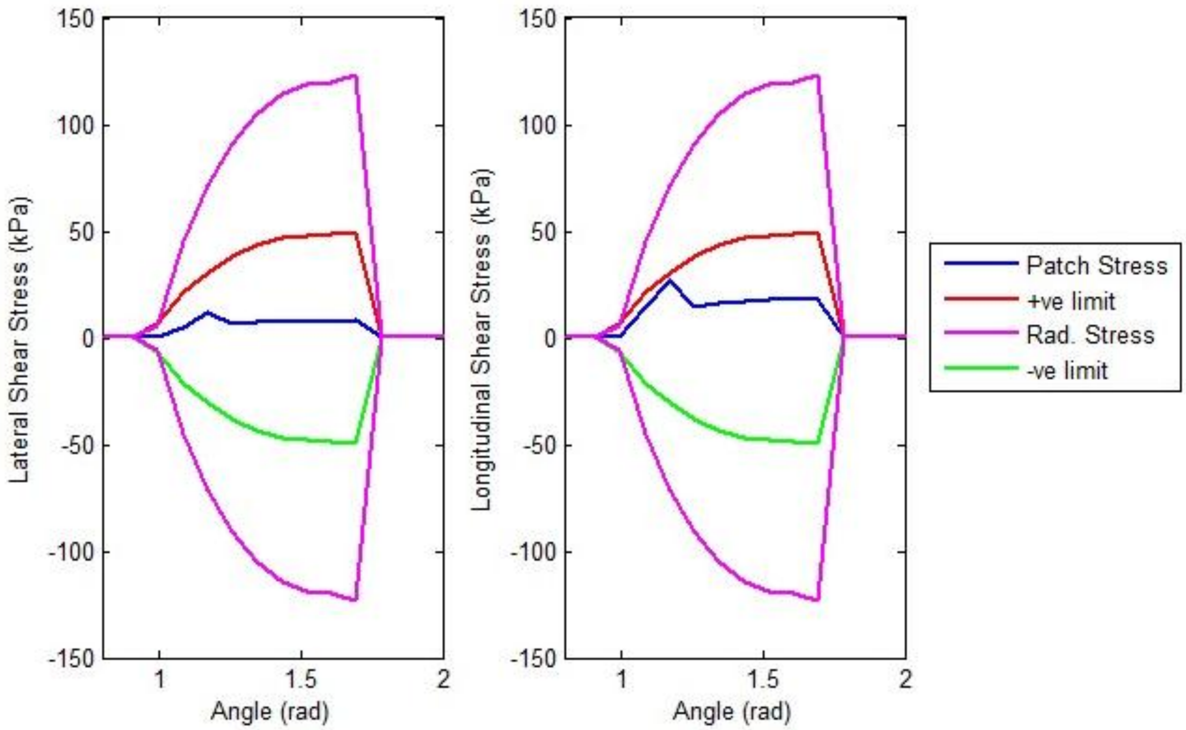

Figure 4-28. Shear stress distribution for the belt and tread layer at a normal load of 4,000N, a slip angle of 10° and 40% slip ratio

4.6 Repetitive Loading

The following section will present the results for repetitive loading. Again, due to the unavailability of experimental data for repetitive loading, the results presented are more qualitative in nature. Figure 4-29 shows the drawbar pull for a normal load of 2,000 N and a longitudinal slip of 20% for three consecutive driven tires. The simulation predicts that drawbar pull increases with each pass, which is due to the fact that less sinkage is experienced, thus, less rolling resistance. This also agrees with the experimental results collected by Holm in [69], which are shown in Figure 3-17 .

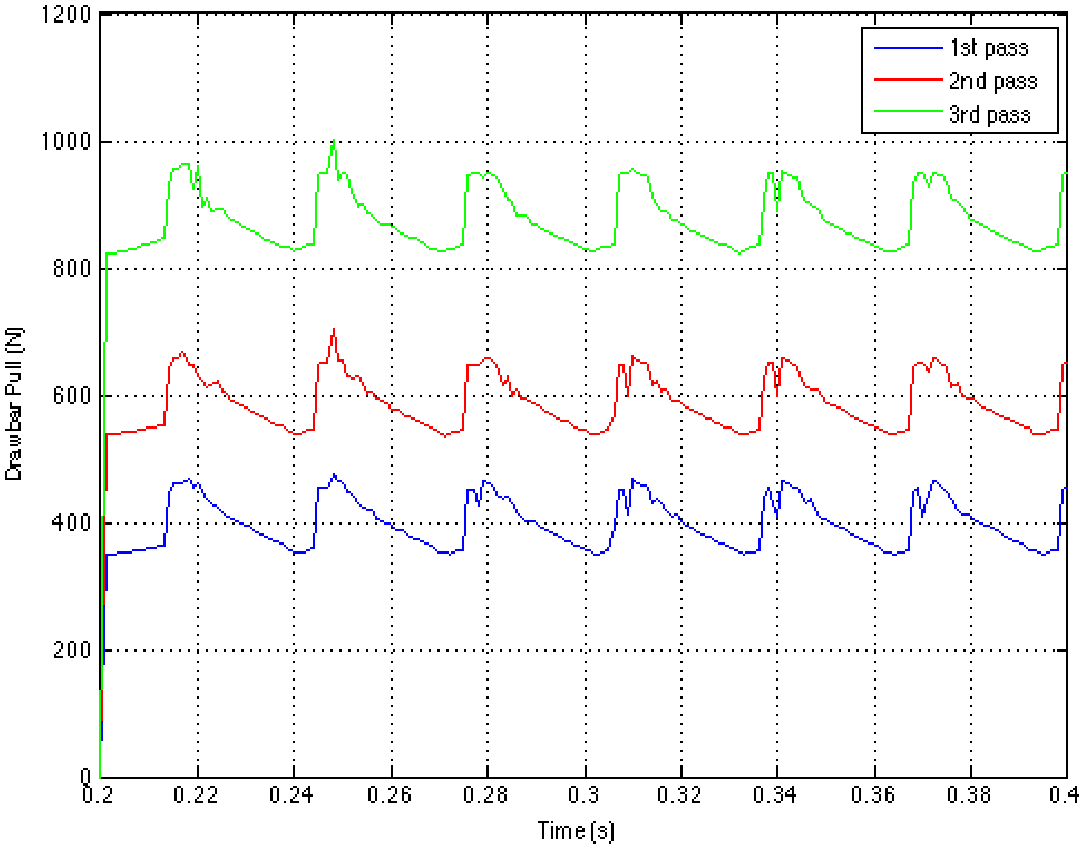

Figure 4-29. Drawbar pull as a function of time for repetitive loading using a normal load of 2,000 N, zero slip angle and a longitudinal slip of 20%

4.7 Chapter Summary

This chapter presented different case scenarios. The dynamic loading over rigid ground was first used to validate the static deflection of the tire. The simulation results should really good agreement with the experimental data, proving that the model can accurately predict tire deformation.

Consequently, a case study for a dynamic loading of the tire under a sandy loam was presented. The simulation results returned data that correlates well with observations made by other researchers. Having shown that the model can predict tire behavior under static conditions, pure lateral and pure longitudinal case studies were shown. Additionally, a combined slip scenario was also presented yielding good results. Finally, a repetitive loading case study was discussed to show how the model can predict multi-pass behavior.

5 Conclusions

This section will present the conclusions found in this investigation. Moreover, it will summarize the work done and will address the main contributions of this work.

5.1 Summarize Work Done

This study developed a three-dimensional tire model for soft soils. The first step was to perform an extensive review of literature of previous work done in the tire modeling and terramechanics fields. After a very thorough analysis it was determined that a discretized semi-empirical tire model would be the best approach; the industry already employs tire models for on-road vehicles based on lumped mass methods, so an extension to off-road applications was considered appropriate. This approach would guarantee that the model could be used for different tires, soils, and simulation scenarios without the need of really expensive or time-consuming tests.

Three layers with N_m number of masses were used to represent the sidewalls and the tread and belt layer of the tire. Thus, a more realistic application of the external ground forces could be done. Moreover, by using a discretized approach, a better resolution is obtained at the contact patch without having to use more computationally expensive modeling approaches. Likewise, the model accounts for different simulation parameters such as camber angle, slip angle, slip ratio, and normal load. Thus, different simulation scenarios can be carried out; including repetitive loading for driven or towed wheels.

The formulation used to predict sinkage, pressure, and shear stress is based on the work of well-established theories brought forth by Grahn, Bekker, Wong and Janosi/Hanamoto. Moreover, the model is based on previous work done at AVDL by Sandu, Chan, and Senatore, which has shown to yield good results. Furthermore, concurrent with this work, Anake Umsrithong in [78] has also been developing a single plane discretized lumped mass approach for rigid rough terrain that has also proven to provide good results.

This study also developed consistent and simple tests that could be used to obtain tire and soil parameters. Parameter identification techniques were also presented in an effort to identify how each parameter is obtained, thus, reducing ambiguity.

Finally, different case scenarios were presented to demonstrate the capabilities of the tire model. The tire deformation was validated for static rigid ground conditions showing really good agreement with the experimental data. Dynamic loading simulations were also done for soft soil conditions. Pure longitudinal and pure lateral case scenarios demonstrated that the model produced consistent data based on the principles of mechanics. Likewise, a combined slip scenario also proved to yield consistent data. Ultimately, a repetitive loading case was used to display the capability of the model. All the case scenarios presented showed good agreement with experimental data collected by other researchers in the field, however, further refinement will probably be needed once experimental data is collected.

5.2 Main Contribution

The main contribution of this research is the development of a discretized tire model dedicated to soft soil conditions. As it was presented in the review of literature, the discretized tire model approach is relatively popular in the on-road tire modeling community; however, no evidence of a discretized approach for soft soil conditions was found. Thus, this model provides a great medium between the simple empirical models and the highly complex finite element models used in the terramechanics field.

One of the advantages of using a lumped mass approach is that the model can be applicable to a large range of driving scenarios. By using a different number of lumped masses the resolution of the model can be adjusted, and thus the frequency range of the simulation. Moreover, by introducing a multiple plane approach a more realistic application of the ground forces can be done, since now they can act directly on the sidewall, or on the tread and belt layer, as needed. Furthermore, by using multiple planes it can be accounted for not only the curved shape of the tire but also for the stiffness in the different directions of the tire.

Another contribution of this research is the methodology used to calculate the ground forces. The equations used to calculate the ground forces in this research have been extensively used by other researchers, however, the methodology used to adapt them to work for a lumped mass approach is a novel method.

The implementation of a rheological soil model to calculate the normal pressure is also a contribution of this study. Previously, the soil models used at AVDL were all for quasi-static conditions, thus, this is a big leap forward to better represent the tire-soil interaction for a rolling tire scenario. Furthermore, the methodology used to implement this model is also novel since it has never been used in a lumped mass approach.

Another contribution of this thesis is that the tire can lose contact with the ground. In the past, all the models developed at AVDL required for the tire to be in contact with the ground at all times. Therefore, the uni-lateral contact formulation used in this model is more efficient.

Finally, the last contribution of this study is the graphical user interface developed. This GUI is presented in the appendix in section 6.1- Graphical User Interface (GUI) and it is used to easily access the different tire models developed at AVDL. The great advantage of this GUI is that a variety of tire models have been developed at AVDL, however, they are not easily accessible by other members of the laboratory. Hence, the idea to create a tire model interface that can easily be used by other members of the laboratory.

5.3 Future Work

This section will present some aspects that need to be addressed in the future to better represent the tire and the tire-soil interaction. Moreover, some other recommendations are done regarding the inclusion of other simulation scenarios.

5.3.1 Soil and Tire Parameter Testing

Having accurate soil and tire parameters guarantees better simulation results. Therefore, if a thorough and accurate validation of the model is to be performed, good tire and soil parameters are required.

5.3.2 Bulldozing Force Formulation

The formulation for the bulldozing force assumes that no soil is compacted and all the soil is displaced to the outside of a steered tire. Nonetheless, this is not entirely accurate since some soil is displaced and other is compacted. As such, a more accurate approach can be formulated utilizing experimental data to quantify the amount of soil displaced and compacted.

5.3.3 Optimization Algorithm for Tire Parameters

The performance of the tire model is highly dependent on the accuracy of the input parameters. As such, having a reliable optimization algorithm for the tire parameters guarantees the accuracy of the tire model. Unfortunately, in order to accomplish this task several tires are required to assure that the optimization yields accurate results, which was something this author didn't have access to.

5.3.4 Include Tread Pattern or Lugs

It is well known that tread pattern has a reasonable influence in vehicle performance in soft soil conditions. This is due to the fact that lugs and treads allow the tire to flush excess water and soil from the tire. Moreover, the lugs also help to increase the friction between the tire and the soil. Thus, it would be very beneficial to add a tread pattern or lug to the simulation. Nonetheless, this is not an easy task since the formulation required to determine contact between the tire and the soil is really complex.

5.3.5 Rough Terrain

Increasing the capability of the model to accommodate for rough terrain or discrete obstacles will make the model more powerful. This would increase the amount of driving situations the model can account for, making it much more versatile and desirable especially, since off-road locomotion is generally not on smooth surfaces.

5.3.6 Non-linear Dynamics

According to Sadeghi and Ahmadian in [79], It is tires have a non-linear behavior. In this model linear dynamics are used to represent the tire; thus, introducing non-linear elements into the model would most likely increase the accuracy of the model. However, obtaining the parameters needed to portray this non-linear behavior is not an easy task.

5.3.7 Standardized Methodology for Model Benchmarking

It would help performing benchmarking studies between different tire models if all researchers would use standardized case studies. Thus, it is recommended to develop a standard simulation and testing methodology for tires in off-road conditions.

References

1. **Rauh, J., and Mössner-Beigel, M.**, (2008) "*Tyre simulation challenges.*" Vehicle System Dynamics, 46(1): p. 49-62.

2. **Wismer, R.D., and Luth, H. J.** , (1973) "*Off-road traction prediction for wheeled vehicles.*" Journal of Terramechanics, 10(2): p. 49-61.

3. **Brixius, W.**, (1987) "*Traction Prediction Equations for Bias-ply Tires.*" Transactions of the American Society od Agricultural Engineers (871622).

4. **Haley, P.W., Jurkat, M. P., and Brady, P.M. Jr.**, (1979) "*NATO Reference Mobility Model, Edition I, Users Guide, Volume I, Operational Modules.*" US Army Tank-Automotive Research & Development Command. Warren, MI.

5. **Haley, P.W., Jurkat, M. P., and Brady, P.M. Jr.**, (1979) "*NATO Reference Mobility Model, Edition I, Users Guide, Volume II, Obstacle Module.*" US Army Tank-Automotive Research & Development Command. Warren, MI.

6. **Ahlvin, R.B., and Haley, P. W.**, (1992) "*NATO Reference Mobility Model, Edition II, NRMM II User's Guide.*" US Army Engineer Waterways Experiment Station. Vicksburg, MI.

7. **Upadhyaya, S.K., Jubbal, G., and Wulfsohn D.**, (1989) "*Traction Prediction Equations for Radial Ply Tyres.*" Journal of Terramechanics, 26(2): p. 149-175.

8. **Upadhyaya, S.K., and Wulfsohn, D.**, (1993) "*Traction Prediction Using Soil Parameters Obtained with an Instrumented Analog Device.*" Journal of Terramechanics, 30(2): p. 85-100.

9. **Uffelmann, F.**, (1961) "*The Performance of Rigid Wheels on Clay Soils*". in *1st Int. Conf. Soil Vehicle Mechanics* Turin, Italy.

10. **Allen, R.W., Rosenthal, T. J., and Chrstos J. P.**, "*A Vehicle Dynamics Tire Model for Both Pavement and Off-Road Conditions (# 970559)*", in *SAE Int. Congress & Exposition*1997: Detroit, Michigan.

11. **Metz, D.**, (1993) "*Dynamics of Four-Wheel-Steer Off-Highway Vehicles (SAE #930765).*" Society of Automotive Engineers: p. 30.

12. **Wong, J.Y.**, "*Theory of Ground Vehicles*". 4th ed ed2008, Hoboken, NJ: John Wiley & Sons.

13. **Priddy, J.**, (1999) "*Improving the Traction Prediction Capabilities in the NATO Reference Mobility Model (NRMM).*" US Army Corps of Engineers. Vicksburg, MS.

14. **Michelin North America**. (2012) [cited 2012 Jan 16]; Available from: http://michelinman.com/tire-selector/category/light-truck/ltx-a-t2/tire-details.

15. **Plackett, C.W.**, (1985) "*A Review of Force Prediction Methods for Off-road Wheels."* The British Society for Research in Agricultural Engineering, 31: p. 1-29.

16. **Micklethwaite, E.W.E.**, (1944) "*Soil Mechanics In Relation to Fighting Vehicles.*" Military College of Science. Chertsey, UK.

17. **Bekker, M.G.**, "*The Theory of Land Locomotion"*1956, Ann Arbor, Michigan: University of Michigan Press.

18. **Bekker, M.G.**, "*Off the Road Locomotion"*1960, Ann Arbor, Michigan: University of Michigan Press.

19. **Reece, A.R.**, (1965) "*Principles of soil-vehicle mechanics"*. in *Institution of Mechanical Engineers, Automobile Division*. Sage publications.

20. **Onafeko, O., and Reece, A.R.**, (1967) "*Soil Stresses and Deformations Beneath Rigid Wheels."* Journal of Terramechanics, 4(1): p. 59-80.

21. **Wong, J.Y., and Reece, A. R.** , (1967) "*Prediction of Rigid Wheel Performance Based on the Analysis of Soil-Wheel Stresses. Part I. Performance of Driven Rigid Wheels."* Journal of Terramechanics, 4(1): p. 81-98.

22. **Wong, J.Y., and Reece, A. R.** , (1967) "*Prediction of Rigid Wheel Performance Based on the Analysis of Soil-Wheel Stresses. Part II. Performance of Towed Rigid Wheels."* Journal of Terramechanics, 4(2): p. 7-25.

23. **Karafiath, L.L.**, (1971) "*Plasticity Theory and the Stress Distribution Beneath Wheels."* Journal of Terramechanics, 8(2): p. 49-60.

24. **Nowatzki, E.A., Karafiath, L. L.**, (1974) "*General Yield Conditions in a Plasticity Analysis of Soil-Wheel Interaction.*" Journal of Terramechanics, 11(1): p. 29-44.

25. **Karafiath, L.L.**, (1986) "*Tire-Soil Interaction Model for Turning (Steered) Tires.*" Journal of Terramechanics, 23(3): p. 153-169.

26. **Schwanghart, H.**, (1968) "*Lateral Forces on Steered Tyres in Loose Soil.*" Journal of Terramechanics, 5(1): p. 9-29.

27. **Grahn, M.**, (1987) "*Investigation of the Influence of Penetration Velocity on the Pressure/Sinkage Relationship*". in *Proceedings of the 9th International ISTVS Conference*. Barcelona, Spain.

28. **Grahn, M.**, (1991) "*Prediction of Sinkage and Rolling Resistance for Off-The-Road Vehicles Considering Penetration Velocity.*" Journal of Terramechanics, 28(4): p. 339-347.

29. **Gee-Clough, D.**, (1976) "*The Bekker Theory of Rolling Resistance Amended to Take Account of Skid and Deep Sinkage.*" Journal of Terramechanics, 13(2): p. 87-105.

30. **Lyasko, M.**, (2010) "*Slip sinkage effect in soil–vehicle mechanics.*" Journal of Terramechanics, 47: p. 21-31.

31. **Fassbender, F.R., Fervers, C. W., and Harnisch, C.**, (1997) "*Approaches to Predict the Vehicle Dynamics on Soft Soil.*" Vehicle System Dynamics, 27(S1): p. 173-188.

32. **Janosi, Z., and Hanamoto, B.**, (1961) "*Analytical determination of draw bar pull as a function of slip for tracked vehicles in deformable soils*". in *1st Int. Conf. of the International Society for Terrain-Vehicles Systems*. Turin, Italy.

33. **Grecenko, A.**, (1969) "*Slip and Drift of the Wheel with Tyre in Soft Ground*". in *3rd Int. Conf. of the International Society of Terrain-Vehicle Systems*. Essen, Germany.

34. **Grecenko, A.**, (1992) "*The Slip and Drift Model of a Wheel With Tyre Compared to Some Other Attempts in this Field.*" Journal of Terramechanics, 29(6): p. 599-604.

35. **Lee, J.H., Liu, Q., and Zhang, T.**, (2005) "*Predictive Semi-Analytical Model for Tire-Snow Interaction."* Society of Automotive Engineers (2005-01-0932).

36. **Lee, J.H., Liu, Q., and Mourelatos, Z.**, "*Simulation of Tire-Snow Interfacial Forces for a Range of Snow Densities with Uncertainty (# 2006-01-0497)",* in *SAE World Congress & Exhibition*2006: Detroit, Michigan.

37. **El-Gawwad, K.A., Crolla, D.A., Soliman, A. M. A., and El-Sayed, F.M.**, (1999) "*Off-Road Tyre Modelling I: The Multi-Spoke Tyre Model Modified to Include the Effect of Straight Lugs."* Journal of Terramechanics, 36(1): p. 3-24.

38. **El-Gawwad, K.A., Crolla, D.A., Soliman, A. M. A., and El-Sayed, F.M.**, (1999) "*Off-Road Tyre Modelling II: Effect of Camber on Tyre Performance."* Journal of Terramechanics, 36(1): p. 25-38.

39. **El-Gawwad, K.A., Crolla, D.A., Soliman, A. M. A., and El-Sayed, F.M.**, (1999) "*Off-Road Tyre Modelling III: Effect of Angled Lugs on Tyre Performance."* Journal of Terramechanics, 36(2): p. 63-75.

40. **El-Gawwad, K.A., Crolla, D.A., Soliman, A. M. A., and El-Sayed, F.M.**, (1999) "*Off-Road Tyre Modelling IV: Extended Treatment of Tyre-Terrain Interaction for the Multi-Spoke Model."* Journal of Terramechanics, 36(2): p. 77-90.

41. **Li, L., Sandu, C., Lee, J. H., and Liu, B.**, (2009) "*Stochastic modeling of tire–snow interaction using a polynomial chaos approach."* Journal of Terramechanics, 46: p. 165-188.

42. **Chan, B.J.**, (2008) "*Development of an Off-Road Capable Tire Model for Vehicle Dynamic Simulations*" Ph. D Dissertation Virginia Polytechnic Institute and State University Blacksburg, VA

43. **Senatore, C.**, (2010) "*Prediction of mobility, handling, and tractive efficiency of wheeled off-road vehicles*" Ph. D Dissertation Virginia Polytechnic Institute and State University Blacksburg, VA

44. **Hettiaratchi, D.R.P., and Reece, A. R.**, (1967) "*Symmetrical Three-Dimensional Soil Failure."* Journal of Terramechanics, 4(3): p. 45-67.

45. **Liang, C.Y., Allen, R. W., Rosenthal, T.J., Chrstos, J.P., and Nunez, P.**, (2004) "*Tire Modeling for Off-Road Vehicle Simulations"*. in *SAE Automotive Dynamics, Stability & Controls Conference*. Detroit, Michigan: Society of Automotive Engineering.

46. **Fassbender, F.R.**, "*Vehicle Oscillation on Soft Soil Simulated with STINA.*" University of the Federal Armed Forces. Hamburg.

47. **Fassbender, F.R.**, "*Soil-Tire Interface for the Rigid Body Simulation Program ADAMS - Simulation of the Dynamic Vehicle-Soil Interaction.*" University of the Federal Armed Forces. Hamburg, Germany.

48. **Harnisch, C., Lach, B., Jakobs, R., Troulis, M., and Nehls, O.**, (2005) "*A new tyre soil interaction model for vehicle simulation on deformable ground."* International Journal of Vehicle Mechanics and Mobility, 43(1): p. 384-394.

49. **Gipser, M.**, "*FTire, a New Fast Tire Model for Ride Comfort Simulations.*" Esslingen University of Applied Sciences. Munich.

50. **Gipser, M.**, "*The FTire Tire Model Family.*" Esslingen University of Applied Sciences. Esslingen.

51. **Gipser, M.**, (2007) "*FTire - the tire simulation model for all applications related to vehicle dynamics."* Vehicle System Dynamics, 45: p. 139-151.

52. **Gipser, M.**, (2005) "*FTire: A physically based application-oriented tyre model for use with detailed MBS and finite-element suspension models."* Vehicle System Dynamics, 43(1): p. 76-91.

53. **Hofman, G.**, "*FTire Soft Soil Extension"*, E. Pinto, Editor 2011: Blacksburg, VA.

54. **Gallrein, A., and Backer, M.** , (2007) "*CDTire: a tire model for comfort and durability applications."* Vehicle System Dynamics, 45(1): p. 69-77.

55. **Oertel, C.**, (1997) "*On Modeling Contact and Friction Calculation of Tyre Response on Uneven Roads."* Vehicle System Dynamics, 27(S1): p. 289-302.

56. **Oertel, C., and Fandre, A.**, (1999) "*Ride Comfort Simulations and Steps Towards Life Time Calculations: RMOD-K and ADAMS*". in *International ADAMS User's Conference*. Berlin, Germany.

57. **Fervers, C.W.**, (2004) "*Improved FEM simulation model for tire–soil interaction.*" Journal of Terramechanics, 41(2): p. 87-100.

58. **Nakashima, H., and Oida, A.**, (2004) "*Algorithm and implementation of soil–tire contact analysis code based on dynamic FE–DE method.*" Journal of Terramechanics, 41(2): p. 127-137.

59. **Aubel, T.**, (1994) "*FEM Simulation of the Interaction Between Elastic Tire and the Soft Soil-FEM Simulation by VENUS and Validation*". in *6th Int. Conf. of the ISTVS*. Vienna, Austria.

60. **Lee, J.H., and Qing, L.**, "*Interfacial Forces Between Tire and Snow Under Different Snow Depths (# 2006-01-0496)*", in *SAE World Congress & Exhibition*2006: Detroit, Michigan.

61. **Shoop, S.A.**, (2001) "*Finite Element Modeling of Tire–Terrain Interaction.*" US Army Corps of Engineers. Hanover, NH.

62. **Wood, D.M.**, "*Soil Behaviour and Critical State Soil Mechanics*"1990, Cambridge, England: Cambridge University Press.

63. **Darnell, I., Hulbert, G. M., and Mousseau, C. W.**, (1997) "*An Efficient Three-Dimensional Tire Model for Vheicle Dynamic Simulations.*" Mechanics of Structures and Machines, 25(1).

64. **Gent, A.N., and Walter, J. D.**, (2005) "*The Pneumatic Tire.*" Washington, D.C.

65. **MSC Software**. (2011).

66. **Hettiaratchi, D.R.P., and Reece, A. R.**, (1974) "*The Calculation of Passive Soil Resistance.*" Geotechnique, 24(3): p. 289-310.

67. **Terzaghi, K.**, "*Theoretical Soil Mechanics*". 1st Edition ed1943: Wiley & Sons.

68. **Wong, J.Y.**, "*Terramechanics and Off-Road Vehicle Engineering: Terrain Behaviour, Off-Road Vehicle Performance and Design"*. 2nd Edition ed2010, Amsterdam, The Netherlands: Elsevier.

69. **Holm, I.C.**, (1969) "*Multi-Pass Behaviour of Pneumatic Tires."* Journal of Terramechanics, 6(3): p. 47-71.

70. **US Army Engineer Waterways Experiment Station**, (1960) "*The Unified Soil Classification System (Technical Memorandum No. 3-357).*" Corps of Engineers. Vicksburg, MS.

71. **Wong, J.Y., and Preston-Thomas, J.**, (1983) "*On the Characterization of the Shear Stress-Displacement Relationship of Terrain."* Journal of Terramechanics, 19(4): p. 225-234.

72. **Geotech Data**. (2012) [cited 2012 Jan 16]; Available from: http://www.geotechdata.info/geotest/california-bearing-ratio-test.

73. **Kawase, Y., Nakashima, H., and Oida, A.**, (2006) "*An indoor traction measurement system for agricultural tires."* Journal of Terramechanics, 43(3): p. 317-327.

74. **Yahya, A., Zohadie, M., Ahmad, D., Elwaleed, A. K., and Kheiralla, A. F.**, (2007) "*UPM indoor tyre traction testing facility."* Journal of Terramechanics, 44(4): p. 293-301.

75. **Sandu, C., Taylor, B., Biggans, J. and Ahmadian, M.**, (2008) "*Building Infrastructure for Indoor Terramechanics Studies: The Development of a Terramechanics Rig at Virginia Tech"*. in *16th ISTVS International Conference*. Turin, Italy.

76. **Taylor, B.P.**, (2009) "*Experimental Evaluation and Semi-Empirical Modeling of the Tractive Performance of Rigid and Flexible Wheels on Lunar Soil Simulant*" Virginia Polytechnic Institute and State University Blacksburg

77. **Organic Rose Care**. (2012) [cited 2012 Jan 16]; Available from: http://www.organicrosecare.org/articles/soils_primer.php?continued=yes.

78. **Umsrithong, A.**, (2012) "*Semi-Empirical Stochastic Transient Tire Models*" P.h. D. Dissertation Virginia Polytechnic Institute and State University Blacksburg, VA

79. **Sadeghi, S., and Ahmadian, M.T.**, (2001) "*Tire Modeling with Nonlinear Behavior for Vehicle Dynamics Studies."* Scientia Iranica, 8(2): p. 145-148.

6 Appendix

This first appendix presents the graphical user interface developed to use this tire model and all other tire models developed at AVDL. The second appendix shows the experimental data provided by Schnabel Engineering on the silky sand.

6.1 Graphical User Interface (GUI)

One of the objectives of this project was to improve the ease of using tire models developed at AVDL. Thus, a graphical user interface (GUI) was a tool that needed to be developed. Due to the fact that MATLAB was used to program the tire model in this study, as well as in the past in our laboratory, it was only logical to use the same tool for the graphical interface. Five GUIs were developed in this study, and they can be selected depending on the needs and preferences of the user.

The welcome GUI is very simple in appearance and is used to determine the tire model that is to be used. Four options are available to the user:

1. Three-Dimensional (3 layer) Discretized Soft Soil Tire Model, which is the tire model developed in this study.
2. Three-Dimensional Flexible Ring Soft Soil Tire Model, which is a flexible ring tire model developed at AVDL by Chan [42].
3. Three-Dimensional Rigid Wheel Soft Soil Tire Model, which is a rigid wheel tire model developed at AVDL by Chan [42].
4. Two-Dimensional (1 layer) Discretized Rough Terrain Tire Model, which is a discretized lumped mass model developed for rough terrain by Anake Umsrithong [78].
5. Three-Dimensional Flexible Belt Rigid Terrain Tire Model, which is a flexible belt tire model for on-road applications developed at AVDL. The steady-state formulation was developed by Chan [42] and the transient formulation by Umsrithong [78]. It is also important to note that both deterministic and stochastic models are included in this tire models.

A screenshot of this GUI can be observed in Figure 6-1.

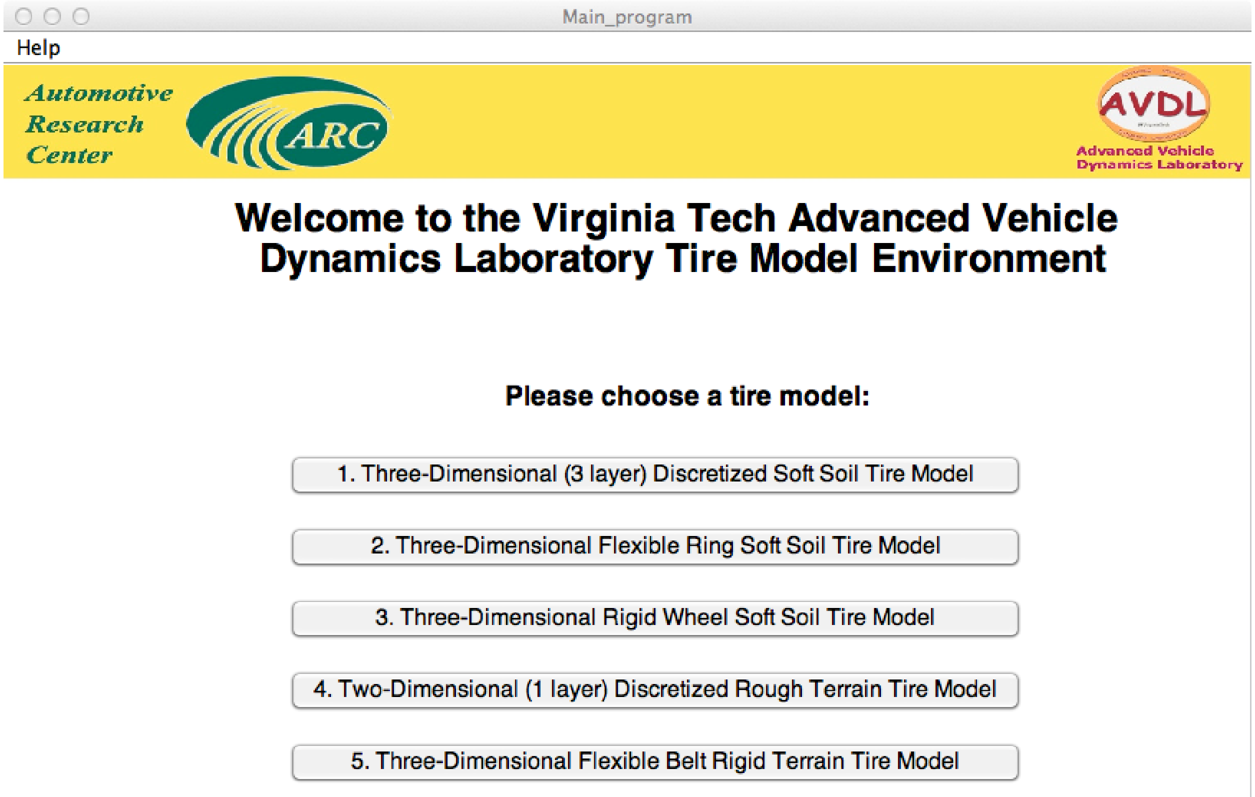

Welcome to the Virginia Tech Advanced Vehicle Dynamics Laboratory Tire Model Environment

Please choose a tire model:

Figure 6-1. Welcome screen of the AVDL Tire Model Environment

If the model described in this study is chosen, then the GUI in Figure 6-2 is displayed. This GUI is used to ask the user the type of interface that is to be used. As the name explains it, the "Predefined Soil and Tire Parameters" interface uses predefined tire and soil parameters in the simulation. On the other hand, the "User-defined Soil and Tire Parameters" interface gives the user the flexibility of using their own parameters to run the model.

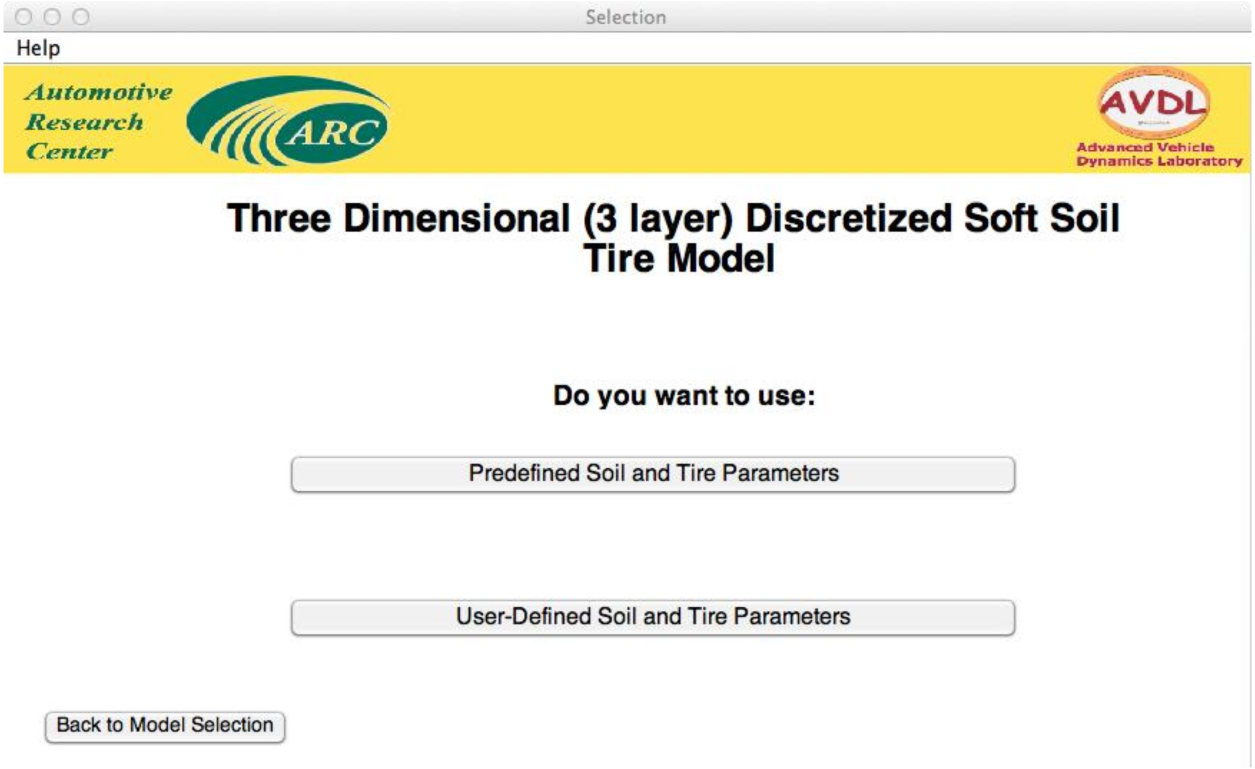

Three Dimensional (3 layer) Discretized Soft Soil Tire Model

Do you want to use:

Figure 6-2. Three-dimensional (3 layer) discretized soft soil tire model parameter type selection GUI

The "Predefined Soil and Tire Parameters" interface shown in Figure 6-3 is geared to those users that (i) are working with a limited number of tires and terrains and don't want to input the data every time, or (ii) don't have all the parameters needed to run the model and use the parameters already available.

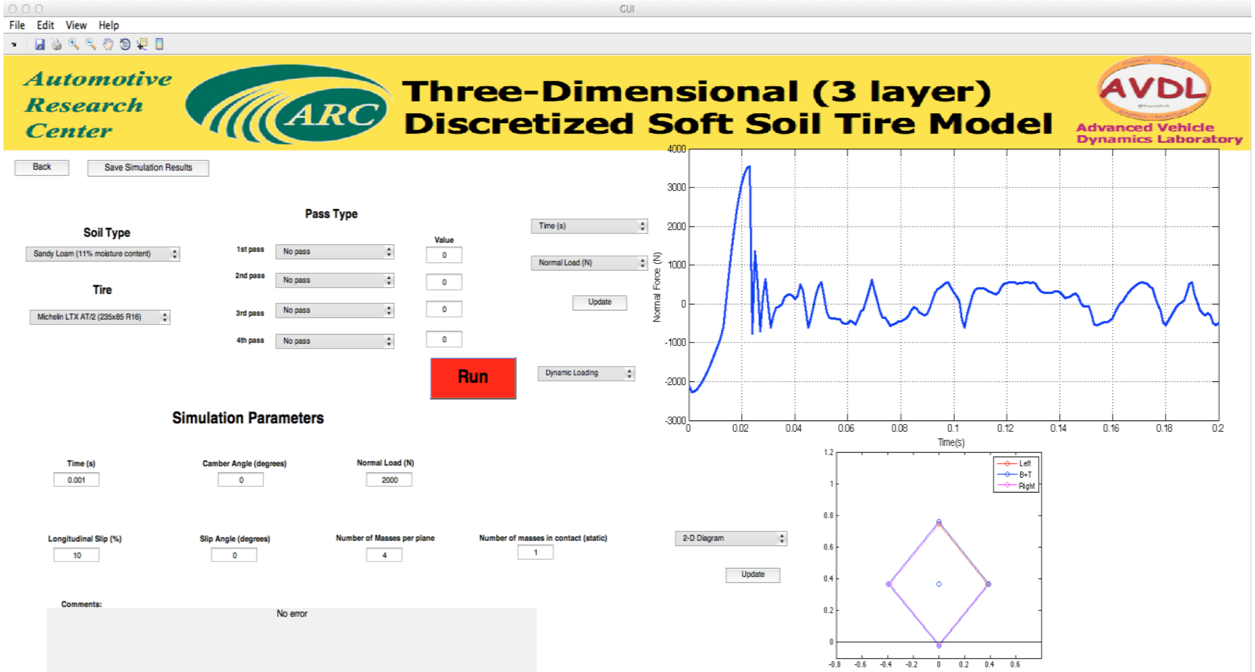

Soil Type: Sandy Loam (11% moisture content)

Tire: Michelin LTX AT/2 (235x85 R16)

Pass Type		Value
1st pass	No pass	0
2nd pass	No pass	0
3rd pass	No pass	0
4th pass	No pass	0

Time (s)

Normal Load (N)

Dynamic Loading

Simulation Parameters

Time (s): 0.001

Camber Angle (degrees): 0

Normal Load (N): 2000

Longitudinal Slip (%): 10

Slip Angle (degrees): 0

Number of Masses per plane: 4

Number of masses in contact (static): 1

2-D Diagram

Comments: No error

Figure 6-3. “Predefined Soil and Tire Parameters” user interface

Observing the screenshot in Figure 6-3 it is evident that using this GUI is really simple. A tire, soil type, type of pass and number of passes needs to be selected from drop down lists. Once this is done the simulation parameters need to be inputted and the simulation is ready to begin. As soon as the simulation is finished running, the user is able to plot a variety of values in the adjacent axis for either the dynamic settling or the different passes performed. Moreover, the user is also able to observe a variety of diagrams or videos in the secondary axes. Finally, the last feature of this GUI is the ability to save all the values in the workspace.

The “User-defined Soil and Tire Parameters” interface was developed for users that want more control of their input parameters. In this interface as it can be observed in Figure 6-4 all the input parameters for the wheel, tire, and terrain can be user-defined. This gives the user the flexibility of using the tire model with any tire or soil type. The same simulation parameters from the other interface can also be found here.

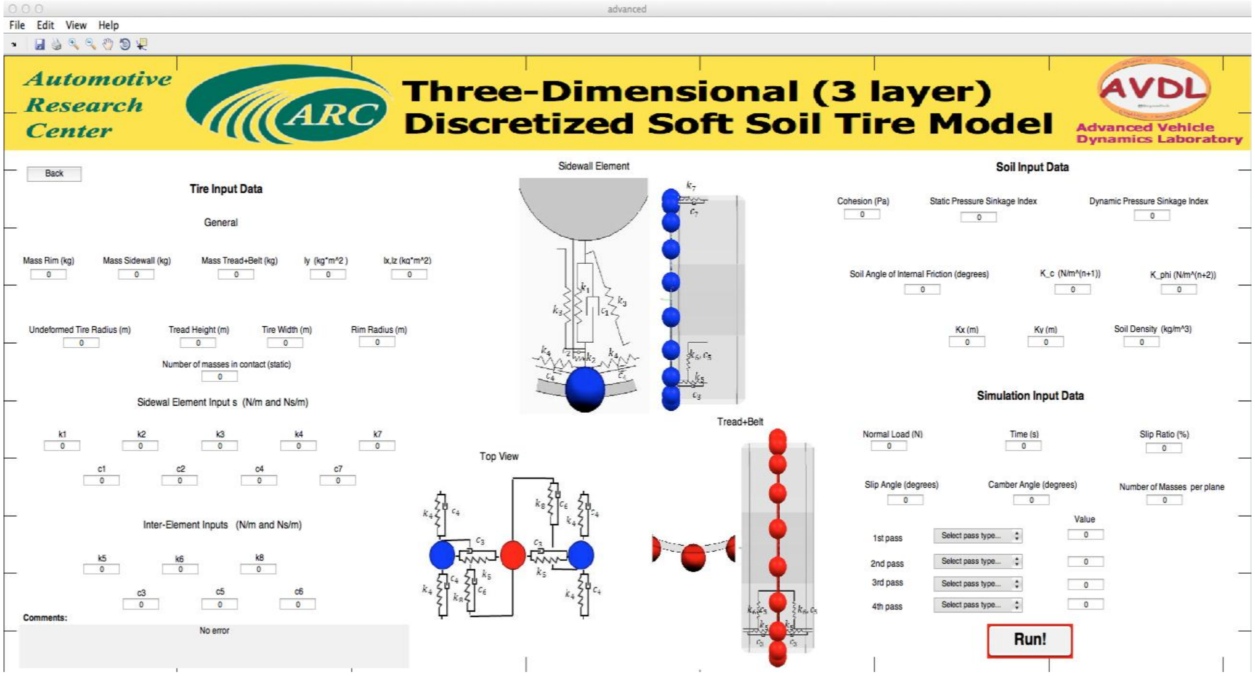

Tire Input Data

General

Mass Rim (kg): 0
Mass Sidewall (kg): 0
Mass Tread+Belt (kg): 0
Iy (kg*m^2): 0
Ix,Iz (kg*m^2): 0
Undeformed Tire Radius (m): 0
Tread Height (m): 0
Tire Width (m): 0
Rim Radius (m): 0
Number of masses in contact (static): 0

Sidewal Element Input s (N/m and Ns/m)

k1: 0
k2: 0
k3: 0
k4: 0
k7: 0
c1: 0
c2: 0
c4: 0
c7: 0

Inter-Element Inputs (N/m and Ns/m)

k5: 0
k6: 0
k8: 0
c3: 0
c5: 0
c6: 0

Comments:
No error

Soil Input Data

Cohesion (Pa): 0
Static Pressure Sinkage Index: 0
Dynamic Pressure Sinkage Index: 0
Soil Angle of Internal Friction (degrees): 0
K_c (N/m^(n+1)): 0
K_phi (N/m^(n+2)): 0
Kx (m): 0
Kv (m): 0
Soil Density (kg/m^3): 0

Simulation Input Data

Normal Load (N): 0
Time (s): 0
Slip Ratio (%): 0
Slip Angle (degrees): 0
Camber Angle (degrees): 0
Number of Masses per plane: 0

		Value
1st pass	Select pass type...	0
2nd pass	Select pass type...	0
3rd pass	Select pass type...	0
4th pass	Select pass type...	0

Figure 6-4. “User-defined Soil and Tire Parameters” user interface

Finally, the last GUI developed was the results GUI. Due to the fact that there was no available space in the “User-defined Soil and Tire Parameters” GUI to show any results, a GUI was developed to present the simulation results. As it can be observed in Figure 6-5, the layout is really simple and it has the same plotting capabilities of the “Predefined Soil and Tire Parameters” interface.

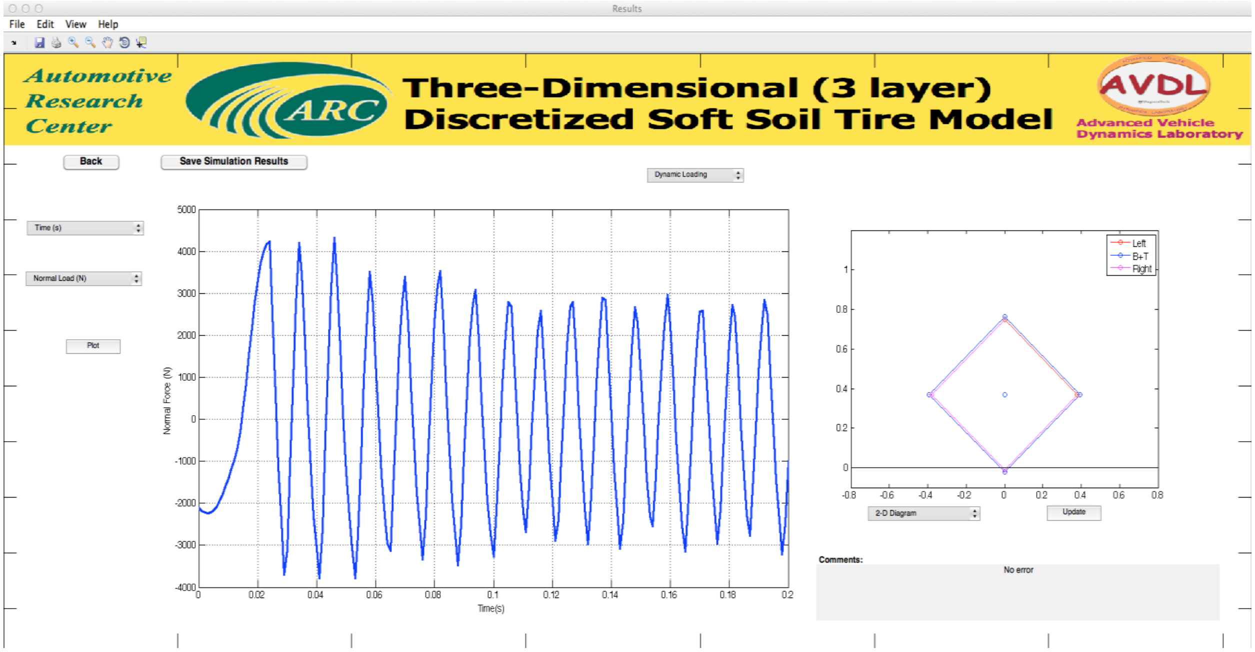

Dynamic Loading

Time (s)

Normal Load (N)

2-D Diagram

Comments:

No error

Figure 6-5. Results graphical interface

6.2 Soil Data provided by Schnabel Engineering

Soil Data provided by Schnabel Engineering for the silky sand.

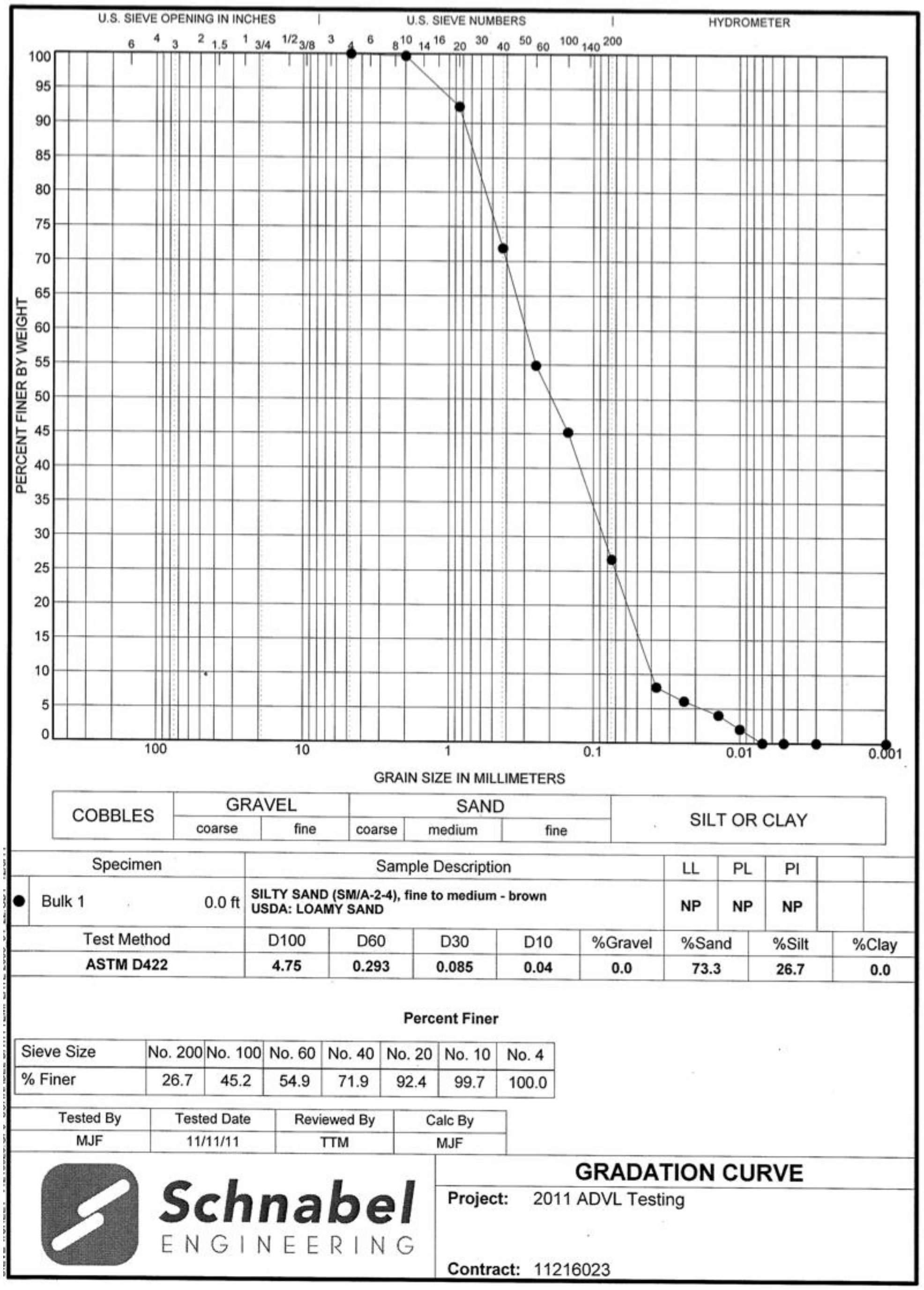

COBBLES	GRAVEL		SAND			SILT OR CLAY
	coarse	fine	coarse	medium	fine	

	Specimen		Sample Description	LL	PL	PI		
●	Bulk 1	0.0 ft	**SILTY SAND (SM/A-2-4), fine to medium - brown** **USDA: LOAMY SAND**	**NP**	**NP**	**NP**		

Test Method	D100	D60	D30	D10	%Gravel	%Sand	%Silt	%Clay
ASTM D422	**4.75**	**0.293**	**0.085**	**0.04**	**0.0**	**73.3**	**26.7**	**0.0**

Percent Finer

Sieve Size	No. 200	No. 100	No. 60	No. 40	No. 20	No. 10	No. 4
% Finer	26.7	45.2	54.9	71.9	92.4	99.7	100.0

Tested By	Tested Date	Reviewed By	Calc By
MJF	11/11/11	TTM	MJF

Schnabel
ENGINEERING

GRADATION CURVE

Project: 2011 ADVL Testing

Contract: 11216023

Figure 6-6. Gradation curve for silty sand used. Provided by Schnabel Engineering.

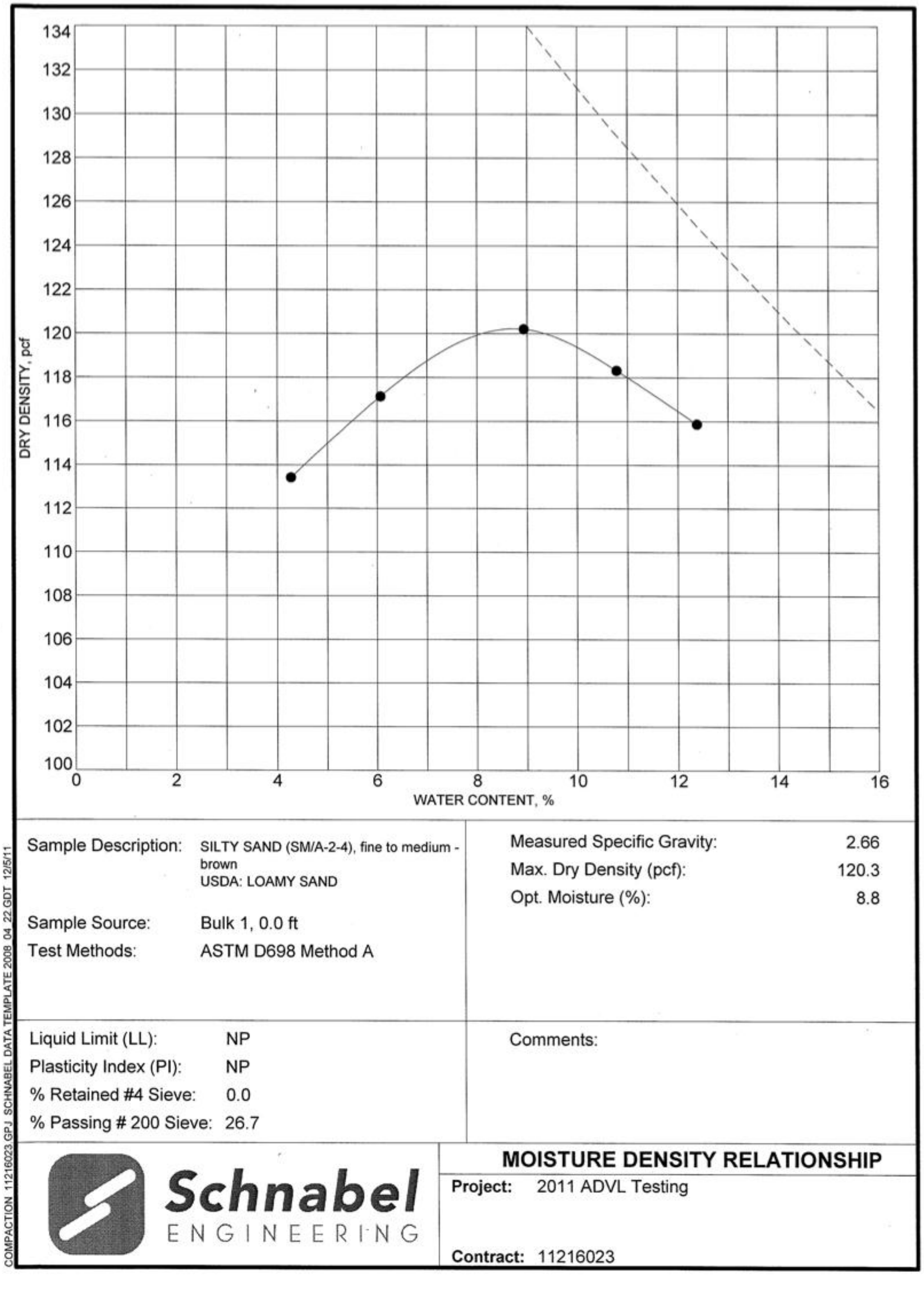

Sample Description: SILTY SAND (SM/A-2-4), fine to medium - brown
USDA: LOAMY SAND

Sample Source: Bulk 1, 0.0 ft
Test Methods: ASTM D698 Method A

Measured Specific Gravity: 2.66
Max. Dry Density (pcf): 120.3
Opt. Moisture (%): 8.8

Liquid Limit (LL): NP
Plasticity Index (PI): NP
% Retained #4 Sieve: 0.0
% Passing # 200 Sieve: 26.7

Comments:

Schnabel ENGINEERING

MOISTURE DENSITY RELATIONSHIP

Project: 2011 ADVL Testing

Contract: 11216023

COMPACTION 11216023.GPJ SCHNABEL DATA TEMPLATE 2008_04_22.GDT 12/5/11

Figure 6-7. Moisture density relationship for silty sand used. Provided by Schnabel Engineering